NUCLEAR MAGNETIC RESONANCE

Introduction

An important objective in materials science is the establishment of relationships between the microscopic structure or molecular dynamics and the resulting macroscopic properties. Once established, this knowledge then allows the design of improved materials. Thus, the availability of powerful analytical tools such as NMR spectroscopy (1–13) is one of the key issues in polymer science. Its unique chemical selectivity and high flexibility allows one to study structure, chain conformation and molecular dynamics in much detail and depth. NMR in its different variants provides information from the molecular to the macroscopic length scale and on molecular motions from 1 to 10^{10} Hz. It can be applied to crystalline as well as to amorphous samples which is of particular importance for the study of polymers.

Moreover, NMR can be conveniently applied to polymers since they contain predominantly nuclei that are NMR sensitive such as ^{1}H and ^{13}C.

Although well established for liquid-like samples such as macromolecules in solutions (14,15), the applications of NMR to solid or solid-like polymers is more demanding because of the presence of anisotropic interactions that complicate the analysis of the results. Several techniques for the removal of these interactions have thus been developed and are nowadays in a state where they could be routinely applied. Nonaveraged anisotropic interactions on the other hand provide valuable information that is lost in the solution state. Thus, while it is often necessary to remove the anisotropic interactions, in many cases one would simultaneously like to preserve them in order to exploit their information content.

This is where two-dimensional (2D) spectroscopy comes into play (1), for instance, by correlating one-dimension where the anisotropic interactions are preserved with a (high resolution) dimension where they are removed. Multidimensional NMR spectroscopy proves to be a powerful method to reveal structural and dynamical information at the molecular level in elastomers (16). Residual dipolar couplings can be measured site-selectively and correlated with the cross-link density and mechanical stress. The local segmental order and information on local molecular motions can also be obtained with newly developed 2D NMR methods (16). The information at the molecular level can be correlated with macroscopic properties of elastomers and provides the basis for a better design of material properties for specific applications.

From the viewpoint of NMR, elastomers, and other viscoelastic polymers above their glass-transition temperature exhibit both, solid-like and liquid-like features (12). Whereas the segmental motions give rise to the liquid-like behavior, the presence of permanent or nonpermanent cross-links leads to residual dipolar couplings, that is responsible for the solid-like properties. This promises that both properties can be exploited, but the application of 2D techniques to viscoelastic materials has to deal with the difficulties related to both, rigid and mobile samples (16). Compared with the wealth of applications in solution and in the solid state, NMR has not been widely applied to viscoelastic polymers, although it can provide information on such important areas as the chain dynamics in elastomers, the local structure, residual couplings (induced by chemical cross-links and topological constraints), dynamic order parameters, internuclear distances, intermolecular interactions (which are important for instance for the miscibility), the effects of fillers on molecular motions, and segmental orientation under mechanical stress and others.

NMR imaging finds most of its applications in medical diagnostics of humans and pathology studies of animal models (17–22). The success of the method is based on noninvasiveness of the nuclear magnetic resonance and the unsurpassed soft-matter contrast, which is hard to achieve with competitive methods like X-ray or computer tomography. The same advantages can be exploited in imaging studies related to materials science (19,22). Here, an important class of soft-matter materials is given by synthetic polymers above the glass transition temperature. Apart from Semicrystalline Polymers (qv) like polyethylene, polypropylene, some polyamides, and polymer melts, elastomers constitute the most striking class of synthetic soft matter with a modulus similar to many biological tissues. Applications of imaging for which nondestructiveness or contrast are essential, are

competitive with other imaging techniques in the information gained and the cost of the experiment. Such applications to elastomers concern distributions in temperature, stress, cross-link density, modulus, and the dynamics of fluid absorption and swelling.

The nucleus imaged most often is the proton. The reason is not only sensitivity but also the weak dipolar couplings between protons in a chemical group and between different chemical groups which dominate the signal decay by relaxation. These dipolar couplings are motionally averaged by the often fast but nearly always anisotropic motion of intercross-link chains. This motion and consequently the value of the residual dipolar couplings are affected by chain stiffness, cross-link density, chain orientation, temperature, and additives, etc. Given that the residual dipolar interactions are too strong to obtain chemical-shift resolution without sample spinning or multipulse techniques, relaxation techniques that probe different time regimes of molecular motion provide the primary access to contrast in imaging of elastomers.

After a brief introduction of the basic principles of NMR, the one-dimensional (1D) and two-dimensional (2D) methods that have been applied to viscoelastic materials will be reviewed. NMR imaging which can be considered as a special form of multidimensional NMR will be introduced by discussing principles and image contrast. Illustrative examples of NMR imaging to elastomer materials are given.

Basic Principles of NMR

Magnetic Resonance Phenomenon. Magnetic resonance is a branch of spectroscopy that detects the quantum-mechanical transitions induced by electromagnetic radiation in a system of discrete energy levels of electron or nuclei placed in a static magnetic field. Nuclear magnetic resonance (NMR) employs electromagnetic waves in the radio-frequency range between 900 MHz and 2 kHz.

Nuclear magnetic resonance is one of the most powerful method for structural and dynamics investigation on matter in different states of aggregation. This is due to the following features: (*1*) The interaction of nuclear magnetic moments are very weak compared with the thermal energy, therefore, we deal with nuclear paramagnetism. Moreover, the energy delivered by the radio-frequency generator are much larger compared with the strength of these internuclear couplings. That leads to the possibility to manipulate these interactions in a specific way and to simplify the spectral response. (*2*) The radio-frequency photons have much lower energy compared with the energy of chemical bonds. Therefore, the interaction of electromagnetic radiation with the matter, especially, biomolecules is nonionising. (*3*) The number of radio-frequency photons with a specific frequency is very large. Hence, the phase of the associated electromagnetic wave is very well defined. The high degree of coherence of radio-frequency radiation is essential for implementation of NMR experiments including magnetic resonance imaging (MRI).

The appearance of NMR spectra, and consequently the molecular structure they are able to provide, arises from the discrete nature of the energy levels pertaining to a nuclear spin system. The energy levels are mainly a result of the

Zeeman interaction $-\vec{\mu}\cdot\vec{B}_0$ between the static magnetic field of induction $\vec{B}_0$ and nuclear magnetic moment $\vec{\mu}$. The quantum-mechanical quantity called spin momentum $\vec{I}$ is related to magnetic moment by $\vec{\mu}=\gamma\hbar\vec{I}$, where γ is the magnetogyric ratio and $\hbar$ is the Planck constant divided by 2π.

In the absence of the magnetic field the nuclear spin states are degenerated (see Fig. 1**a**). The application of a static magnetic field $\vec{B}_0$ induces a magnetic interaction described by the Zeeman Hamiltonian $H=-\vec{\mu}\cdot\vec{B}_0$. Taking the magnetic field orientation to be along the z-direction we get

$$H=-\gamma\hbar B_0 I_z \tag{1}$$

The eigenvalues E_m of this Hamiltonian can be evaluated from the Schrödinger equation

$$H|m\rangle=-\gamma\hbar B_0 m|m\rangle \tag{2}$$

where $|m\rangle$ is the eigenstate corresponding to the eigenvalue $E_m=-\gamma\hbar B_0 m$. The magnetic quantum number is m where $m=I, I-1,\ldots, -I$. Therefore, the equidistant energy differences are for the single-quantum transitions $\Delta m=\pm 1$ given by

$$\Delta E=\hbar\omega_0 \tag{3}$$

where the Larmor frequency is $\nu_0=\nu_{\mathrm{L}}=\omega_0/2\pi$. Energy level diagrams of a spin $I=1/2$ and $I=1$ are shown in Figure 1.

Another important ingredient for a magnetic resonance experiment is represented by the presence of the radio-frequency (rf) field. Only the magnetic component of the electromagnetic field, ie, $\vec{B}_1(t)=\vec{B}_{10}\cos(2\pi\nu t)$ interacts with the magnetic moment of the nuclei. The amplitude of the rf field is $\vec{B}_{10}$ and ν is the carrier frequency. This field is produced by a rf coil and leads to a perturbation Hamiltonian

$$H_{\mathrm{p}}=-\gamma\hbar\vec{B}_{10}\cdot\vec{I}\cos(2\pi\nu t) \tag{4}$$

From time-dependent perturbation theory of quantum-mechanics, it can be stated that a transition between two states $|\psi\rangle$ and $|\phi\rangle$ is allowed provided that $\langle\psi|H_{\mathrm{p}}|\phi\rangle\neq 0$. This takes place if $\nu\approx\nu_0$ (ie, the resonance condition) and the alternative magnetic field $\vec{B}_1(t)$ is polarized perpendicularly to the static magnetic field $\vec{B}_0$. Concerning a spin $I=1$ (Fig. 1**b**), similar calculations show that only the single-quantum transitions $|0\rangle\rightarrow|1\rangle$ and $|-1\rangle\rightarrow|0\rangle$ (and those in the opposite directions) are allowed in the first approximation and occur at the same frequency, given by equation 3.

Quantitative spin system evolution in the presence of the interspin couplings has to be described in the language of quantum-mechanics. This is a reflection of the quantum-mechanical nature of the spins and the fact that the spin couplings via propagator operators encode NMR observables. Nevertheless, the description of nuclear magnetization relaxation processes is done by a semiclassical approach

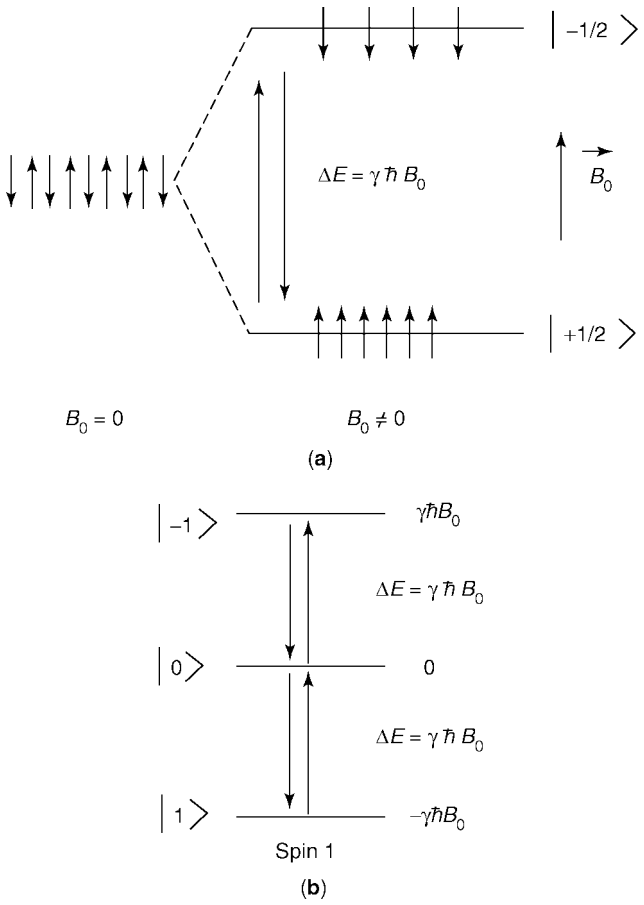

Fig. 1. (**a**) Energy levels diagram and allowed transitions of an ensemble of spins with $I = 1/2$ in the absence and the presence of $\vec{B}_0$. The small arrows indicate the orientation of nuclear spins relative to $\vec{B}_0$. (**b**) Energy diagram and allowed single-quantum transitions for spins with $I = 1$.

where the thermal bath is described classically and the spin system by a quantum-mechanical formalism.

In general, the NMR experiments are performed at high temperatures employing a large number of spins. These features lead to the possibility to treat classically some aspects of the experiments. The excess of spins oriented along the static magnetic field $\vec{B}_0$ with respect of those oriented in the opposite direction (cf Fig. 1**a**) results in a macroscopic nuclear magnetization $\vec{M}$ aligned along the static magnetic field, which is called equilibrium magnetization (cf Fig. 2**a**). It can be displaced from this equilibrium by an appropriate perturbation, for instance, by a rf excitation. It is then subject to a precessional motion around $\vec{B}_0$ with the Larmor frequency ν_L (Fig. 2**b**). The electromagnetic perturbation which brings $\vec{M}$ into a plane perpendicular to $\vec{B}_0$ allows the observation of the Larmor precession through an electromotive force which occurs in a coil whose axis is

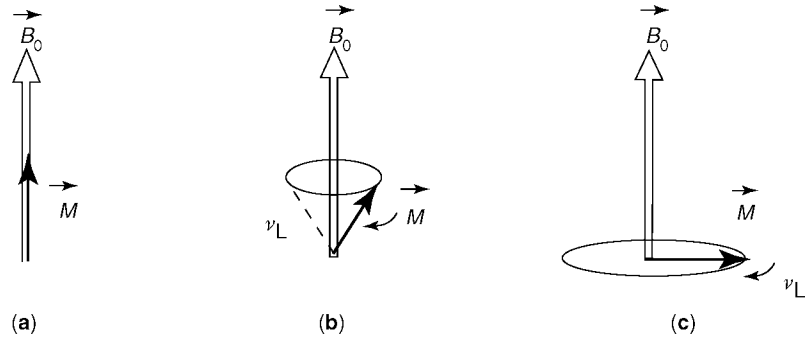

Fig. 2. (**a**) At thermal equilibrium, the nuclear magnetization $\vec{M}$ is collinear with $\vec{B}_0$. (**b**) Under the action of an electromagnetic perturbation $\vec{M}$ is displaced from equilibrium position. It starts undergoes precessional motion around $\vec{B}_0$ at the Larmor frequency $\nu_L = \nu_0$. (**c**) After the action of a 90° rf pulse the magnetization $\vec{M}$ is brought in a transverse plane to $\vec{B}_0$.

contained in that plane (Fig. 2**c**). This can be done by rotation of the nuclear magnetization using a resonant 90° rf pulse. The nuclear magnetization M can be oriented antiparallel to $\vec{B}_0$ by the action of 180° pulse. The majority of NMR experiments used pulse sequences composed of 90° and 180° rf pulses.

Magnetic and Electric Spin Interactions. The nuclear spins can experience various external and internal interactions. These interactions can have magnetic or electric origin. The external interactions are, in general, represented by the Zeeman interactions with static and rf magnetic fields and the gradients of these fields.

The chemical shielding, dipole–dipole, spin–spin indirect coupling or J-coupling, spin-rotation, and hyperfine couplings represent the major internal magnetic interactions. The quadrupolar interaction has an electrostatic character. All these interactions have a tensorial character, ie, are function on the orientation of the principal axes of the tensor relative to the direction of $\vec{B}_0$. They are relevant for solid polymers below and around the glass transition temperatures. For polymer in solution or for soft polymers fast molecular motions average these anisotropic interactions to isotropic or residual values which can be zero. Detailed description of the properties of these spin interactions can be found in References 1–9.

In the studies of elastomers by NMR experiments dipolar and quadrupolar interactions have been mainly used. The presence of the high magnetic field already imposes a manipulation of the spin system which separates certain parts of the spin interaction Hamiltonian. This process is called truncation and the secular dipolar Hamiltonian of two spins I and S has the general form

$$H_{\mathrm{d}}^{(0)} = -\left(\frac{\mu_0}{4\pi}\right)\frac{\gamma_I\gamma_S}{r^3}\frac{1}{2}(3\cos^2\theta_{IS} - 1)(3I_zS_z - \vec{I}\cdot\vec{S}) \qquad (5)$$

The factor $\mu_0/4\pi$, where μ_0 is the magnetic susceptibility of vacuum has been introduced in conformity with MKSA units. The magnetogyric ratios are γ_I and

γ_S. The spin operators are denoted by $\vec{I}$ and $\vec{S}$. The space encoded part of the dipolar Hamiltonian depends on the distance r of spins I and S and the angle θ_{IS} between $\vec{r}$ and $\vec{B}_0$. The anisotropic segmental motions average the space part of $H_{\mathrm{d}}^{(0)}$ to a residual value.

Finally, the truncated form of the axially symmetric quadrupolar Hamiltonian for nuclei with spin I larger than 1/2 can be expressed as

$$H_{\mathrm{Q}}^{(0)} = C_{\mathrm{Q}}\left[3I_z^2 - \vec{I}^{\,2}\right] \tag{6}$$

The quadrupolar coupling C_{Q} is defined by

$$C_Q = \frac{eQV_{\mathrm{ZZ}}}{4hI\,(2I-1)} \tag{7}$$

where eQ is the quadrupolar moment of a specific isotope and V_{ZZ} is the Z component of the electric field tensor at the position of the nucleus. In the presence of anisotropic molecular motions, the electric field gradient tensor is averaged to a residual value.

The spin interactions can be classified as inhomogeneous and homogeneous (4). The NMR spectrum generated by the inhomogeneous spin interaction which is linear in the spin operator I_z, is a sum of independent individual lines. A selective rf irradiation can saturate only a group of spins producing a hole in the spectrum. For homogeneous lines the NMR spectrum is a sum of individual lines with no shift with respect to each other. The spin interactions bilinear in the spin operators generate these spectra. The excitation of the spectrum with a selective pulse will affect all the spectral frequencies.

Magnetization Relaxation. One of the important sources of information about molecular motions is related to the relaxation of the longitudinal (M_z) and transverse (M_x and M_y) components of the macroscopic nuclear magnetization. The molecular motions modulate the spin interactions that lead to the exchange of energy between the nuclear energy levels and the lattice or thermal bath represented by the molecular degree of freedom. This process is described by a time constant T_1 the so-called longitudinal relaxation time. The dephasing of the transverse magnetization components M_x and M_y, which is related to the increase of the entropy of the spin system is described by the transverse relaxation time T_2.

The molecular motions responsible for the relaxation include: (*1*) overall translational or rotational motions, (*2*) local motions such as internal rotations around C—C bonds or molecular axis of symmetry or segmental motions of polymer chains, and (*3*) exchange between two different distinct chemical sites within the same molecule or different molecules.

In the simplest assumption, the time evolution of the nuclear magnetization under relaxation processes can be described by the Bloch equations (see (19), and

references therein)

$$\frac{dM_{x,y}(t)}{dt} = \frac{M_{x,y}(t)}{T_2}$$
$$\frac{dM_z(t)}{dt} = -\frac{M_z(t) - M_0}{T_1} \tag{8}$$

where M_0 is the magnetization of the spin system in the thermodynamic equilibrium. The time evolution of $\vec{M}(t)$ vector under relaxation processes described by equation 8 is given by exponential functions. This approximation is not valid in many cases for polymer or other macromolecular systems where complex relaxation mechanisms are present (23,24). In such cases, a complete treatment requires additional relaxation parameters such as cross-relaxation or cross-correlation rates (1,23–25). Such a situation occurs whenever two spins A and X interact by a random fluctuating spin interactions. For this cross-relaxation process A spins magnetizations induces a modification of X magnetization which add up to the specific evolution of X magnetization. More formally, this coupling can be expressed via the Solomon equations (see for instance, Reference 25) which contain besides the longitudinal relaxation rates of spins A and X also cross-relaxation rate which reflects the coupling between the A and X spin magnetizations. Several two-dimensional NMR experiments (see below) can measure cross-relaxation rates that enhance our knowledge about molecular motions in complex systems (1,25).

The longitudinal magnetization relaxation can be measured using different methods (5,18,19,25) based on the scheme:

$$\text{Initial perturbation} - \text{Evolution}\ (\tau) - \text{Detection}$$

The initial perturbation brings the spin system in a state on nonequilibrium and can be represented by an inversion pulse of 180° (ie, $M_z(0) \rightarrow -M_0$) or a saturation train of 90° pulses (ie, $M_z(0) = 0$). The detection is performed by a standard 90° pulse under low or high resolution conditions.

The transverse relaxation measurements are performed using a Hahn echo (see below) or Carr–Purcell–Meiboom–Gill (CPMG) pulse sequences (18,19). The first method uses the pulse scheme: $90^\circ_x - \tau - 180^\circ_{x,y} - \tau -$ Hahn echo and measure the time evolution of the amplitude of the Hahn echo as a function of echo time 2τ. CPMG scheme, $90^\circ_x - [\tau - 180^\circ_y - \tau -$ Hahn echo$]_N$ allows measuring the transverse magnetization decay in a single scan using a train of N Hahn echoes.

The mechanisms of relaxation are produced by local magnetic fields originating from randomly fluctuating spin interactions like homonuclear or heteronuclear dipolar, quadrupolar or chemical shielding interactions. They would induce quantum-mechanical transitions in the Zeeman energy levels manifold whose effect would be to take the nuclear magnetization back to the equilibrium configuration. When performing a spectra decomposition of these fluctuating local fields $\vec{h}(t)$ (which are in general, tensorial quantities), we can find a nonzero component frequencies equal to those of the various transitions which can exist within the Zeeman energy level diagram. Efficiency of the local magnetic fields to induce

transitions can be appreciated by the quantities named spectral densities of the form

$$J_i(\omega) = \int_0^\infty \overline{h_i(t)h_i(0)}\, \exp(-i\omega t)\, dt \tag{9}$$

where $h_i(t)$ is the random fluctuating i component of local fields. The bar denotes an average over the ensemble of spin systems. On the other hand, a quantum-mechanical transition can be induced by a fluctuating local field at the condition that a certain degree of coherence is present. The autocorrelation function $C(t) = \overline{h_i(t)h_i(0)}$ is indicative of this coherence that essentially persists for a time equal with the correlation time τ_c. A more general correlation function is represented by space–time autocorrelation function $C(\vec{x}, t)$, where $\vec{x}$ is a general spatial coordinate meant to represent translational or rotational coordinates. These correlation functions will turn out to be necessary in the context of characterization of two-dimensional (2D) exchange spectra (2). Moreover, a three-dimensional (3D) spectrum, being a three-time distribution, contains information that cannot be directly retrieved from the 2D spectrum. The detailed information on the nature of the nonexponential loss of correlation in polymers obtained from reduced four-dimensional (4D) exchange spectrum is also not accessible in the corresponding one-dimensional relaxation measurements and the 2D exchange spectrum (2).

Molecular processes with a single correlation time are rarely found in partially or strongly disordered solids like semicrystalline or amorphous polymers. A distribution of the correlation times $g(\tau)$ has to be introduced in order to evaluate the correlation function (2), ie,

$$C(t) = \int_0^\infty \exp\left\{-\frac{t}{\tau}\right\} g(\tau)\, d\tau \tag{10}$$

Such distribution has been shown to span several orders of magnitude for instance in the case of local motions in the glassy state. Instead of the distribution function, other fitting functions for correlation function $C(t)$ are considered. One of these functions is the stretched exponential Kohlraush–Williams–Watts function $\exp\{-(t/\tau_{\mathrm{kww}})^\beta\}$ that has been found to fit the data quite universally (2).

Spin Coherences. In all NMR experiments the spin system evolves under internal and external spin interactions. For isolated spins, the spin dynamics can be described in terms of the motion of classical magnetization vectors. Many structural and molecular dynamics problems in NMR involve couples spins. In this case, it is necessary to recourse to a quantum—mechanical formalism where a density operator describes the state of the system (1).

The density operator $\rho(t)$ is a generalized wave function which describes a so-called mixed state. This state corresponds to a statistical ensemble of quantum-mechanical objects, which in our case is a collection of nuclei with magnetic moments. Therefore, the statistics specific of these objects and the statistics of an ensemble are simultaneously present.

The equation of motion for the density operator is given by Liouville–von-Neumann equation

$$i\frac{\partial\rho(t)}{\partial t} = [H(t), \rho(t)] \tag{11}$$

where $H(t)$ is the Hamiltonian or total energy operator of the system expressed in angular frequency units, which may itself be time dependent. In general, equation 11 does not have an exact solution. Several mathematical methods have been applied to obtain an approximate solution for $\rho(t)$ one of the most efficient and accurate being the Floquet technique (1). The dynamics of the spin system detected via an observable $\langle O(t)\rangle$ described by a quantum-mechanical operator O can be evaluated by

$$\langle O(t)\rangle = \mathrm{Tr}\{O\rho(t)\} \tag{12}$$

Thus, the expectation value is found by evaluating the trace of the product of the observable operator and the density operator.

A particularly simple interpretation of the density matrix is possible in the eigenbase of the Hamiltonian H. The diagonal element ρ_{rr} is equal to the probability that the spin system is found in the eingenstate $|r\rangle$. The population of state $|r\rangle$ is P_r and therefore, $\rho_{rr} = P_r$. The off-diagonal element is defined by

$$\rho_{rs} = \langle r|\rho(t)|s\rangle = \overline{c_r(t)c_s^*(t)} \tag{13}$$

where the bar indicates an ensemble average. These elements describe a "coherent superposition" of eigenstates $c_r(t)|r\rangle + c_s(t)|s\rangle$ in the sense that the time dependence and the phase of the various members of the ensemble are correlated with respect to $|r\rangle$ and $|s\rangle$. Such a coherent superposition is simply called "coherences". A spin coherence can be associated with a transition between two eigenvalues specified by the eigenstates $|r\rangle$ and $|s\rangle$. If the two states span an allowed transitions with a difference in magnetic quantum numbers $\Delta M_{rs} = M_r - M_s = \pm 1$, the coherences ρ_{rs} is related to the NMR observables represented by the transverse magnetization components $M_x^{(rs)} \pm iM_y^{(rs)}$. In general, a matrix element of the density operator ρ_{rs} represents p-quantum coherence for which $p = M_r - M_s$, which, for $p \neq \pm 1$, does not lead to observable magnetization and can only be detected indirectly by two-dimensional spectroscopy (1,26).

The density operator $\rho(t)$ has been formulated for the entire quantum-mechanical system. For magnetic resonance applications, it is usually sufficient to calculate expectation values of a restricted set of operators which act exclusively on nuclear variables. The remaining degrees of freedom are referred to as "lattice". The reduced spin density operator is defined by $\sigma(t) = \mathrm{Tr}_1\{\rho(t)\}$, where Tr_1 denotes a partial trace over the lattice variables. The reduced density operator can be represented as a vector in a Liouville space of dimension

n^2, ie,

$$\sigma(t) = \sum_{r}^{1,n^2} b_r(t) B_r \tag{14}$$

where n is the dimension of the Hilbert space of all admissible state functions and $\{B_r\}$ is a complete set of orthogonal base operators. A proper selection of this base is often essential to ease the solution of a particular spin dynamics problem. For instance, for systems with spins $I_k = 1/2$ the product of the Cartesian spin operators is a convenient base operators (1,27). As an example, the complete set of product operators $\{B_r\}$ for two J or dipolar coupled nuclei with spin $I = 1/2$ consists of $2^{2\times 2} = 16$ operators, ie,

$$\frac{1}{2}E \text{ (E is the unity operator)}, I_{ix}, I_{iy}, I_{iz}$$

$$2I_{ix}I_{jx}, 2I_{iy}I_{jy}, 2I_{iz}I_{jz}, 2I_{ix}I_{jy}, 2I_{ix}I_{jz}, \text{ for } i,j = 1,2 \tag{15}$$

The spin modes described by the product operators of equation 15 are the matrix elements of the density operator

$$\rho = \begin{pmatrix} P_1 & \text{SQ} & \text{SQ} & \text{DQ} \\ \text{SQ} & P_2 & \text{ZQ} & \text{SQ} \\ \text{SQ} & \text{ZQ} & P_3 & \text{SQ} \\ \text{DQ} & \text{SQ} & \text{SQ} & P_4 \end{pmatrix} \tag{16}$$

The above product operators can be detected by a proper design NMR experiment (1,26) and reflect different features of the spin systems related to the structure, spin interaction topology, and molecular dynamics. The most popular spin modes are represented by single-quantum coherences (SQ) of spin i, I_{ix} and I_{iy} that are related to x- and y-magnetizations, respectively. Two-spin coherences of spin i and j consist of superposition of $p = 0$ (zero-quantum (ZQ)) and $p = \pm 2$ (double-quantum (DQ)) quantum coherences. The former is insensitive to the inhomogeneity of the magnetic field and the latter is reflecting the existence of spin couplings. Not only the existence of J- or dipolar couplings can be detected by editing DQ coherences but also the strength of these couplings can be measured including internuclear distances and dihedral angles (27–29).

Spin-Echoes. The evolution of spin coherences under nonfluctuating spin interactions is a reversible process. The strength and sign of the spin Hamiltonians can be manipulated by rf pulses and/or sample rotation such that the evolution of the spin system during a period of time is refocused during the spin system evolution at a latter time.

The spin interactions described by inhomogeneous or homogeneous spin Hamiltonians lead to inhomogeneous and homogeneous spin-echoes. If a linear superposition of both types of spin Hamiltonians is present, a mixed spin-echo can be generated. The most common used inhomogeneous echoes are: Hahn (30),

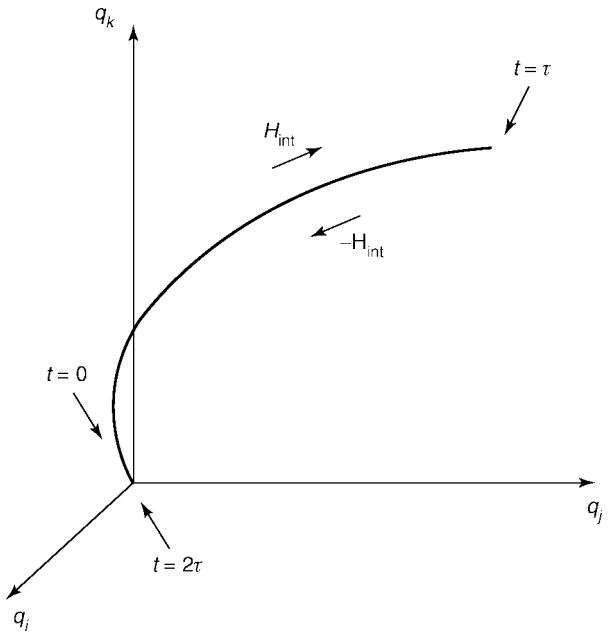

Fig. 3. Evolution of the quantum-mechanical state of a spin system in a Liouville space. The evolution from the initial time $t = 0$ to an intermediate time $t = \tau$ takes place under a Hamiltonian H_{int} which describes internal and external spin interactions. At this time, a pulse sequence change the sign of the spin Hamiltonian. The spin system evolves on the same generalized trajectory and after total evolution time $t = 2\tau$ the initial state is refocused under a spin echo.

stimulated (30), and gradient echoes (5,18). Solid (31) and magic (32–34) echoes are the most familiar types of homogeneous echoes.

In order to understand how a spin echo can be produced, we shall consider a spin system composed of N nuclei, which interact, or not between themselves. The quantum-mechanical state of such a system can be described by a linear superposition of spin coherences represented by a vector evolving in a Liouville space of dimension 2^{2N} (cf Fig. 3). In this abstract space, the state of the spin system at time $t = 0$ is represented by a configurational point. This state corresponds in many cases to the single-quantum coherences excited after a 90° rf pulse. The spin system evolves in laboratory or rotating reference frames for a time τ, evolution described by the propagator operator $E_{\text{evolution}} = \exp\{-\text{i}H_{\text{int}}\tau\}$, where H_{int} is the spin-interaction Hamiltonian. At the end of this evolution period, a pulse or a complex pulse sequence is applied which change the sign of the Hamiltonian H_{int}. During the refocusing period of duration τ the evolution operator is now $E_{\text{refocusing}} = \exp\{-\text{i}(-H_{\text{int}})\tau\}$. This is formally equivalent with a time reversal, ie, $\tau \rightarrow -\tau$. For the full evolution period 2τ, the propagator is $E_{\text{evolution}}\, E_{\text{refocusing}} = E$, where E is the unity operator and the spin system is reaching the initial state. Hence, a spin echo was generated with an amplitude identical with the free induction decay as long as the magnetization relaxation processes are neglected.

The pulse sequence used for generation of inhomogeneous spin-echo of the Hahn type is shown in Fig. 4**a**. The spin systems for which this echo can be

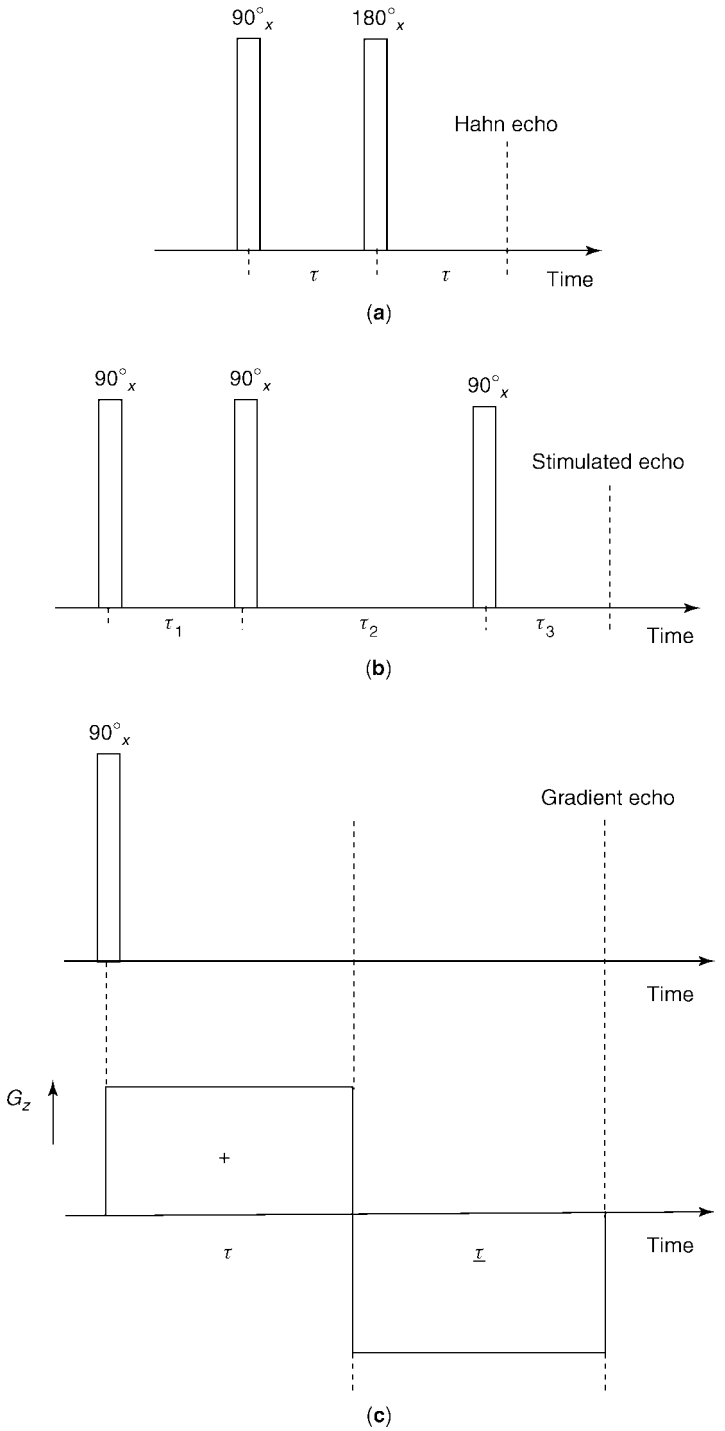

Fig. 4. Pulse sequences used for Hahn echo (**a**), stimulated echo (**b**), and gradient echo (**c**) are shown.

produced are characterized by the Hamiltonian $H_{\text{int}} = -\delta I_z$, where δ describes the inhomogeneity of the magnetic fields or chemical shift distributions. By the action of refocusing 180°_y pulses, the spin operator I_z becomes $-I_z$ and the spin Hamiltonian changes the sign, ie, $H_{\text{int}} = -H_{\text{int}}$. If the transverse magnetization relaxation is neglected, the amplitude of the Hahn echo is equal with the amplitude of the free induction decay generated after 90°_x preparation pulse (cf Fig. 4**a**). The relaxation encoding is given by the factor $\exp\{-2\tau/T_2\}$, where T_2 is the transverse relaxation time. The Hahn echo represents an important tool for measuring residual dipolar couplings, correlation function of molecular motions, and encoding of spatial information and mass transport. If the 180°_x pulse is split in two 90°_x pulses separated by a time τ_2 (cf Fig. 4**b**), a stimulated echo is produced at time τ_1 after the action of the last pulse. This spin-echo has under ideal conditions the amplitude half of the amplitude of FID and the lifetime is much longer compared with that of the Hahn echo. Therefore, it is an ideal instrument for measuring self-diffusion coefficients.

The scheme used for gradient echo is presented in Figure 4**c**. The evolution of the single-quantum excited by a preparation 90°_x pulse under a field gradient G_z is refocused by the filed gradient with the opposite direction $-G_z$. The amplitude of the echo is affected by the presence of the magnetic field gradients inside the sample. This effect is exploited for enhancement of the contrast in MRI.

In many rigid or soft polymers, the protons are dipolar coupled in a complex network. The dipolar Hamiltonian is bilinear in spin operators representing a homogenous interaction. Pulse sequences can be designed that change the sign of the dipolar Hamiltonian H_{d}, ie, $H_{\text{d}} \rightarrow -kH_{\text{d}}$, where k is a scaling factor. An example of such a homogeneous spin-echo is given by magic echo for which $k = 1/2$ (cf Fig. 5**b**). The most simple homogeneous spin echo is represented by solid echo

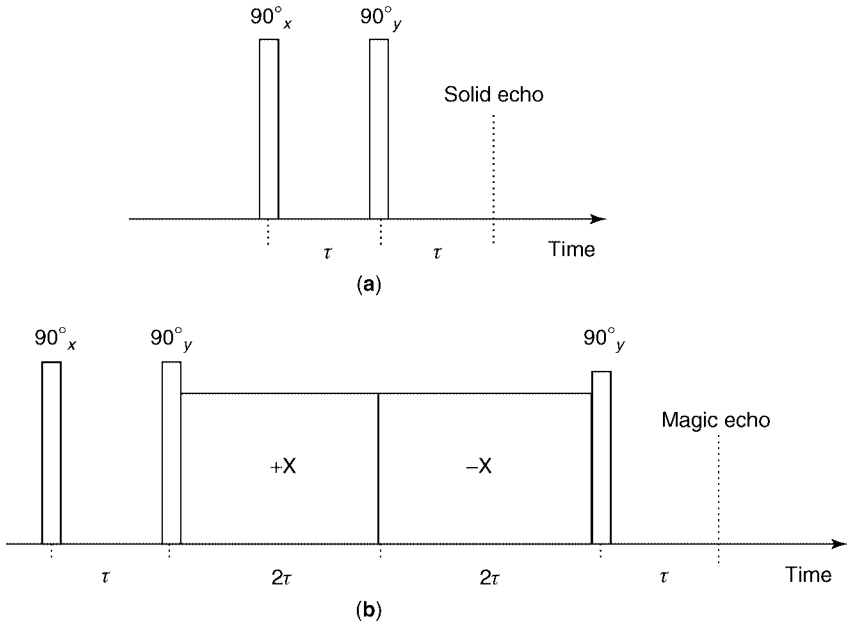

Fig. 5. Pulse sequences used for solid echo (**a**) and magic echo (**b**) are shown.

(Fig. 5**a**). For a spin system composed of spin-1/2 pairs the spin evolution is fully refocused by the solid echo. This is not the case for a multispin dipolar network. These echoes can be used for high resolution NMR spectroscopy of solids, measurement of residual spin interactions, and NMR imaging of rigid polymers.

Two-dimensional Fourier Spectroscopy. Two-dimensional (2D) spectroscopy is a general concept that can be applied to different brunches of spectroscopy which make it possible to acquire more detailed information about the molecular system under investigation. Since the first proposal in the 1971 (35) and the first experimental realization in the 1974 (36–38) a large number of 2D NMR methods have been invented and applied (1) to solve structural and dynamical problems in physics, chemistry, biology, and medicine.

Several strategies can be employed for obtaining a 2D spectrum, which is a signal function $S(\omega_1, \omega_2)$ of two independent frequency variables (ω_1, ω_2) (1). The most popular one is based on the 2D time-domain experiments. In this approach, a time-domain signal $s(t_1, t_2)$ is obtained by incrementing the time interval t_1 parametrically from experiment to experiment, and recording the free induction signal as a function of t_2. In a general case, for a 2D experiment, we distinguish four intervals:

$$[\text{Preparation } (t_p)]-[\text{Evolution } (t_1)]-[\text{Mixing } (t_m)]-[\text{Detection } (t_2)]$$

The four basic intervals have the following qualitative features: (*1*) *Preparation period*: In the course of this period of fixed length the spin system is prepared in a coherent nonequilibrium state. In the simplest experiments, the preparation periods consists of a single rf pulse. However, this period can involve more sophisticated procedures like cross-polarization (39,40) and excitation of multiple-quantum coherences (1,41). (*2*) *Evolution period*: During this period, in general, the spin system evolves under a spin Hamiltonian, which may be modified by heteronuclear decoupling (42), sample spinning (43,44), or homonuclear decoupling pulse sequences (45,46). The evolution during this indirect dimension of the 2D experiment determines the frequencies in the ω_1-domain. (*3*) *Mixing period*: This period may consists of one or more rf pulses, separated by intervals with fixed or variable durations. During the mixing period, transfer of coherences or polarization can take place. For instance, mixing process transforms single (SQ)-, multiple (MQ)- or zero-quantum (ZQ) coherences into observable transverse magnetization. In many cases, the 2D spectrum may be regarded as a visual representation of the pathways of the mixing process. (*4*) *Detection period*: In the course of the detection period, the SQ coherences evolution is measured as a function of time-domain variable t_2. The spin system can be manipulated by the action of coherent averaging pulse sequences and/or sample spinning, or by polarization transfer to nuclei with higher sensitivity. Finally, a complex 2D spectrum is obtain for the time-domain data by a complex 2D Fourier transformation defined by

$$S(\omega_1, \omega_2) = \int_{-\infty}^{\infty} \mathrm{d}t_1 \exp\{-\mathrm{i}\omega_1 t_1\} \int_{-\infty}^{\infty} \mathrm{d}t_2 \exp\{-\mathrm{i}\omega_2 t_2\} s(t_1, t_2) \tag{17}$$

The major advantages of 2D NMR spectroscopy are related to the assignment of complex spectra, of revealing the correlated transitions to establish J- or dipolar

coupling topologies or for studying complex dynamic processes. These features lead to a classification of 2D spectroscopic experiments in three groups (1).

The interpretation of NMR spectra is often impeded by the complexity of overlapping resonances. When the interactions responsible for the multiplet structure are different such as chemical shielding, dipolar, or scalar couplings, it is often possible to render spectra more intelligible by *separating* various interactions in orthogonal frequency domains. In the course of *2D separation* experiments the number of peaks is conserved.

The second group of 2D experiments is represented by *2D correlation* methods based on coherence transfer. These experiments allow interpretation of NMR spectra of networks of coupled spins by establishing the connectivities of nuclear spins coupled by J or dipolar interactions. The appearance of cross-peaks in 2D correlation spectra constitutes a proof of the existence of resolved scalar or dipolar couplings, and allows one to correlate the chemical shifts of coupled partners. These experiments are designed to correlate transitions of coupled spins by transferring magnetization of MQ coherences from one transition to another in the course of a suitable designed mixing process.

A third class of 2D time-domain experiments is concerned with studying *dynamic processes* such as cross-relaxation, nuclear Overhauser effects, chemical exchange, and magnetization exchange including spin diffusion (1,2). These methods have a number of advantages particularly when the system comprises an extended network of exchange processes that occur simultaneously. Moreover, the 2D methods are most useful for studying slow dynamic processes with rates that are two low to affect the lineshapes. The basic idea of 2D exchange spectroscopy is the "frequency labeling" of the longitudinal magnetization of various chemical sites before chemical or magnetization exchange takes place, such that after exchange the pathways of the magnetization can be traced back to their origins.

The magnetic resonance imaging (MRI) techniques used most frequently for applications to soft polymers are directly related to the multidimensional Fourier transform (5,18,19,47). Just like in 2D spectroscopy, the phase of the signal acquired during the detection period (time domain t_2) is modulated by the coherence phases present in the evolution period (t_1). The idea is that the accumulated signal phase is primarily a result of the applied gradient which induces a position encoding. A 2D Fourier transformation then produces a 2D image of the object.

One-Dimensional NMR Studies of Molecular Motions and Dynamic Order

NMR methods can probe molecular dynamics in polymers on various time scales from relatively fast segmental motions (with correlation times of the order of 10^{-10} s) down to slow motions in the 10^{-3} s range or even slower (2–6,48). Dynamics in the range of around 10^{-10} s can be investigated by T_1 measurements that are sensitive to motions around the Larmor frequency. Particularly useful for such investigations is the field cycling technique, where the magnetic field and thus also the Larmor frequency ω can be varied over several orders of magnitudes

down to the 10 kHz regime. By acquiring $T_1(\omega)$, molecular dynamics can be probed over the corresponding range ((5), and references therein).

Slow motions can be studied using so-called longitudinal relaxation in the rotating frame ($T_{1\rho}$) (5). In these experiments, a radio-frequency field ("spin-lock pulse") with field strength of around 10–100 kHz plays the same role as the main magnetic field does for T_1. For instance, the changes in the phase structure under mechanical deformation of thermoplastic elastomers have been investigated by $T_{1\rho}$ measurements of ^{13}C nuclei under MAS (49).

Transverse relaxation (T_2) and lineshape analysis has also been the topic of many studies of molecular dynamics in viscoelastic media ((12,13,50,51), and references therein). It was found to be indicative of heterogeneities of molecular motions (12,13). Transverse relaxation curves therefore often turn out to be composed of a superposition of multiexponential and the Gaussian decays. Measurement of residual dipolar couplings, molecular motions, and other parameters have been performed by this relaxation technique on different nuclei like ^{1}H, ^{13}C, ^{15}N, ^{31}P, and ^{29}Si and could be related to material properties such as the cross-link density (12,13). In order to separate the liquid-like and solid-like contributions of the T_2 decay, a linear combination of Hahn echoes and solid echoes have been used (52,53). While Hahn spin-echo amplitudes are encoded by irreversible dephasing due to molecular motions and by reversible residual dipolar couplings, only the first effect encodes the amplitudes of solid echo (actually mixed echo) to first approximation. The appropriate combination of these spin-echoes thus gives access to residual dipolar couplings and the fluctuation rate (52,53). The method was applied to measure the degree of segmental order induced in natural rubber upon stretching (53).

A powerful technique for the study of orientation and dynamics in viscoelastic media is lineshape analysis in deuteron NMR spectroscopy (2,50,51,53). Recent reviews on this topic were published (50,51). For instance, the average orientation of chain segments in elastomer networks upon macroscopic strain can be determined by this technique (54–60). For a nondeformed rubber, a single resonance line in the deuterium NMR spectrum is observed (57) while the spectrum splits into a well-defined doublet structure under uniaxial deformation. It was shown that the usual network constraint on the end-to-end vector determines the deuterium lineshape under deformation, while the interchain (excluded volume) interactions lead to splitting (57–60). Deuterium NMR is thus able to monitor the average segmental orientation due to the cross-links and mean field separately (60).

The network structure of unfilled and filled elastomers was probed by the analysis of the quadrupolar splitting in ^{2}H solid echo spectra of uniaxially strained samples (55) (see Fig. 6). The local chain order at a given elongation is larger by a factor of 1.5–2 in the filled system. A decrease of local chain mobility in the absorption layer is observed under stress. The same method was applied to investigate molecular dynamic in thermoplastic elastomer based on hydrogen bonding complexes (61,62).

The 1D NMR techniques described above already allow a detailed investigation of polymer dynamics but they are mostly not selective in the sense that they do not provide information on the averaging of particular couplings. For the interpretation of some of the above results therefore a representative spin pair

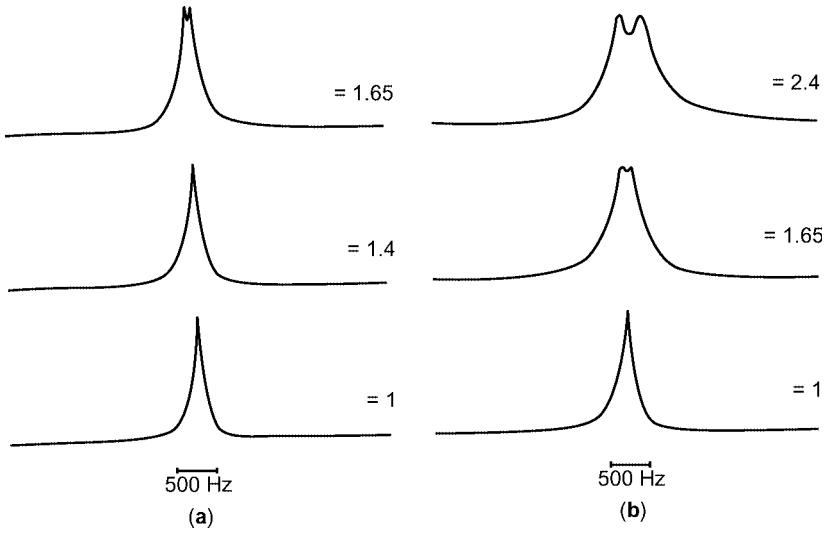

Fig. 6. Deuterium solid echo spectra of unfilled (**a**) and filled (**b**) poly[dimethylsiloxane] networks at 305 K with and without mechanical stress as given by the parameter λ. Reproduced from Ref. 55, with permission from Wiley-VCH.

along the chain was assumed, thus neglecting local site-specific motions as well as the geometry of the bonds. This is where multidimensional NMR techniques come into play.

Residual van Vleck Moments. The difficulties related to these measurements are due to the small values of the residual spin couplings compared to those of other spin interactions, the many-body character of the dipolar couplings and the presence of molecular motions which produce a supplementary encoding of the spin system response.

One-dimensional (1D) NMR methods based on the dipolar correlation effect in combination with the Hahn and solid echoes (52,63), the stimulated echo (5), the magic echo (64), magnetization-exchange (65), and cross-relaxation dynamics (66) provide access only to the second van Vleck moment via a model which takes into account the solid-like and liquid-like contributions to the spin system response (67). Model free access is given by the analysis of multiple-quantum builtup (68) and decay (69) curves recorded in the initial regime of the excitation/reconversion periods.

In the following, we discuss a method to measure model free the residual dipolar van Vleck moments without contributions from inhomogeneous spin interactions originating from static magnetic field inhomogeneities, local susceptibility effects, and heteronuclear dipolar interactions (70). Moreover, in the first approximation this method is insensitive to the transverse relaxation produced by the fluctuating dipolar interactions.

Principles of the Method. The method is based on the mixed echo composed of the Hahn and the magic echo (33,71,72). The Hahn echo explores the magic echo shape generated by an accordion magic sandwich (cf Fig. 7).

One possibility to have the amplitude of the Hahn echo encoded by the homonuclear dipolar interactions is to employ a mismatched magic sandwich

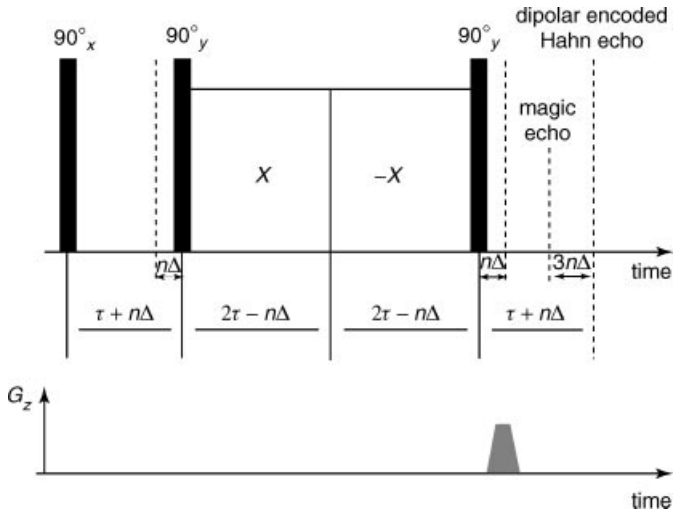

Fig. 7. AIMS pulse sequence used for generation of a mixed echo composed of a magic and a Hahn echo. A dephasing gradient pulse is applied at the end of the sequence. Reproduced from Ref. 70, with permission from Elsevier.

(MS), ie, $90^{\circ}_{x} - (\tau + n\Delta) - 90^{\circ}_{y}$ – Burst Pulse$_{x}$ $(2\tau - n\Delta)$ – Burst Pulse$_{\overline{x}}$ $(2\tau - n\Delta)$ – $90^{\circ}_{y} - (\tau + n\Delta)$ – Mixed Echo (see Fig. 7), where n is a positive and negative integer number and Δ is the time decrement and increment, respectively. We call this mismatched MS composite pulse with variable n the *accordion magic sandwich* (hereafter the method will be called AIMS).

The spin system response to the AIMS sequence was evaluated in Reference 70 for a multispin dipolar network characteristic to elastomers and other soft polymers. It was shown that the normalized amplitude of the Hahn echo measured at time $t = 6\ \tau$ is encoded only by the homonuclear dipolar couplings and relaxation, ie,

$$\frac{S(3n\Delta)}{S(0)} = \frac{\mathrm{Tr}\left\{I_y \exp\left\{-\mathrm{i}\hat{\bar{H}}_d^{(0)}(3|n|\Delta)\right\}I_y\right\}}{\mathrm{Tr}\{I_y^2\}} \exp\left\{-2n\Delta\left(\frac{1}{T_2^*} - \frac{1}{T_{2\rho}^*}\right)\right\} \tag{18}$$

where T_2^* and $T_{2\rho}^*$ are the effective transverse relaxation times in the laboratory and rotating frames, respectively. It is easy to see from the above equation that a combination of signals taken with $+|n|$ and $-|n|$ is given by

$$\frac{S(3|n|\Delta)S(-3|n|\Delta)}{S(0)^2} = G(3|n|\Delta)^2 \tag{19}$$

This composite NMR signal is not encoded by the transverse relaxation. The function $G(t)$ describes the magic echo shape and is given by (4)

$$G(t) = \frac{\mathrm{Tr}\left\{I_y \exp\left\{-\mathrm{i}\hat{\bar{H}}_d^{(0)} t\right\}I_y\right\}}{\mathrm{Tr}\{I_y^2\}} \tag{20}$$

In the short-time limit, ie, for $3|n|\Delta\omega_d \ll 1$, we obtain from the above equations,

$$\frac{S(3|n|\Delta)S(-3|n|\Delta)}{S(0)^2} \cong 1 - \bar{M}_2(3|n|\Delta)^2 + \frac{1}{12}\bar{M}_4(3|n|\Delta)^4 - \cdots \quad (21)$$

where $\bar{M}_2$ and $\bar{M}_4$ are the residual second and forth van Vleck moments, respectively (4).

In conclusion, the AIMS pulse sequence produces a disentanglement of the magic and Hahn echoes in time. The dipolar encoding of the signal occurs because the Hahn echo samples the magic echo shape.

^1H Residual van Vleck Second Moments of Cross-Linked Series of Natural Rubber. Proton residual second and fourth van Vleck moments were measured by AIMS for the samples of cross-linked series of natural rubber (NR). The residual van Vleck moments $\bar{M}_2$ and $\bar{M}_4$ can be evaluated by the best fits of the composite signals with equation 21 and these results are shown in Figures 8**a** and 8**b**, respectively, for the whole NR series.

The measured values of $\bar{M}_2$ are in good agreement with the values measured on the same series using the model dependent dipolar correlation function (64). The best fit of the dependence of $\bar{M}_2$ and $\bar{M}_4$ on shear modulus G is given by continuous lines in figures 9**a** and 9**b**. These are described, in general, by a polynomial $\sum_1^m (-1)^p a_p G^p$ up to the powers four and eight in G, respectively. This polynomial dependence can be justified by considering high order corrections to a Gaussian distribution of the end-to-end vectors (68). The classical Gaussian distribution will lead only to dependences of powers two and four in G which are shown by the dashed lines in these figures. Nevertheless, in the case of samples with low values of the cross-link density the Gaussian approximation is able to describe the experimental data sufficiently well (see the insets of figures 8**a** and 8**b**). These results also show that high order van Vleck moments are more sensitive to cross-link density compared to the second van Vleck moment which is usually used.

The value of the ratio $\bar{M}_4/\bar{M}_2{}^2$ on shear modulus is shown in figure 8**c**. The ^{1}H NMR absorption lineshape is quasi-Lorentzian for all samples but starts to deviate towards a Gaussian lineshape for higher values of the cross-link density.

Residual Dipolar Couplings by ^{1}H Multiple-Quantum NMR. The measurements of residual dipolar couplings in elastomer system is desirable, because they reflect the hindrance to molecular motions by the cross-linking, topological constraints, and the external factors like mechanical stress. Dipolar-encoded longitudinal magnetization (DELM) NMR decay curves, double-quantum (DQ) and triple-quantum (TQ) NMR buildup intensities for measuring the residual dipolar couplings and the associated dynamic order parameters were discussed in Reference 68. These methods allow measuring residual dipolar couplings model free and in the limit of short excitation time regime the effective dipolar network is simplified.

Principles of the Method. One of the important features of the MQ spectroscopy is the possibility to edit the strongest dipolar couplings. This feature is based on the fact that the efficiency of MQ pumping is a nonlinear function of the dipolar coupling strength. For instance, the pumping efficiencies of DQ and TQ coherences in the initial excitation time regime are proportional to $(D^{ij})^2$

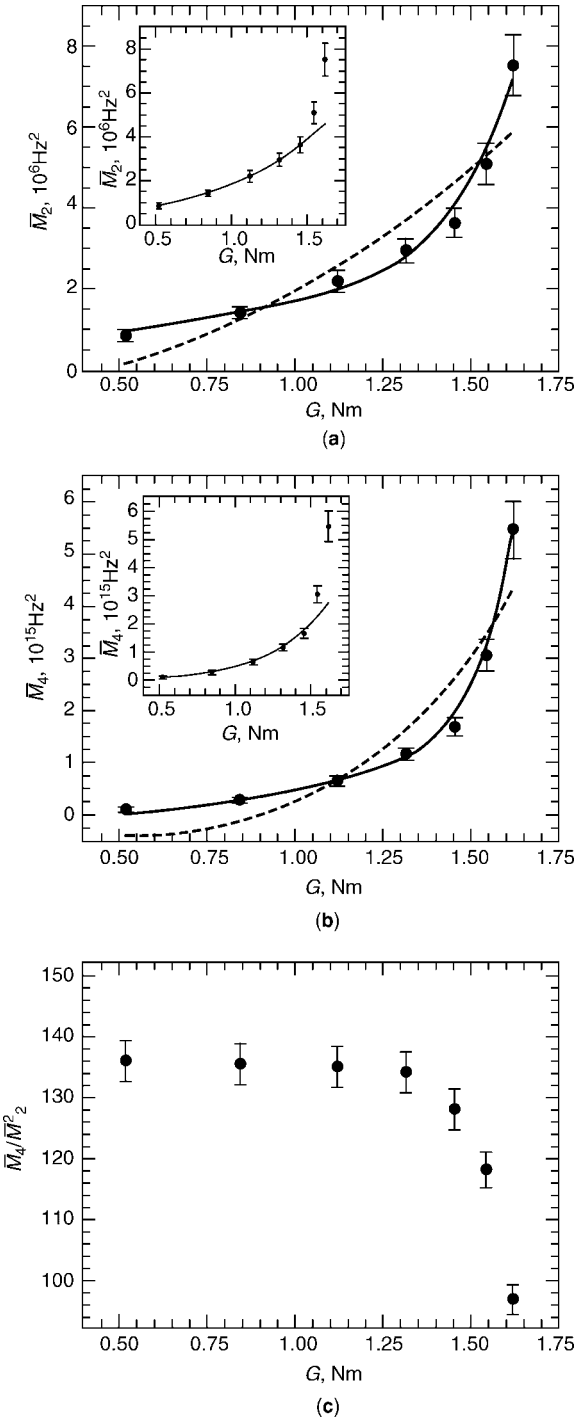

Fig. 8. Proton residual van Vleck moments $\bar{M}_2$ (**a**), $\bar{M}_4$ (**b**), and the ratio $\bar{M}_4/\bar{M}_2{}^2$ (**c**) measured by AIMS for the samples of a series of cross-linked natural rubber versus the shear modulus G. Reproduced from Ref. 70, with permission from Elsevier.

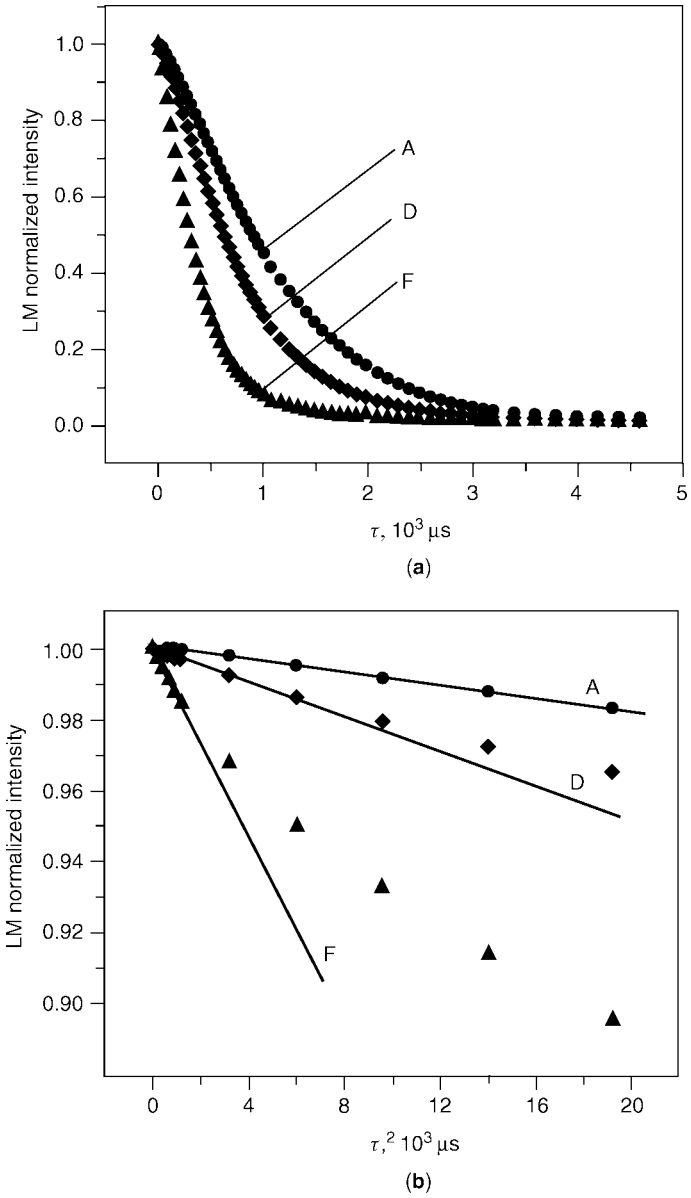

Fig. 9. (**a**) Proton dipolar-encoded longitudinal magnetization decay curves for a series of synthetic polyisoprene samples with different cross-link densities. (**b**) The initial time behavior of DELM decays exhibits a linear dependence in τ^2 (solid lines). Reproduced from Ref. 68, with permission from American Institute of Physics.

and $(D^{ij})^4$, respectively, where D^{ij} is the dipolar strength between protons i and j (73–75). Therefore, we can estimate that the pumping efficiency of DQ coherences for methylene protons is about six times higher compared to that of methyl protons. The editing capabilities are expected to be even better for the intergroup

dipolar interactions. In the case of TQ coherences, the maximum pumping efficiency is expected for the methyl group.

The possibility to implement a MQ dipolar filter has already been demonstrated. For instance, by use of a ^{13}C–^{13}C DQ dipolar filter working in the initial excitation time regime the signal of the crystalline domains in polyethylene could be enhanced (74). The possibility of functional group editing by MQ NMR methods is also supported by DQ experiments performed on static and rotating elastomers. The 2D ^{1}H DQ MAS spectrum of polyisoprene (68) shows that for short excitation times the response of the methylene protons can be approximated well by an isolated spin pair. Moreover, the experiment shows that the DQ coherences at which methyl protons participate are mainly originating from the CH_3 group. This also leads to the conclusion that TQ coherences excited in the initial time regime can be attributed mainly to the methyl groups. Weak dipolar coupling of CH_2 and CH_3 protons with CH protons is demonstrated (68). But, the contribution of the methine protons to the overall NMR signal is only about 12% so that these couplings are negligible in a good approximation.

The spin system response to the pulse sequence used for excitation of different multipolar spin states can be evaluated in the limit of short dipolar encoding time. For DELM, it is possible to write (68)

$$\begin{aligned} S_{\mathrm{DELM}}(\tau) \approx 1 - \left\{ l_2 \left[D^{(2)} S_s^{(2)} \right]^2 + l_3 \left[D^{(3)} S_s^{(3)} \right]^2 + \text{intergroup} \right\} \tau^2 - \cdots \\ \equiv 1 - [D_{\mathrm{eff}}]^2 \tau^2 - \cdots \end{aligned} \tag{22}$$

where the numerical coefficients are $l_2 = 21/80$, and $l_3 = 63/190$ and correspond to the CH_2 and CH_3 groups. D_{eff} is the effective residual dipolar coupling describing contributions from both CH_2 and CH_3 groups as well as intergroup residual dipolar couplings. Nevertheless, the residual dipolar couplings of methylene and methyl protons dominate the intergroup couplings and the slope of the LM decay curve versus the square of the excitation time τ is given by a weighted sum of the squares of dynamic order parameters of CH_2 and CH_3 groups.

The DQ signal can be evaluated in a similar manner, and finally one can write

$$\begin{aligned} S_{\mathrm{DQ}}(\tau) \approx \left(d_2 \left[D^{(2)} S_s^{(2)} \right]^2 + d_3 \left[D^{(3)} S_s^{(3)} \right]^2 + \text{intergroup} \right) \tau^2 + \cdots \\ \equiv [D'_{\mathrm{eff}}]^2 \tau^2 + \cdots \end{aligned} \tag{23}$$

where the numerical coefficients are $d_2 = 21/40$ and $d_3 = 9/200$. An effective residual dipolar coupling D'_{eff} similar (but not identical) to D_{eff} for dipolar encoded longitudinal magnetization can be introduced describing DQ-edited residual dipolar couplings.

In the regime of short excitation times the TQ coherences are derived mainly from the methyl protons. The spin system response to the pulse sequence (68) for a proton triad rotating rapidly around the C_3 axis in a static sample can be evaluated similar to the procedure used for DQ coherences. In the limit of short excitation

times, the normalized TQ-filtered signal is given by

$$S_{TQ}(\tau) \approx \left(r_3\left[D^{(3)}S_s^{(3)}\right]^4 + \text{intergroup}\right)\tau^4 + \cdots \equiv [D''_{\text{eff}}]^4\tau^4 + \cdots \quad (24)$$

where $r_3 = 39/4$. Again as above, an effective residual dipolar coupling D''_{eff} can be introduced for the full dipolar network. These effective residual dipolar couplings, introduced by the above equations, depend on the dipolar network edited by the experiments and it is therefore not easy to express them in terms of site-specific dynamic order parameters. Nevertheless, D''_{eff} is expected to be dominated by the methyl protons.

Dynamic Order Parameters. Dipolar-encoded longitudinal magnetization decay curves were measured for ^{1}H in a series of cross-linked synthetic polyisoprene samples (68). The decays for three samples (A, D, and F with the cross-link density of 0.75, 5.0, and 15.0, respectively) are shown in Figure 9.

The decay curves show a dependence on the cross-link density. In the short-time regime, the dipolar-encoded LM decays display a linear dependence in τ^2, in accordance with equation 22, (cf Fig. 9**b**). DQ buildup curves for the same samples are shown in figure 10 for the full range of excitation time τ. Systematic dependence of the DQ-filtered signal intensity on the cross-link density is evidenced in Figure 10**a**. Based on equation 23, an initial dependence of the signal amplitude on τ^2 will be shown by the DQ signals with a slope related to the scaled dynamic order parameters of methylene and methyl protons (cf Fig. 10**b**). TQ buildup curves for protons in polyisoprene also show a clear dependence on the cross-link density similar to the case of the DQ buildup curves.

Within the limit of experimental errors scaled dynamic order parameters measured from the MQ experiments show a linear dependence on cross-link density (cf Fig. 11).

This is expected because the dynamic order parameters $S_s^{(2)}$ and $S_s^{(3)}$ are inversely proportional to the number N of statistical segments. The same dependence on N is expected for cross-link density as measured in parts per hundred of rubber (phr) of cross-linking agent. For the whole series, the dynamic order parameters of methyl protons are slightly larger than those of the methylene protons. This reflects the hindrance imposed to the motion of methyl groups attributed to backbone chain by the short-range interactions between segments belonging to different chains in comparison with the case of the methylene proton located along the polymer chain.

The values of the effective ^{1}H residual dipolar couplings $D_{\text{eff}}/2\pi$ measured from the initial decays of the LM are shown as a function of cross-link density in Figure 11**b**. In the good approximation, the dipolar couplings are linearly proportional to cross-link density. These quantities can also be evaluated from equations 23 and 24 by using the dynamic-order parameters measured site-selectively from DQ and TQ buildup curves. These $D_{\text{eff}}/2\pi$ are plotted versus cross-linked density in Figure 11**b**, again showing a linear dependence on cross-linked density. They are systematically lower than the values measured from the LM

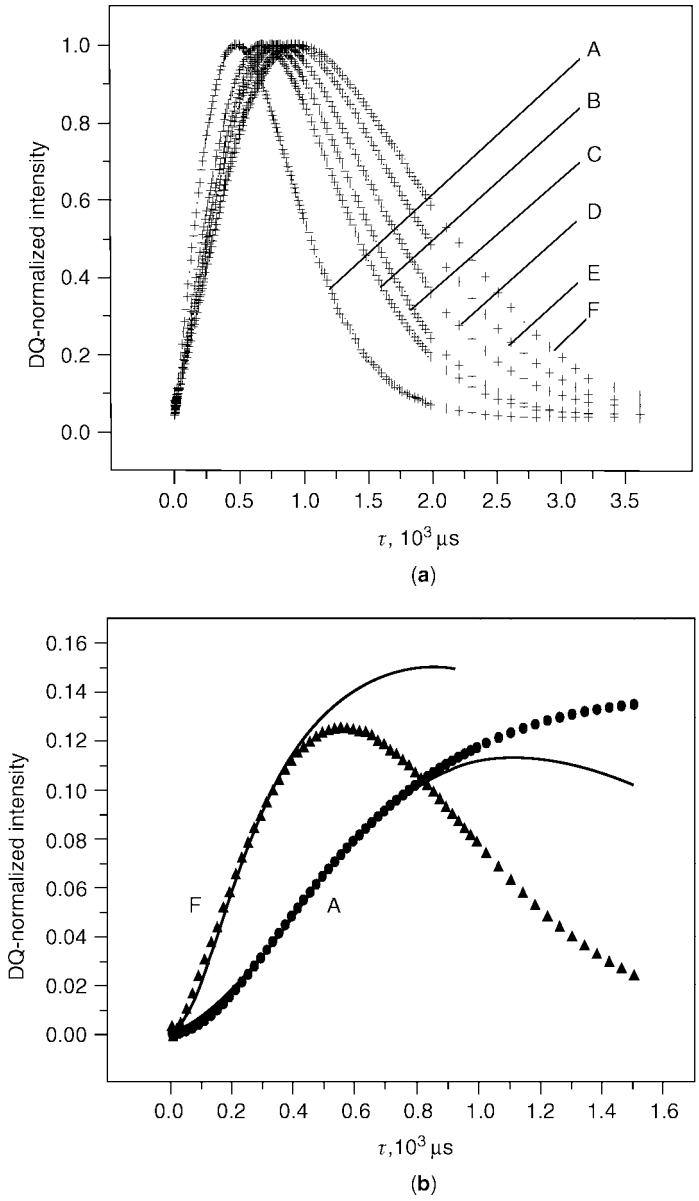

Fig. 10. Proton DQ buildup curves for a series of synthetic polyisoprene samples with different cross-link densities increasing from samples A to F. (**a**) The signal dependence on excitation and reconversion times τ for the full time domain. (**b**) The initial time regime of the DQ buildup curves for samples A and F together with the simulated curves including transverse relaxation (continuous lines). Reproduced from Ref. 68, with permission from American Institute of Physics.

decays. This fact can be due to the shorter time scale used for extraction of $D_{\text{eff}}/2\pi$ from LM decays compared to that used in DQ and TQ buildup curves.

The dynamic order parameters determined by the above methods can be compared to those measured by other NMR techniques if the specific dynamic

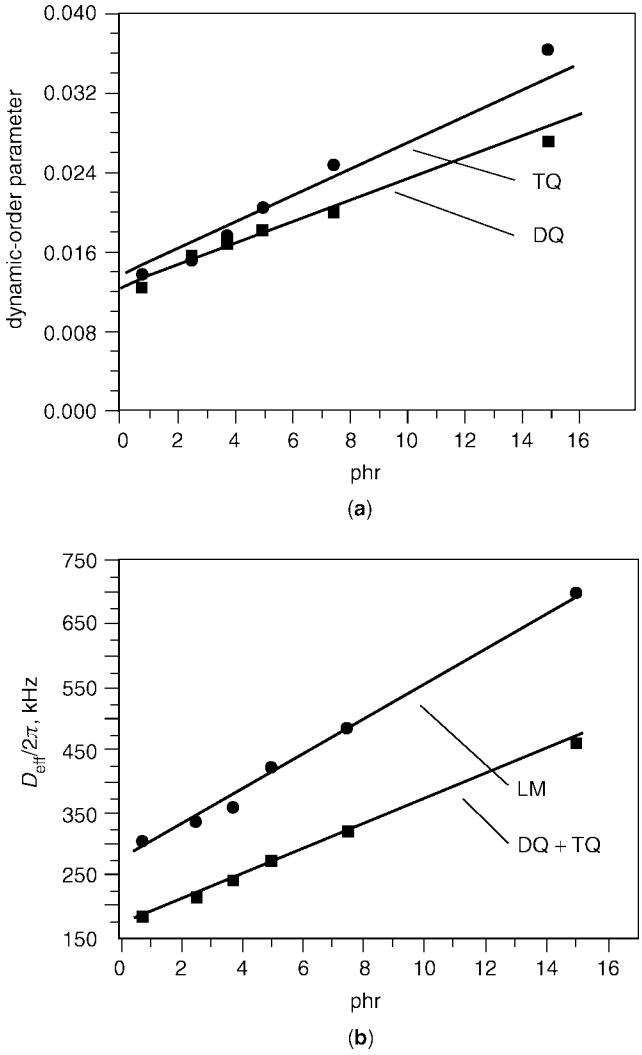

Fig. 11. (**a**) The dependence of dynamic-order parameters measured from DQ (squares) and TQ (circles) buildup curves on the cross-link density for synthetic polyisoprene. (**b**) The effective residual dipolar coupling D_{eff} (circles) measured from dipolar encoded longitudinal magnetization decays together with the D_{eff} values (squares) computed from dynamic-order parameters. A linear dependence on the cross-link density is evidenced in all cases (solid lines). Reproduced from Ref. 68, with permission from American Institute of Physics.

time scale is considered. It was shown that residual dipolar couplings measured in the initial time regime of the LM decays, DQ, and TQ buildup curves are more sensitive to cross-link density as compared to, for instance, transverse relaxation rates (68).

The proposed methods are generally applicable to partially averaged proton dipolar interactions and can be applied for studying segmental order and its associated dynamics in a variety of polymer networks or entangled melts and solutions

(transient networks) without the need for isotopic labeling, sample rotation, or the use of cross-polarization.

Heterogeneity in Segmental Chain Order of Grafted Polymers. Proton multiple-quantum NMR was also used for investigation of heterogeneity in segmental chain order of grafted polymers. The measurements were performed on a series of samples of poly(dimethylsiloxane) (PDMS) layers chemically attached to the surface of hydrophilic silica (76). These grafted PDMS layers consists of partially immobilized chain segments at the PDMS–silica interface and mobile chain portions outside the interface which is probed by measurements of homonuclear double- and triple-quantum buildup curves. These curves reveal a bimodal distribution of the residual dipolar couplings along the PDMS chain (see Fig. 12).

The segmental orientation detected in the interface and mobile regions are related to the average chain length and reflects the competing effects of the surface-induced orientation and chain conformations.

The ^{1}H DQ (and TQ) buildup curves were measured at two temperatures $T = 298$ K and $T = 227$ K for the three grafted PDMS samples with different chain lengths (N_t) and the results are shown in Figure 12. The buildup curves display two maxima. The first maximum shows a relatively sharply defined value of the excitation and reconversion time τ. The second maximum at longer τ values are more difficult to identify in sample PDMS3 ($N_t = 4.5$) and less pronounced in sample PDMS2 ($N_t = 6.2$) due to the small amount of the mobile fraction and the broadness of the signal. Nevertheless, the second maximum is enhanced at lower temperature (cf Fig. 12**b**) due to reduced mobility and therefore increasing residual dipolar coupling. The maximum at short τ values are due to the segments at the interface, and those present at longer τ correspond to the mobile fractions of the grafted PDMS chains. The first maximum occurs at the same τ value for the three samples indicating the same chain immobilization in the interface of all three samples. The immobilizations are caused by a loss of conformation entropy due to chain anchoring to the silica surface and by excluded volume effects from the silica surface and neighboring chains. Thus, the averaged residual dipolar couplings of the interface have the same values independent of N_t. These results are both reflected in the ^{1}H DQ as well as in the ^{1}H TQ buildup curves (76).

The positions of the second maximum of the three samples are also indicative of the anisotropy of chain motions outside the interface. Assuming the same thickness of the interface in all three samples, we deduce that the fraction of the mobile chain fragments decreases from sample PDMS1 ($N_t = 7.7$) to PDMS3 ($N_t = 4.5$). This results in a shorter τ value for the position of the second maximum for sample PDMS3 versus samples PDMS2 and PDMS1 that can be detected in the DQ as well as the TQ buildup curves (76).

A bimodal distribution of the segmental-chain orientation corresponding to the interface and the mobile regions of PDMS chains grafted onto silica was detected by ^{1}H multiple-quantum NMR spectroscopy. The size of the interface is found to be independent of the total length of the PDMS chains. A broad distribution of segmental orientation prevails in the mobile region, and the segmental mobility is proportional to its fraction and therefore to the chain length. At lower temperatures, the mobility decreases until at $T = 198$ K the whole chain appears to be immobile at the time scale of the NMR experiment of about 10^{-5} s.

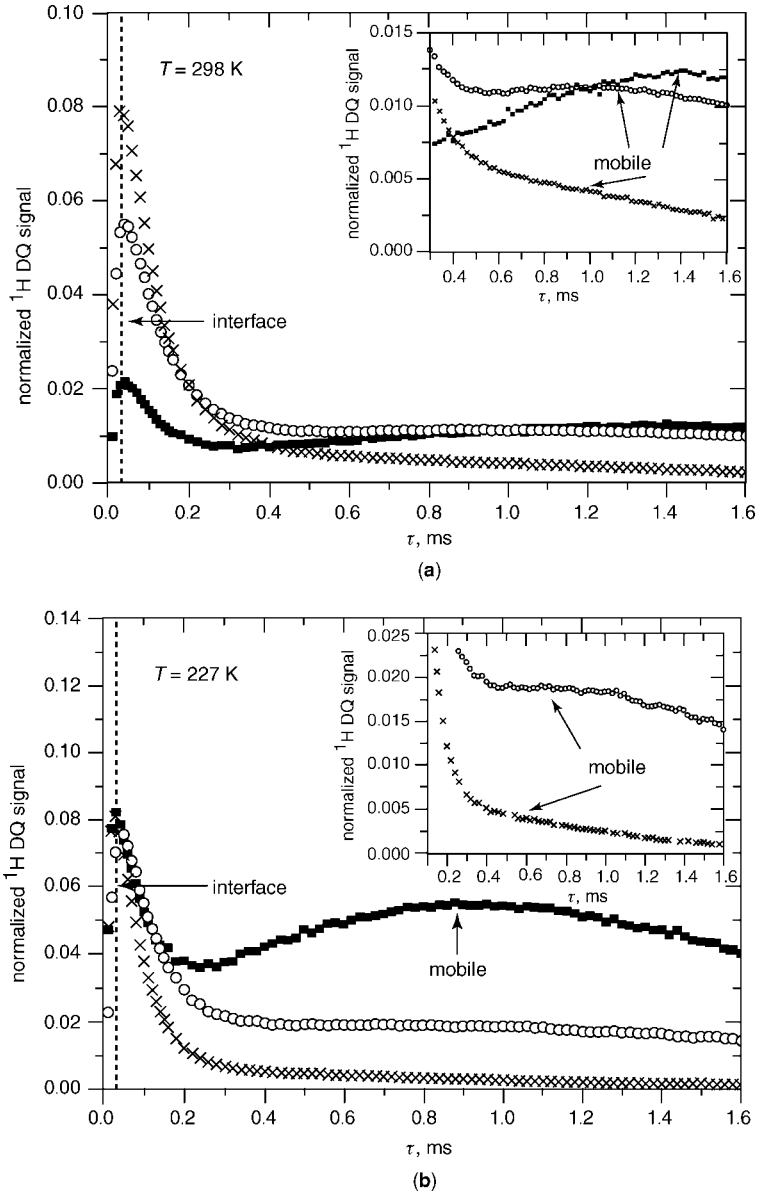

Fig. 12. Proton DQ buildup curves of grafted PDMS samples recorded at $T = 298$ K (**a**) and $T = 227$ K (**b**). (■) PDMS1, (○) PDMS2, and (×) PDMS3. The region of the DQ buildup curves after the first maximum is enlarged in the insets. Reproduced from Ref. 76, with permission from American Chemical Society.

The measurements using transverse ^{1}H relaxation shown that this quantity is also highly sensitive to the heterogeneous mobility of PDMS chains grafted onto a silica surface (77). This method allowed the distinction between a dense brush-like structure of the grafted layer containing chains of a fairly uniform

length and a layer containing a significant fraction of long-chain loops outside the grafted layer. The mobility of the chain outside the interface was found to increase with increasing average length of the grafted chains in agreement with the measurements performed by MQ NMR (76).

Local Segmental Anisotropy Induced by Mechanical Deformation. A well-known consequence of the theory of rubber elasticity is bond orientation (78,79). Deformation of an elastomer induces anisotropy of the backbone bonds of the polymer coil. In recent NMR studies of rubber elasticity, the mechanism of deformation and the orientation of network chains have received increasing attention (50,51). The local segmental anisotropy induced by a uniaxial applied force in elastomers was also investigated by NMR in terms of ^{1}H dipolar encoded longitudinal magnetization decays and double-quantum coherences buildup curves (80). These multipolar nuclear spin states were measured as a function of the angle θ between the static magnetic field and the direction of the applied force. The experimentally determined angular dependence of the effective residual dipolar couplings shows a minimum around the magic angle. These NMR methods offer the possibility to investigate in great detail the mechanisms responsible for the induced local anisotropy in strained polymer networks without contributions from the dipolar correlation effect (*vide infra*) and without need for chain deuteration.

Network Properties by Transverse Magnetization Relaxation. The transverse relaxation reflects mainly the loss of quantum phase coherence of spins. The axial symmetry induced by the presence of static magnetic field is of particular interest for observing the broad spectrum of relaxation rates related to the hierarchy of fluctuations, which affect any polymer chain in a melt or network (from about 10^9 s^{-1} down to less than 1 s^{-1}). For protons attached to polymer chains, the irreversible dynamics of the longitudinal magnetization is sensitive to properties generated by the local viscosity, which governs the random rotations of monomeric units. With regard to the transverse magnetization, the relaxation process cannot by analyzed without considering the time interval allotted for the full random rotations of chemical units that is close to the time interval (about 1 s or more) required for the full renewal of the chain configurations. However, this is to long a process for inducing any magnetic relaxation mechanism; consequently, the transverse magnetization is sensitive to a part of the hierarchy of chain fluctuations, only. In other words, random motions of units are detected as nonisotropic rotations generated by the topological constraints and the irreversible dynamics of the transverse magnetization is thus governed by the nonzero average of the dipolar interactions. A solid-like behavior of the transverse relaxation is expected to be associated with the property of elasticity, provided the time scale of the renewal of configurations is longer than the NMR scale of observation. This effect is considerably enhanced when permanent networks are observed.

Models for Transverse Relaxation. The simplest model to describe chain statistics from the NMR point of view is a chain of freely jointed segments of fixed length (12). Such a chain may be rescaled in several hierarchical steps according to the time scale of the motions which takes place at different space scales, compared to the time scale defined by the NMR spin interactions. All intrachain motions are assumed to be fast enough to average elementary interactions, whereas junction average positions are static.

Let us consider a linear chain of N statistical segments, fixed at its extremities. An average orientation is induced along the chain by these constrains. To estimate the effect of this average orientation on NMR parameters, the simplest picture is to consider that each segment carries an isolated pairs of spins, usually protons (two-spin approximation). Within this framework, the time evolution of the transverse magnetization $M_{\vec{R}}(t)$ for a spin pair attached to a chain may be written in the very simple form

$$M_{\vec{R}}(t) = \mathrm{Re}\left[M_0 \exp\left\{-\frac{t}{T_2}\right\} \exp\{\mathrm{i}\omega_{\vec{R}}\,\mathrm{t}\}\right] \tag{25}$$

where $M_{\vec{R}}(t)$ is the initial polarization, T_2 is the transverse relaxation time related to the fluctuating part of the dipolar Hamiltonian, and $\omega_{\vec{R}}$ is the residual dipolar interaction in angular frequency units. Other theories of transverse relaxation ((13), and references therein) are more complex that this simple approach. A polymer network is considerably disordered. To model this disorder, the end-to-end vector components $\vec{R}(x, y, z)$ may be supposed to obey ideal, the Gaussian statistics, ie,

$$P(\vec{R}) = \left(\frac{3}{2\pi N a^2}\right)^{3/2} \exp\left\{-\frac{3}{2}\frac{\vec{R}^2}{Na^2}\right\} \tag{26}$$

where a is the length of the statistical segment. The overall evolution of the complex transverse magnetization is then obtained by averaging equation 25 over end-to-end vector distribution. This yields (67)

$$M(t) = \mathrm{Re}\left[M_0\left(1 - \frac{2}{3}\mathrm{i}D_{ij}N_{\mathrm{e}}^{-1}t\right)^{-1/2}\left(1 + \frac{1}{3}\mathrm{i}D_{ij}N_e^{-1}t\right)^{-1}\exp\left\{-\frac{t}{T_2}\right\}\right] \tag{27}$$

where D_{ij} is the dipolar coupling constant for a spin pair and N_{e} is the effective number of statistical segments. At short times, ie, for $\Delta^2 N_{\mathrm{e}}{}^{-1}t^2 \ll 1$ the transverse relaxation decay has a Gaussian behavior corresponding to the presence of the residual dipolar couplings.

Experimental transverse relaxation decays cannot be usually described from exponential time functions but integral treatments of these curves yield standard parameters equivalent to relaxation rates (81). Without entering into too many details, it may be worth noting that the integral treatment amount to calculating several moments of the function $P(\vec{R})$. The first and the third moments of the distribution function are obtained from the two following integral treatments of the experimental relaxation curves

$$A_1 = \int_0^\infty \frac{M(t)}{\sqrt{t}}\,\mathrm{d}t, \text{ and } A_3 = \int_0^\infty \frac{\mathrm{d}M(t)/\mathrm{d}t}{\sqrt{t}}\,\mathrm{d}t \tag{28}$$

A NMR structural parameter χ_{c} was introduced which is defined as $\chi_{\mathrm{c}} = A_3/A_1$. The quantity $1/\chi_{\mathrm{c}}$ is proportional to the correlation length of segments between two consecutive nodes. Thermal behavior, swelling effects,

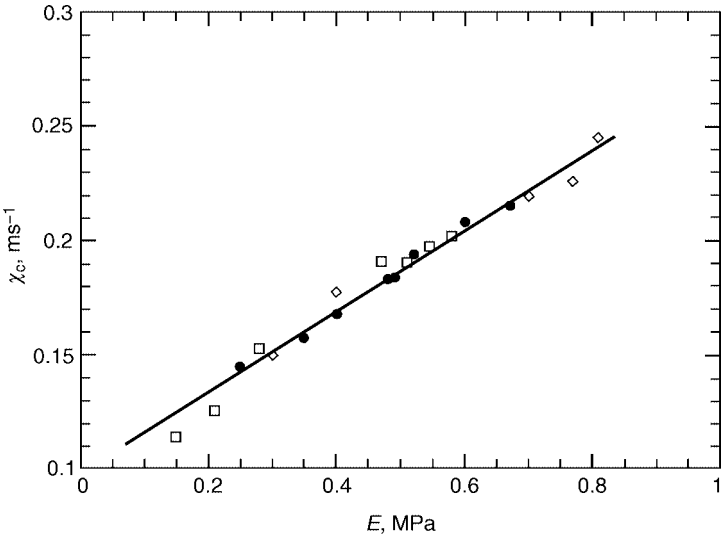

Fig. 13. Relaxation rate parameter χ_c as a function of the Young modulus E for randomly cross-link PDMS chains. NMR measurements were performed without any sample deformation. Reproduced from Ref. 82, with permission from American Chemical Society.

NMR-vulcanization, and NMR-elasticity relationships can be derived using the χ_c parameter ((81), and references therein). For instance, linear dependence of the NMR relaxation rate χ_c on the modulus of elasticity E measured on randomly PDMS chains (82) are shown in Figure 13.

Segmental fluctuations involved in the linear mechanical response to a small strain are directly observed from the transverse magnetization relaxation, in the absence of any strain.

Characterization of Polymer Networks by Transverse Relaxation. The NMR transverse magnetisation relaxation experiments were extensively used for quantitative analysis of the density of chemical cross-links, temporary and trapped chain entanglements and physical network junctions which are formed in filled rubbers, semicrystalline and ionic containing elastomers, and for determination of the molecular-scale heterogeneity of polymer networks ((83), and reference therein).

Several types of heterogeneity may occur in rubbery materials: (*1*) molecular-scale heterogeneity, which is caused by the chemical heterogeneity of uncured elastomers, network defects, and heterogeneous distribution of network junctions on a molecular level; (*2*) morphological heterogeneity of rubbery compounds due to a spatially heterogeneous distribution of components and filler in the compound; (*3*) spatial heterogeneity due to a difference in curing conditions such as temperature and concentration of vulcanisation agents throughout the sample volume.

A significant difference between the large spatial-scale mobility of network chains and that of network defects allows us to determine the degree of network heterogeneity. The most reliable data are obtained for swollen samples, because an increasing solvent content results in the disentanglement of network defects from network chains (84–86). The molecular mobility of network chains is consequently

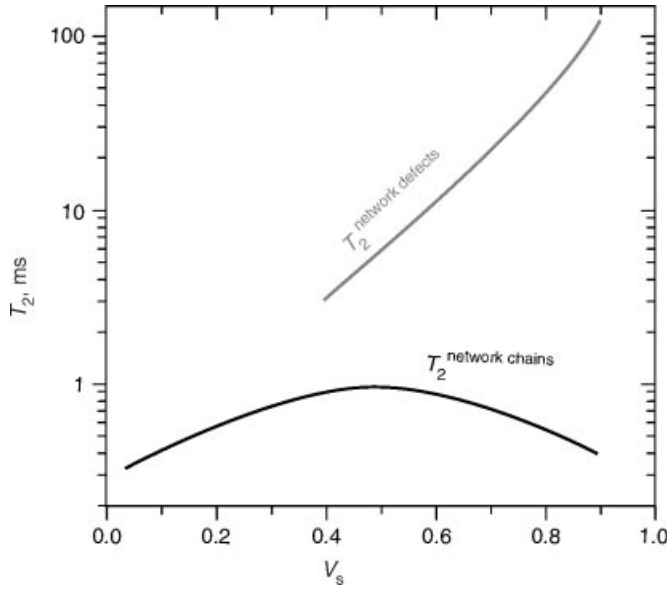

Fig. 14. The transverse relaxation time for a polymer network with defects against the volume fraction of a good solvent. Reproduced from Ref. 84, with permission from American Chemical Society.

decoupled from that of network defects, resulting in a major distinction in the relaxation behavior.

One example is given by the monoexponential T_2 decay of a cured acrylate that is splitted into two components upon swelling. This behavior is most clearly observable at high solvent concentrations (84,85). One component has short decay time (T_2^s), which is comparable with that of the original sample. This component apparently derives from network chains. Starting at a low volume solvent content (see Fig. 14), V_s, T_2^s shows an increase, which may be attributable to the following phenomena: (*1*) the disentanglement of network chains, (*2*) an increase in the frequency of the large spatial-scale chain motion, and (*3*) a slight decrease in the strength of the interchain proton dipole–dipole interactions. At $V_s \approx 40$–50 vol%, T_2^s reaches a maximum value. A value of T_2^s at the maximum, $(T_2^s)^{max}$, is related to the molecular mass of the network chains between chemical cross-links and trapped chain entanglements. At higher values of V_s, T_2^s decreases until the state of equilibrium swelling is reached. This decrease in T_2^s is thought to reflect the increase in the interchain proton dipole–dipole interactions as a result of the network chain elongation following a progressive increase in the solvent fraction in a swollen gel (12).

The long decay time (T_2^l) of the other component is typical of semidiluted polymer solutions. A T_2^l value continuously increases with an increasing solvent content. This component is apparently originated from the relaxation of network defects which are disentangled from network chains in a swollen state. At the equilibrium swelling degree, the relative fraction of the T_2^l relaxation component could be used as a measure of the fraction of highly mobile network defects. The

described behavior of T_2 relaxation decay following a progressive increase in the solvent fraction is typical of networks containing a significant fraction of network defects.

Distinct T_2 relaxation components with widely differing mean decay times suggest molecular or macroscopic heterogeneity of the material. In such cases, the submolecules concept can be used to describe the relaxation behavior (12). In a simplified interpretation, the overall T_2 relaxation decay of a heterogeneous elastomer is the weighted sum of the decays originating from the submolecules, which are defined as the network chains that are formed by the chemical and physical junctions, and network defects, ie, chains that are not attached to the network, chain loops and dangling chain ends. The large spatial-scale mobility of these submolecules differs substantially, and so does their relaxation behavior. The relative contribution of the submolecules to the overall decay is proportional to the number of protons attached to these chain fragments.

A quantitative analysis of the shape of the decay curve is not always straightforward due to the complex origin of the relaxation function itself (12,81,87–89) and the structural heterogeneity of the long-chain molecules. Nevertheless, several examples of the detection of structural heterogeneity by T_2 experiments have been published, for example the analysis of the gel/sol content in cured (90,91) and filled elastomers (85,86), the estimation of the fraction of chain-end blocks in linear and network elastomers (91,92), and the determination of a distribution function for the molecular mass of network chains in cross-linked elastomers (93,94).

Chain Orientation and Slow Dynamics by Dipolar Correlation Effect. An important 1D NMR method used for investigating anisotropy of chain dynamics and segmental order in polymer networks is given by the decay of the solid echo (12,63), a combination of Hahn and solid echoes (52), and a normalized stimulated echo (95–97). For all these cases, the echo amplitude decays can be described by a residual dipolar or quadrupolar correlation function (DCF) (for an introduction, see Reference 5). This function describes the autocorrelation of dipolar or quadrupolar randomly fluctuating interactions around the residual nuclear spin interactions that have been preaveraged by the fast dynamics of the chains and functional groups. Measurement of the DCF together with a corresponding theoretical model reveals important information about local segmental order and slow-chain dynamics under various experimental conditions. The possibility to measure the DCF using a combination of a solid echo, a Hahn echo and the free induction decay of protons, and deuterons has been discussed in Reference 63. An improved method was introduced later by Callaghan and Samulski (52) which exploits the fact that Hahn echo refocuses chemical shielding interactions and magnetic field inhomogeneities. Moreover, the Hahn echo amplitude is encoded by the molecular motions and residual dipolar couplings. The fluctuation of the dipolar interactions encodes the amplitude of the solid echo (actually a mixed echo) to a first approximation. The appropriate combination of these echoes, thus, gives access to residual dipolar couplings and the fluctuation rates. From the viewpoint of the spin system response, the solid echo completely refocuses the evolution of coherences of quadrupolar nuclei of spin $I = 1$ like ^{2}H and of a pair of 1/2 spins other than the ^{1}H multispin dipolar interactions. Therefore, the solid echo is strongly affected by the residual multispin interaction which makes the measurements of

DCF inaccurate. Moreover, the time scale of the dipolar or quadrupolar interaction fluctuations is limited to the time of the solid echo decay which is shorter than the transverse magnetization relaxation time. A considerably longer NMR time-window is offered by the DCF recorded with a stimulated echo (95–97). However, the amplitude of the stimulated echo is smaller than that of the solid echo and is affected by the multispin residual dipolar couplings as well as by the fluctuating dipolar fields. Furthermore, the evolution of the chemical shift Hamiltonian before storage of the z-magnetization encodes the stimulated echo evolution. Moreover, magnetization exchange competes with the dipolar correlation effect.

In all the cases discussed above, only the response of the spin system composed of dipolar coupled spin-1/2 pairs was considered. Proton DQ-NMR spectroscopy on elastomers—static and spinning at the magic angle—proved that the consideration of isolated spin-1/2 pairs is a crude approximation (68). The dipolar couplings between the protons belonging to various functional groups are shown to be active in two-dimensional DQ-MAS spectra for high excitation/reconversion times (68,73).

Dipolar correlation function can be measured for a multispin dipolar coupled network, for example, for the protons in functional groups attached to polymer chains in elastomers by a mixed echo given by the combination of the magic and the Hahn echo. The magic echo refocuses the residual multispin dipolar Hamiltonian with high efficiency (71–73,98). In a good approximation, the amplitude of the mixed echo is independent of residual (quasistatic) multispin couplings and inhomogeneous spin interactions including chemical shielding interaction. The following gives an evaluation of the dipolar correlation function describing slow chain motions within the limits of an exponential correlation function and a distribution of correlation times.

Mixed Echo Decay. The mixed echo amplitude decay can be expressed in terms of the autocorrelation function of the dipolar Hamiltonian (64). Transverse relaxation processes described by a single correlation time are rarely found in amorphous polymers including elastomers. If a normalized distribution of correlation times $g(\tau_c)$ is introduced, than the mixed echo decay is given by (64)

$$S_{ME}(6\tau) \cong 1 - \bar{M}_2 \int_0^\infty {\tau_c}^2 \left\{ e^{-\frac{6\tau}{\tau_c}} - 3\, e^{-\frac{5\tau}{\tau_c}} + \frac{9}{4}\, e^{-\frac{4\tau}{\tau_c}} + 3\, e^{-\frac{\tau}{\tau_c}} + \frac{3\tau}{\tau_c} - \frac{13}{4} \right\} g(\tau_c)\, d\tau_c \tag{29}$$

where τ_c is the correlation time. It is obvious form equation 29 that the measurement of DCF leads to a mixture of contributions from residual van Vlevk second moment and the distribution function of correlation times that is model dependent.

A particularly simple form for the function $g(\tau_c)$ is related to the log-Gaussian distribution (see for instance Reference 2), ie,

$$g(\tau_c) \equiv \frac{1}{\tau_c} F_G(\ln \tau_c) \tag{30}$$

where

$$F_{\mathrm{G}}(\ln\tau_c) \equiv \frac{1}{\sigma_{\ln}\sqrt{2\pi}} \exp\left\{ - \frac{[\ln(\tau_{\mathrm{c}}/\tau_{\mathrm{c0}})]}{2\sigma_{\ln}^2} \right\} \tag{31}$$

The center of gravity of the correlation time distribution is given by $\ln(\tau_{\mathrm{c0}})$ and the width of the distribution is $\Delta_{1/2} = 1.02\,\sigma_{\ln}$.

Parameters of the Dipolar Correlation Function for a Cross-Linked Elastomer Series. The mixed echo decays were measured for a series of cross-linked natural rubber (64). The model involving the distribution of correlation times (see eq. 29) was used to fit the mixed echo decay. The residual second van Vleck moments obtained from fits as a function of shear modulus G.

For ideal polymer coils, the most significant and distinctive property is the Gaussian distribution of the end-to-end distances. By considering the different segments of the freely jointed chain which are statistically independent and can be represented by a Markov chain, one can derive the correction to the Gaussian distribution of the end-to end distances (see Reference 99).

Using the corrected Gaussian distribution function one than gets (64)

$$\langle M_2 \rangle \propto \frac{5}{3}\frac{1}{N^2} - \frac{2}{3}\frac{1}{N^3} \tag{32}$$

Within the limit of the approximation used, it is concluded that the residual second van Vleck moment scales with $1/N^2$ for high numbers of statistical segments, ie, for $N \gg 1$, which means for low cross-link densities. However, this regime is invalid for the series of cross-linked natural rubber investigated using DCF (64). The effective number of statistical segments N is defined by the number of segments $N^{(0)}$ between physical cross-links or topological constraints and the number $N^{(\mathrm{C})}$ of segments between chemical cross-links. If we assume that the contributions to the residual dipolar coupling are additive and topological constraints are independent of the degree of chemical cross-linking, we can write $(N)^{-1} \approx (N^{(0)})^{-1} + (N^{(\mathrm{C})})^{-1}$. In this case, one expects (cf equation 32) that $\langle M_2 \rangle$ has a polynomial dependence on cross-link density or shear modulus.

Based on the dependence of the residual second moment on $1/N$ given by equation 32, the measured $\langle M_2 \rangle$ values can be fitted by a polynomial up to the forth power in the shear modulus G, ie,

$$\langle M_2 \rangle = a_0 - a_1 G + a_2 G^2 - a_3 G^3 + a_4 G^4 \tag{33}$$

This dependence is similar with that shown in Figure 8**a** measured using AIMS method (70). If only the first four values of $\langle M_2 \rangle$ corresponding to an intermediate regime of cross-linking are considered, the G^2 term dominates the dependence as it is expected from a Gaussian distribution of end-to-end vectors. The DCF measurements also reveal that the centre of gravity, as well as the logarithmic width of the distribution function of correlation time—which describes the slow motion of the network chains—scale with the cross-link density in a complex manner (64).

The development of NMR methods that allow accurate measurements of residual second van Vleck moments and the distribution of correlation times yields new tools to test polymer network theories that are more sophisticated than the theory of the freely jointed chain corresponding to a Markov chain.

Viscoelastic Polymers by Two-Dimensional NMR Spectroscopy

The investigation of molecular dynamics and local segmental orientation by two-dimensional (2D) NMR spectroscopy has a number of advantages (1,2) particularly when dealing with complicated spin systems such as viscoelastic polymers. Below, we will discuss examples of such investigations, concentrating on techniques that are particularly sensitive to the viscoelastic regime that is, NMR techniques for measuring residual dipolar couplings and dynamic order parameters. Readers interested in a more general overview of multidimensional NMR of polymers are referred to references (2,3,6).

Chain Orientation from 2D ^{1}H Magnetization Exchange Spectroscopy. Two-dimensional ^{1}H magnetization-exchange spectroscopy and its reduced one-dimensional (1D) variant have been used to probe residual dipole–dipole couplings between different functional groups of a SBR sample, namely between the CH and CH_2 groups of the butadiene units (65,100). The intergroup residual dipolar couplings can then be correlated with the shear modulus that is an independent measure of the cross-link density (65). Hence, the dynamic local-order parameter associated with the partially averaged dipolar coupling can be evaluated taking the average over the relevant dynamic processes.

Principle of the Method. Following the general scheme of 2D NMR spectroscopy, an evolution period of duration t_1 follows the excitation pulse. This interval ends with a flip-back pulse and the system is allowed to exchange during the mixing period t_m. After a third pulse the remaining signal is acquired during the detection interval t_2 (1). The intensity of the cross-peaks in the resulting 2D spectra then reflects the degree of exchange between the corresponding groups. Since full 2D NMR spectroscopy is time-consuming, for quantitative evaluations also a reduced 1D form has been used. In this case, the time t_1 is fixed and adjusted such that it acts as a chemical-shift filter (2) for one of the two butadiene lines in the static SBR spectrum. The reappearance of the filtered line with increasing mixing time is then a measure of the magnetization exchange between the protons of the CH and CH_2 groups. Note, that unlike the 500 MHz spectrum the styrene line and the CH line could not be distinguished in these experiments so that only the CH and CH_2 lines of the butadiene units are resolved. They are separated by about 3.35 ppm, corresponding to 1 kHz at the Larmor frequency of 300 MHz.

The theory needed for the evaluation of the exchange process was also developed (65,100). The model of the spin system used is depicted in Figure 15.

For short mixing times, the measurable exchange of ^{1}H longitudinal magnetization is predominantly determined by the protons belonging to nearest-neighbor CH and CH_2 groups. At longer mixing times on the other hand, a much larger spin system along the polymer chain must be considered, in principle. In Reference 100, however, it was shown that even in this case the intergroup residual dipolar

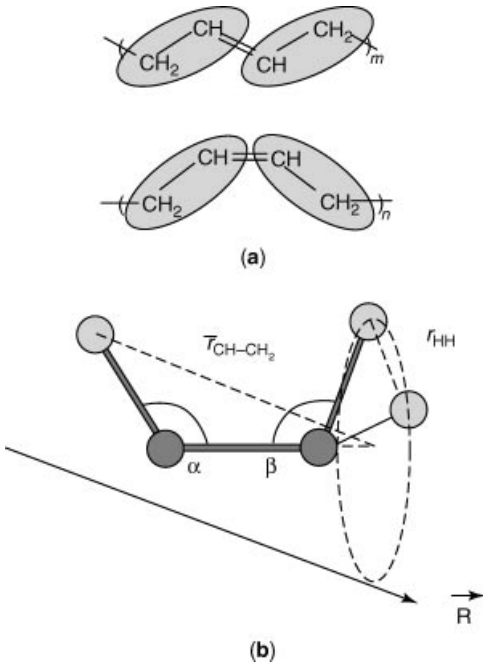

Fig. 15. (**a**) The monomer unit of *trans*- and *cis*-1,4-butadiene. The alternating sequence of CH—CH_2 groups, for which the magnetization-exchange process is treated. (**b**) The geometry of the CH—CH_2 spin system. The shaded circles represent protons and the black circles carbon atoms. The conformational jumps of the methylene protons lead to an average CH—CH_2 proton distance $\bar{r}_{CH—CH_2}$. Reproduced from Ref. 65, with permission from American Institute of Physics.

coupling can be measured from the initial-time regime of the magnetization-exchange decay curve.

In the limit of short mixing times t_m, the initial decay rates for the CH line were found (65,100) to depend only on the intergroup residual dipolar coupling $\bar{D}^{CH—CH_2}$ according to

$$\langle\langle I_z(t_m)\rangle\rangle = 1 - \frac{1}{2}\langle(\bar{D}^{CH—CH_2})^2\rangle t_m^2 \tag{34}$$

where $\langle\langle I_2(t_m)\rangle\rangle$ is the observable for the CH protons (for the CH_2 protons the factor 1/2 must be substituted by 1/4 in equation 34). The symbol $\langle\ \rangle$ represents the statistical ensemble average of the space part of the dipolar coupling in a disordered elastomer. Note, that from such measurements, the intergroup dipolar coupling $\bar{D}^{CH—CH_2}$ can be determined which is largely parallel to the segment axis. That is, it is much more informative with respect to the detection of chain order and chain motion than intragroup couplings would be.

Two-Dimensional ^1H Magnetization-Exchange Processes in Cross-Linked SBR. From the point of view of molecular motion, cross-linked elastomers are highly heterogeneous systems and a solid-like behavior is present together with slow and fast motions of both chains segments and functional

groups. Hence, the magnetization-exchange process is expected to be also heterogeneous, that is, driven by different mechanisms.

In order to investigate this heterogeneity, a series of static 2D NMR experiments was performed on SBR for increasing mixing time (100). As already discussed above, the aromatic and the olefinic protons are not resolved under the applied experimental conditions as can be seen in the 2D spectra shown in Figure 16.

A remarkable feature of the diagonal 2D spectrum for short mixing times is that the width of the diagonal peaks perpendicular to the (ω_1, ω_2) diagonal is much smaller than the widths along the diagonal. This indicates that the ^{1}H NMR spectrum is heterogeneously broadened (65). The width of each line along the diagonal reflects both the solid- and the liquid-like contributions, whereas the width perpendicular to the diagonal reflects selectively the liquid-like line width only. This feature is very pronounced for the CH diagonal peak and less for the CH_2 diagonal peak because of the strong proton–proton coupling within the methylene group. A similar result was already found in a ^{13}C magnetization-exchange experiment on natural rubber aimed to detect chain diffusion (101). While no chain diffusion was detected, the lines were also found to be spread out along the diagonal.

In the ^{1}H magnetization-exchange experiment on SBR not much cross-peak signal is found for mixing times shorter than 2.5 ms (see Fig. 16**a**). This indicates that within this time scale the CH and CH_2 functional groups can be considered in reasonable approximation to be isolated. The intergroup residual dipolar coupling leads to magnetization exchange for longer mixing times. Intense positive cross-peaks are thus present for $t_m = 30$ ms (see Figs. 16**d** and 16**e**). Such positive cross-peaks can arise for two reasons: from the exchange process mediated by residual dipolar couplings and from cross-relaxation induced by segmental motions with correlation times τ_c longer than ${\omega_0}^{-1}$ (1).

Proton Intergroup Residual Dipolar Couplings. The residual dipolar couplings between the protons of the CH and the CH_2 groups were determined from the t_m dependence of the peak intensities. The decay of the longitudinal magnetization $M(t_m)$ of the diagonal signals (normalized to the value M_0 that corresponds to zero mixing time) is recorded for short mixing times for the CH group. According to equation 34, the magnetization-exchange dynamics should show an initial quadratic dependence on t_m. This dependence is indeed found in the experiments and is shown in Figure 17**a** for SBR as an example.

From the slope of the initial magnetization decay, the values of the effective residual dipolar couplings $D_{\mathrm{eff}}^{\mathrm{CH{-}CH_2}} \equiv \langle (\bar{D}_{\mathrm{eff}}^{\mathrm{CH{-}CH_2}})^2 \rangle^{1/2}$ could be evaluated and it could be shown that these couplings scale with the cross-link density (65,100). The correlation of the coupling constant $D_{\mathrm{eff}}^{\mathrm{CH{-}CH_2}}$ with the shear modulus G as an independent measure of the cross-link density demonstrates this behavior (Fig. 17**b**). Note, however, that the line in Figure 17**b** does not cross the origin but provides a significant value for $D_{\mathrm{eff}}^{\mathrm{CH{-}CH_2}}$ at G = 0. This is not in contradiction with the applied model, but reflects the influence of local chain order (physical cross-links). From extrapolating to $G = 0$ in Figure 17**b**, the intergroup residual coupling of an uncross-linked SBR melt was determined to be $\bar{D}_{\mathrm{eff}}^{\mathrm{CH{-}CH_2}} \approx 533$ Hz. Using average internuclear distances and bond angles for SBR, one can extract the value for the dynamic-order parameter $S_{\mathrm{H{-}H_2}}$ of the CH—CH_2 intergroup linkage

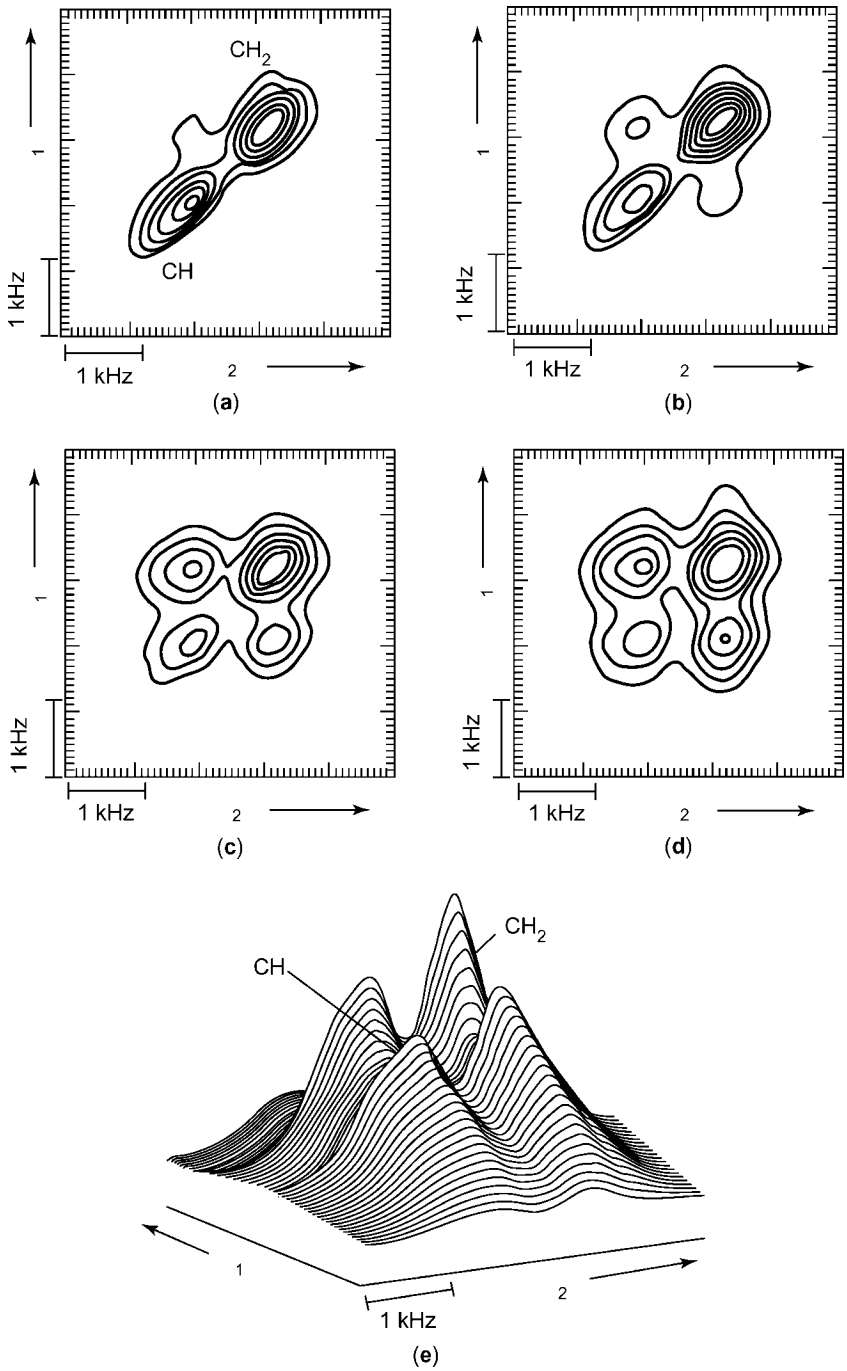

Fig. 16. Two-dimensional ^{1}H magnetization-exchange spectra of a SBR recorded with different mixing times have been used: $t_m = 2.5$ ms (**a**), 5 ms (**b**), 15 ms (**c**), and 30 ms (**d**). The 2D surface representation for $t_m = 30$ ms in (**e**) shows that all cross-peaks are positive. Reproduced from Ref. 65, with permission from American Institute of Physics.

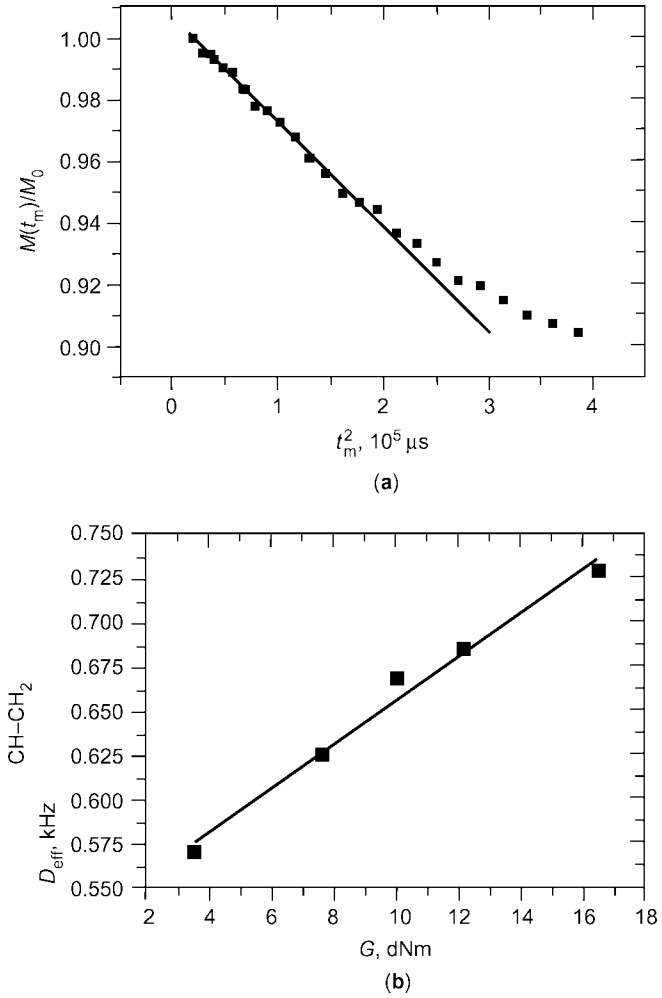

Fig. 17. (**a**) The initial decays of the proton magnetization for the exchange process CH → CH_2. The initial part of the magnetization-exchange data (starting with $t_m = 100\ \mu s$) shows the predicted dependence in t_m^2. The effective CH—CH_2 intergroup dipolar coupling constant $D_{eff}^{CH—CH_2}$ can be evaluated by fitting the theoretical curve. (**b**) $D_{eff}^{CH—CH_2}$ as a function of the shear modulus G for a series of differently cross-linked SBR samples. Reproduced from Ref. 65, with permission from American Institute of Physics.

$\vec{r}_{CH—CH_2}$ according to $\bar{D}_{eff}^{CH—CH_2} = D_{rigid}^{CH—CH_2} S_{H—H_2}$. This yields $S_{H—H_2} \approx 0.1$ and suggests an even higher value for the dynamic-order parameter for the corresponding carbon–carbon bond $S_{C—C} \approx 0.13$, since $\vec{r}_{CH—CH_2}$ and $\vec{r}_{C—C}$ forms an angle of 24°. Thus, even in polymer melts the chain motion can be largely anisotropic, as shown previously for poly(methacrylates) (102).

Magnetization-exchange NMR spectroscopy offers a convenient means for measuring the residual dipolar couplings between functional groups along the polymer chains. The intergroup dipolar coupling is remarkably high even in uncross-linked melts representing relatively high local segmental order. In

cross-linked samples, it scales with the cross-link density as predicted by the scale-invariant model of residual dipolar couplings (12), emphasing its relation to viscoelastic properties of the elastomers.

Segmental Motions by 2D NOESY-MAS Spectroscopy. In the previous paragraph, we have discussed the coherent magnetization-exchange process by ^{1}H non vanishing average dipolar couplings. Under fast MAS conditions, however, the residual couplings responsible for the exchange are largely refocused for full rotor periods and cross-relaxation by the fluctuating part of the dipolar interaction predominates. This so-called nuclear Overhauser effect (NOE) (103) takes place if the spins system is not in internal equilibrium. It corresponds to relaxation between dipolar-coupled nuclei such as ^{13}C and ^{1}H or between different nonequivalent magnetically sites of the same type of nucleus. NOE spectroscopy (NOESY) is well known in liquid-state NMR where it is one of the standard 2D techniques to elucidate and assign structures of macromolecules in solution (1).

Following the success of the technique in solution state, NOESY has been also applied to polymers or viscoelastic materials (104–110). As in solution experiments, one takes advantage of the fluctuating part of the dipolar coupling to extract useful structural and dynamical information. Using this method, nuclear Overhauser enhancement factors have been measured in polyisoprene over a range of temperatures with static ^{13}C NOE spectroscopy (104). A molecular-weight independent change of regime was observed at around 60°C for the backbone motion reflecting a loss of motional cooperativity with increasing temperature. Also the temperature-independent correlation time of the internal rotation of the methyl group could be inferred.

The polymer miscibility in polymer blends (PS/PVME) was probed by ^{13}C NOE spectroscopy under MAS (105). This study takes advantage of the fact that cross-peaks appear only between spins that are neighbors of each other, thus establishing NOE as a probe for the degree of mixture on the molecular level. Additional information on the molecular structure of the blend could be obtained from the NOE growth rates. The results suggest that there exists a specific interaction between the phenyl ring of the PS and the PVME methyl group. In Reference 106 the same technique was applied for investigating methyl groups as a source of cross-relaxation in solid polymers such as polycarbonate or polystyrene.

Static ^{1}H 2D NOE spectroscopy was applied in a first experiment showing that the technique can be used to measure interchain interactions (107). This work was then continued by applying the technique under MAS to investigate the intermolecular interactions responsible for the miscibility in polybutadiene/polyisoprene blends above the glass-transition temperature (108). It could be shown that intermolecular association can be probed by this technique and the results reveal the existence of weak intermolecular interactions between the polyisoprene methyl group and the vinyl side chain of the polybutadiene.

Segmental Motions of Elastomers. NOESY experiment under MAS on protons was used to study molecular motions in technical relevant materials such as rubbers (109,110). For the evaluation of these parameters, it is necessary to understand the cross-relaxation process in the presence of anisotropic motions and under sample spinning. Such a treatment is provided in Reference 110 and the cross-relaxation rates were found to weakly depend on fast motions in the Larmor frequency range and strongly on slow motions of the order of the spinning

frequency ν_R. Explicit expressions for the ν_R dependent cross-relaxation rates were derived for different motional models. Examples explicitly discussed were based on a heterogeneous distribution of correlation times (2,12,111) or on a multistep process in the most simple case assuming a bimodal distribution of correlation times (112–114).

The derived relationships were tested experimentally on a cross-linking series of styrene–butadiene rubbers and the cross-relaxation was studied as a function of the rotor frequency ν_R. As an illustration of such measurements, Figure 18**a** shows a surface representation of the gradient-selected 2D NOESY spectrum of a SBR sample acquired with a mixing time of 2.7 ms at a rotor frequency of 8 kHz. The lines corresponding to the aliphatic, the olefinic, and the aromatic protons are well resolved and can be assigned as indicated. Already at short mixing times pronounced cross-peaks are visible, in particular between the olefinic CH and the CH_2 group.

Figure 18**b** shows the decay curve of the diagonal peaks for mixing times up to 3 ms. Unlike in the magnetization-exchange case (65), the decay is found to be approximately linear in t_m in the short mixing time regime and exponential or biexponential for long times (110). A similar curve can be plotted for the increase of the cross-peaks. In order to investigate the effect of the sample spinning on the cross-relaxation rates, series of 2D NOESY-MAS spectra were acquired as a function of the rotor frequency. The rates evaluated from these series were found to decrease linearly with rotor frequency that is an indication that cross-relaxation in elastomers is dominated by slow motions in the 10 kHz regime rather than by motions in the Larmor frequency range as in case of liquids. The cross-relaxation rates at room temperature were found to depend moderately only on the cross-link density that is another indication that cross-relaxation is dominated by the α process.

The experimental rates were analyzed in terms of the explicit expressions derived by the theoretical treatment (110). As expected for a statistical copolymer, segmental motions in the SBR samples cannot be described by a single correlation time (2). From T_1 data that were also measured the correlation time should be in the range of 10^{-8} s while the rotor frequency ν_R dependence of the cross-relaxation rates requires a correlation time of 10^{-5} s. So it is clear that at least two different correlation times are necessary to account for the experimental findings. The relaxation dispersion data T_1 (ω) (ω being the Larmor frequency) (96), however, show no discontinuity that would indicate the presence of two distinct motional processes. Thus, the data were analyzed in terms of a broad distribution of correlation times for almost isotropic segmental motions (α relaxation). With a simple log-Gaussian distribution function of reasonable parameters (110) it was found that one could account for both the T_1 values and the ν_R-dependent cross-relaxation rates. From the center of gravity of the distribution, the glass-transition temperature could be estimated as $T_g = 230$ K using the well-known Williams–Landel–Ferry (WLF) equation (2). This value compares favorably with the known value of $T_g = 220$ K for uncross-linked SBR-1500.

Selective Residual Dipolar Couplings by ^{1}H Multiple-Quantum NMR Spectroscopy. Multiple-quantum MQ NMR spectroscopy is well established for structural studies of liquids and highly mobile solutes in liquid crystals (1,26).

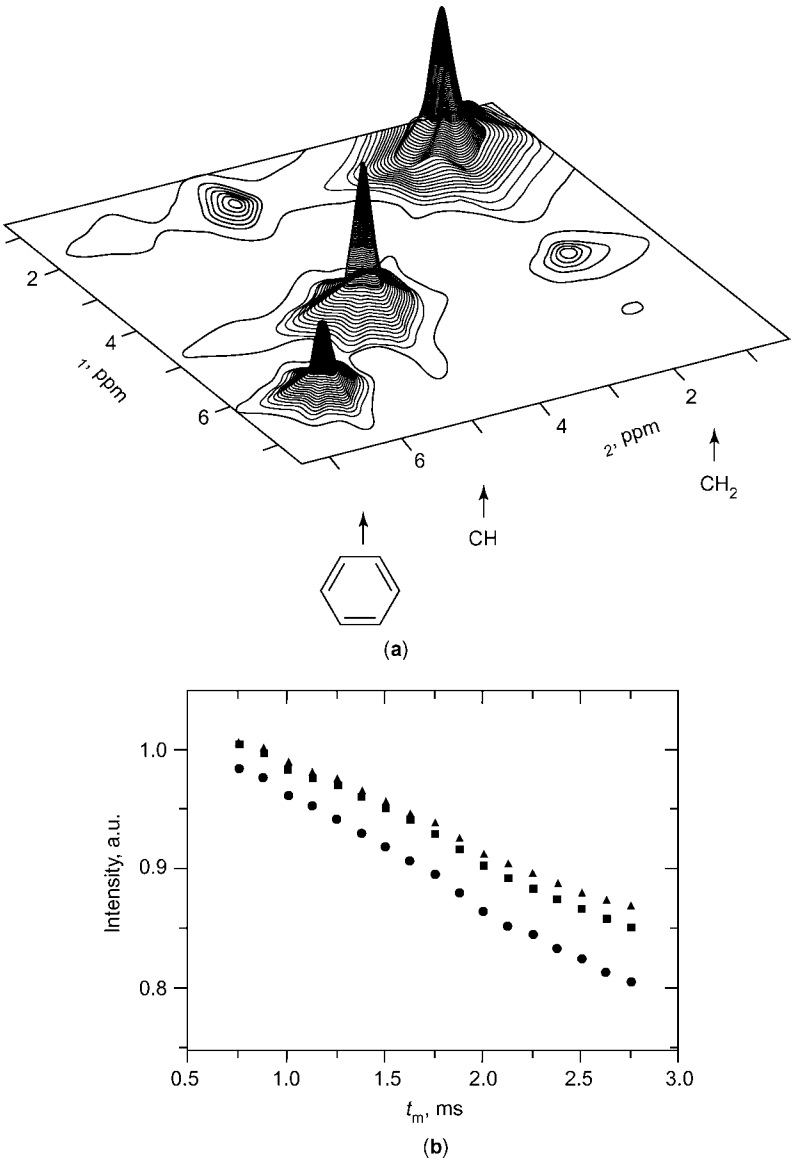

Fig. 18. (**a**) 2D ^{1}H-NOESY surface spectrum of SBR acquired for a mixing time of 2.7 ms and under 8 kHz MAS. Already at this short mixing time pronounced cross-peaks are visible. (**b**) Short-time decay of the cross-peak intensity evaluated from a series of 2D spectra. Such curves can be analyzed providing information on internuclear distances and segmental dynamics (■) aromatic CH, (●) olefinic CH, (▲) CH. Reproduced from Ref. 110, with permission from Taylor & Francis Ltd.

In recent years, there has been a sustained effort to obtain homonuclear (73,115–119) and heteronuclear (120–122) high resolution MQ NMR spectra also for organic solids using fast MAS to increase resolution and sensitivity. Such MQ spectra proved to be valuable tools for determining dipolar connectivities between

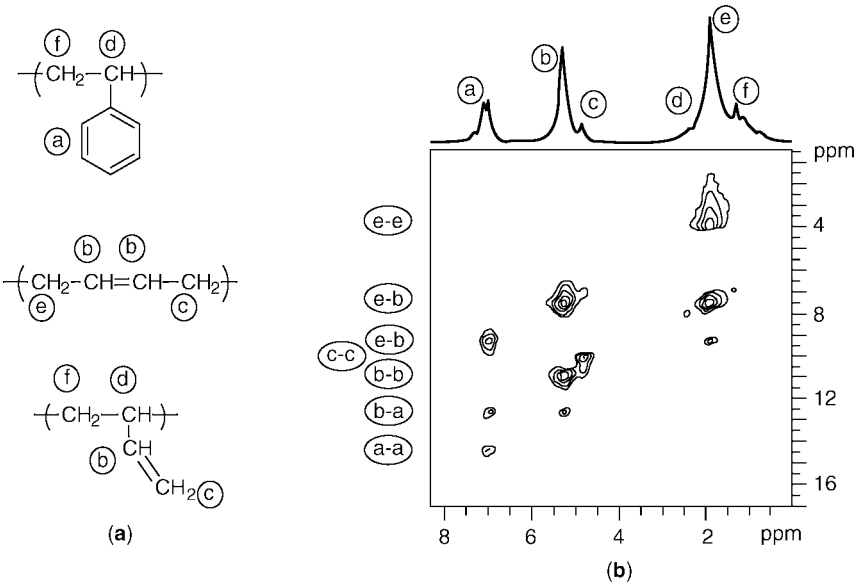

Fig. 19. Proton DQ MAS spectrum of a SBR sample with a low value of cross-link density (0.8–0.8 phr sulfur accelerator). The rotor frequency was 10 kHz and the t_1 increment was 15 μs. The diagonal peaks and the cross-peaks of the functional groups are assigned as indicated (compare (**a**) and (**b**)). Reproduced from Ref. 73, with permission Elsevier.

spin-1/2 nuclei (74,75,116). More quantitatively, dipolar couplings, internuclear distances, and molecular torsion angles can be measured by these techniques (74). For viscoelastic materials, it was recently shown that ^{1}H high resolution MQ NMR spectroscopy offers the possibility to measure site-selective residual dipolar couplings between all resolved protons (73,119). The MQ technique thus is an attractive tool for studying structure and dynamics in polymer melts (119) and elastomers (68,73).

Dipolar Connectivities from the High Resolution ^{1}H DQ MAS Spectroscopy. Figure 19 shows the ^{1}H DQ spectrum of a cross-linked SBR sample that has been acquired at a spinning frequency of 10 kHz (73).

The peaks in the 2D DQ spectrum correspond to double-quantum coherences between two spins which must be relatively close neighbors in space in order to contribute significantly to the peak intensity as follows from the strong distance sensitivity of the dipolar coupling. From the existence of the corresponding peaks therefore through space dipolar connectivities can be easily established.

The assignment of the peaks is shown along the ω_1 dimension by pairs of letters a–f (see Fig. 19**a**) which indicates the functional groups that are involved in the generation of the corresponding DQ peaks. From a simple qualitative inspection of the DQ spectrum, it can be seen that there are dipolar connectivities between practically all functional groups. The strongest DQ signals are found between protons of the polybutadiene groups, but also DQ peaks of considerable intensity are visible between the polybutadiene protons and the aromatic protons of the styrene units. This indicates a good mixture of the different functional

groups on the nanometer length scale as is found for instance in the case of a statistical copolymer.

Another recent example of the use of ^{1}H DQ MAS NMR spectroscopy is given by the study of molecular scale miscibility of poly(butylenes terephtalate)-*block*-poly(tetramethylene oxide) multiblock (PBT-*block*-PTMO) copolymers (123) by looking for correlation peaks between signals from the hard and soft blocks.

Previous ^{13}C NMR MAS relaxation experiments revealed a large, bimodal-like heterogeneity of the PTMO chain mobility, which were explained by microphase separation of the amorphous phase into a highly mobile PTMO-rich phase and a less mobile PBT/PTMO mixed phase (PBT/PTMO interface) (124). However, the motional heterogeneity of the PTMO blocks can also originate from a dynamical interface due to anchoring of PTMO blocks to rigid PBT domains, which can cause apparent "two-phase" behavior. 2D NMR experiments can provide direct information on the molecular scale miscibility in polymeric materials. ^{1}H DQ correlation spectroscopy under fast MAS using the back-to-back (BABA) sequence is used in the present study to determine the proximity of the PBT and PTMO chain units in the block copolymers.

The ^{1}H MAS NMR spectrum of PBT-*block*-PTMO consists of resonances at 8.0, 4.4, 3.4, and 1.6 ppm that originate from the aromatic protons of PBT, OCH_2 protons of PBT, OCH_2 protons of PTMO, and the $(CH_2)_2$ protons of PBT and PTMO, respectively. It is noted that the OCH_2 protons of PBT and PTMO at the transition from PBT to PTMO blocks along the chain have slightly different chemical shifts, as measured by ^{1}H solution NMR spectra, ie, 4.35 and 3.45 ppm for PBT and PTMO, respectively. However, these resonances are not resolved in the solid state NMR spectra. Figure 20 shows the phase-sensitive 2D spectrum of sample A1000/35 measured using the BABA sequence (123). The single-quantum (SQ) and double-quantum (DQ) dimensions are shown on the horizontal and vertical axes, respectively. The signals in the DQ dimension are situated at the sum of the frequencies of the two-coupled protons. Therefore, a DQ signal between two protons with identical chemical shifts will be on the diagonal, and signals between two protons with different chemical shifts will be off-diagonal giving rise to two signals equally spaced from the diagonal. One should note the different positions of off-diagonal signals are compared to COSY/NOESY spectra.

As expected, all resonances of PBT and PTMO blocks are present in the 2D spectrum, ie, all diagonal peaks and off-diagonal correlation peaks between the aromatic and the OCH_2 protons of PBT as well as a correlation peak between the CH_2 and OCH_2 peaks of PTMO. Additionally, there is a correlation peak between the aromatic protons from PBT and the OCH_2 groups from PTMO, suggesting a close proximity of these two chain fragments. The signal is in fact much more intense than one would expect (*1*) from a small fraction (only 14%) of PTMO chain units that are located at the transition from PBT to PTMO blocks in a single chain and (*2*) from the rather long intrachain distance between aromatic PBT and the OCH_2 protons of PTMO at the transition from the hard to the soft blocks along the chain. The correlation peak cannot be explained by spin diffusion during the 1ms *z*-magnetization delay after the reconversion period. Therefore, the DQ BABA MAS experiment is not affected essentially by the spin diffusion process and gives information about the molecular scale mixing. This correlation peak has to come primarily from intermolecular couplings between the PBT and PTMO protons

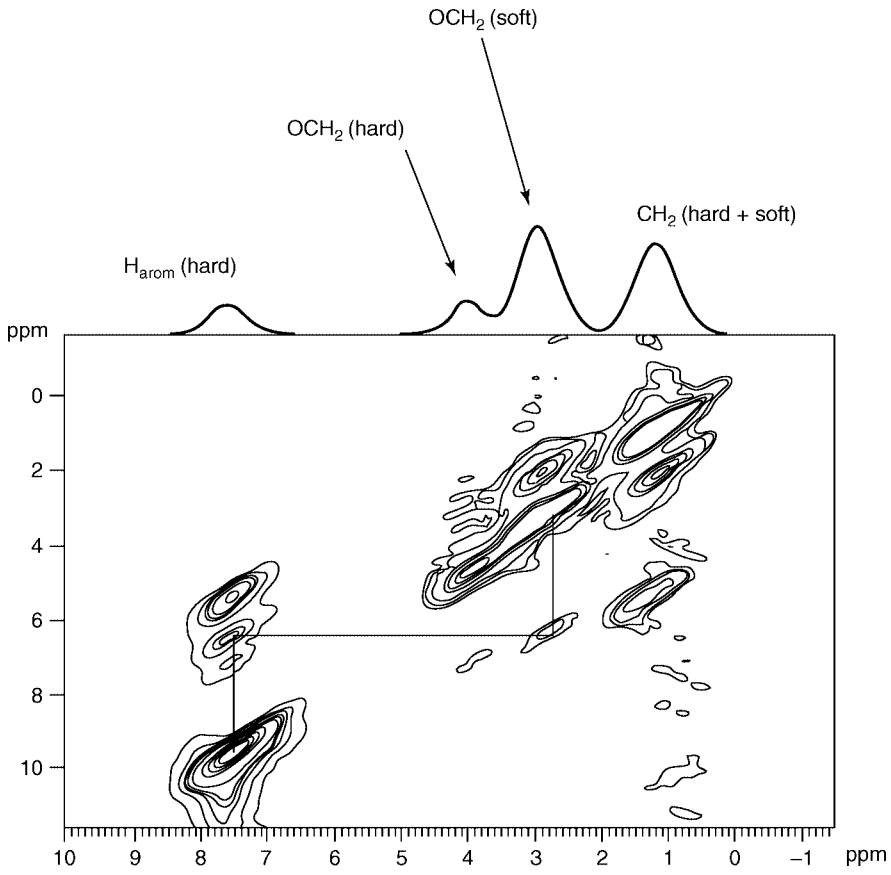

Fig. 20. Two-dimensional ^{1}H DQ MAS spectrum for thermoplastic elastomers PBT-*block*-PTMO with a length of PTMO block of 1000 g/mol and amount of PTMO block of 35% in weight (sample A1000/35) showing the dipolar correlation between the resonances of PBT and PTMO chain units, as indicated by the lines connecting the peak positions. Reproduced from Ref. 123, with permission from American Chemical Society.

of adjacent chains. In fact, it was shown that a DQ correlation signal arises at short recoupling times, which in our case, marks an interproton distance below 0.5 nm. Therefore, this correlation peak can be unambiguously attributed to PBT and PTMO units in a mixed PBT/PTMO phase.

Site-Selective Double-Quantum Buildup Curves and Correlation with Cross-Link Density. A more quantitative evaluation of the DQ peak intensities is possible by acquiring the experimental DQ buildup curves for each of the peaks performing a series of DQ experiments with increasing excitation time. As an example, the buildup curves for the three main contributions are shown in Figure 21 for two SBR samples with different cross-link densities (73).

A fit of the experimental DQ builtup curves using a relationship derived in the spin-pair approximation allows the ratio of the corresponding residual dipolar couplings to be determined, ie, $(\bar{D}^{CH_2} S_s^{CH_2}) : (\bar{D}^{CH_2-CH} S_s^{CH_2-CH}) : (\bar{D}^{CH-CH} S_s^{CH-CH})$, where $\bar{D}^{ij}$ represents a preaveraged dipolar coupling constant and S_s^{ij} the

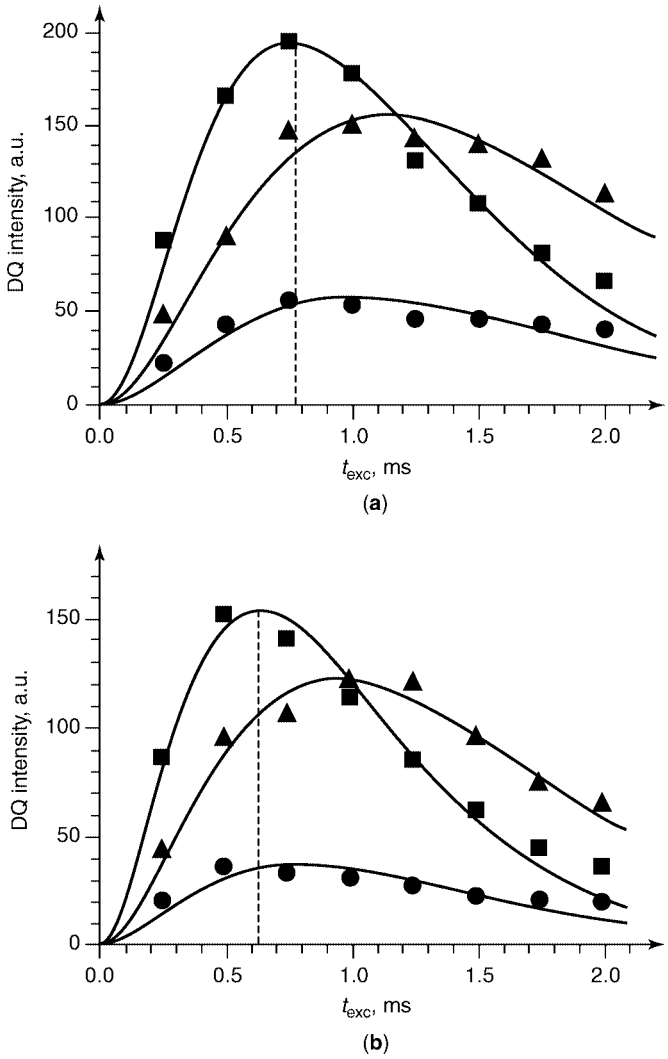

Fig. 21. Site-selective ^{1}H DQ buildup curves for low (**a**) and high (**b**) cross-linked SBR samples. The DQ signals correspond to the —CH_2— (■), CH_2—CH— (▲) and CH═CH coherences (●). The vertical dashed lines mark the excitation times for the maximum signal for the methylene protons, which differs for the two cases. Reproduced from Ref. 123, with permission from Elsevier.

corresponding scaled dynamic-order parameter (73,119). The order parameter $S_s^{CH_2—CH}$ (calibrated using a 1D MAS sideband pattern) is found to be close to the value $S_s^{CH_2—CH} = 0.1$ that has been estimated for SBR samples by the magnetization-exchange experiments described above (65). The order parameter corresponding to the CH—CH coupling is even higher (73). This coupling provides the best measure for the chain dynamics since it is predominantly aligned along the segmental axis.

For investigating a series of samples with different cross-link densities, however, the procedure described above is very time-consuming. In this case, a somewhat less detailed 1D measurement of the integral DQ-filtered signal can be used to establish the relationship between the total DQ intensity and the cross-link density. The square root of the DQ intensity is found to be an approximately linear function of the cross-link density but, more important, the topological constraints that are already present in the melt are found to dominate the residual couplings (see also Reference 119). Hence, the technique is not so much a sensitive measure of the cross-link density but is a rather sensitive and selective probe for local dynamic chain order.

The strongest residual dipolar couplings were also edited in a nonrotating cross-linked polyisoprene series by exciting double- and triple-quantum coherences in the short time regime (68). From this, the dynamic order parameters of the methylene and methyl groups were estimated and correlated with the cross-link density. Essentially, the same behavior was found as for SBR.

Residual Local Dipolar Fields by Heteronuclear Correlation Experiments. The NMR spectrum of rare spins (e.g. ^{13}C) contains extremely useful information because of the usually high chemical-shift dispersion and the possibility to easily eliminate undesired spin interactions. It would thus be advantageous to combine this high resolution dimension with ^{1}H spectroscopy in form of a heteronuclear correlation experiment (1). In the following, we will concentrate on the so-called wide-line separation (WISE) experiment (2,125–128), in which ^{1}H broadline information is correlated with the ^{13}C spectroscopic information. There are however also other possibilities for including heteronuclear information in a 2D experiment, for instance, 2D heteronuclear *J*-resolved spectroscopy which was applied for the investigation of filled natural rubber in Reference 101. It was concluded that there must be a high degree of motion in order to allow the scalar ^{13}C—^{1}H couplings to be revealed by magic-angle spinning alone. The ^{13}C line width was found to be determined by susceptibility effects due to the presence of the filler.

While the (heteronuclear and homonuclear) residual dipolar couplings have to be eliminated in such *J*-resolved experiments, they are the main source of information in the WISE experiment described below. For the investigation of viscoelastic materials the experiment thus must be performed under static conditions or under slow magic-angle spinning. The method is discussed in the previous section.

^{13}C–^{1}H Local Residual Dipolar Couplings by WISE-MAS Experiments. For elastomers and rubbery-like materials well above the glass-transition temperature T_g, the high molecular mobility reduces the dipolar couplings dramatically. The WISE experiment allows one to investigate site-selectively residual dipolar interactions and thus molecular dynamics by editing the corresponding proton slices of the 2D data set.

In References 129 and 130 ^{13}C-edited ^{1}H transverse relaxation was investigated in a nonrotating SBR cross-linking series. A short contact time was used to avoid ^{1}H spin diffusion. As a consequence of this, only ^{1}H atoms directly bonded to ^{13}C atoms are observed and the ^{1}H transverse relaxation is thus found to be mainly governed by ^{1}H—^{13}C heteronuclear couplings which makes analysis simple. The ^{13}C-edited ^{1}H transverse relaxation could be fitted with only one adjustable

parameter, the effective number of statistical segments (129). This was invoked as a justification for the heterogeneous model used to describe transverse relaxation. Moreover, the effect of cross-linking could be investigated and it was shown that it affects the dynamics of all functional groups to the same extend (125).

A similar experiment has been performed in (125) but under MAS conditions. For a series of cross-linked natural rubber samples (A-F1), ^{13}C-edited ^{1}H spinning sidebands have been extracted from the 2D spectrum. These sideband patterns are encoded by the residual dipolar couplings of the corresponding functional groups and are presented in Figure 22.

For the experimental conditions given, the spectra are found to be dominated by heteronuclear dipolar interactions which leads to relatively narrow, well-separated dipolar spinning sidebands. The heteronuclear dipolar couplings could be evaluated by simulating the spectra on this basis (see right column in Figure 22). They where found to be between 0.9 and 1.5 kHz for the samples of the series (the intercross-link masses M_c were between 6700 and 11,000 g/mol). A practically identical envelope of the spinning-sidebands intensities in the indirect dimension is found for all functional groups. This indicates that the effective ^{1}H—^{13}C vectors of different segments are affected in approximately the same way by internal motions.

Spin diffusion as an alternative explanation of this effect could be excluded by a similar experiment with additional ^{13}C decoupling during the evolution period t_1 which eliminates the encoding by the heteronuclear dipolar couplings (125). Distinct features are then visible for the spinning sideband patterns of the CH_3, CH_2 and CH groups (see Reference 125) proving that different functional groups are relatively isolated from each other on the time scale of the experiment as a consequence of the reduction of homonuclear dipolar interactions by high segmental mobility and magic-angle sample spinning. Therefore, the indirect detection of the spinning sideband patterns via cross-polarization ^{13}C spectroscopy allows for selective measurements of residual dipolar interactions on different functional groups (125).

Deuterium NMR Studies on Thermoplastic Elastomers. For the investigation of the molecular dynamics in polymers, deuteron solid-state nuclear magnetic resonance (^{2}D-NMR) spectroscopy has been shown to be a powerful method (2). In the field of viscoelastic polymers, segmental dynamics of poly(urethanes) has been studied intensively by ^{2}D-NMR (131,132). In addition to 1D NMR Spectoscopy, 2D NMR exchange spectroscopy was used to extend the time scale of molecular dynamics up to the order of milliseconds or even seconds. In combination with line-shape simulation, this technique allows one to obtain correlation times and correlation-time distributions of the molecular mobility as well as detailed information about the geometry of the motional process (2).

Principles of the Method. The scheme typically used for such 2D-exchange NMR experiments corresponds to that given in References 1 and 2, however, in case of deuterons often a solid echo sequence is used for detection instead of the last pulse. During the mixing time t_m of the experiment, molecular reorientations are allowed to take place. If the molecular orientation of a C—^{2}H bond has changed due to slow molecular motions, the signal continues to evolve with a new frequency. For reorientation about a well-defined angle θ, the 2D exchange spectrum exhibits

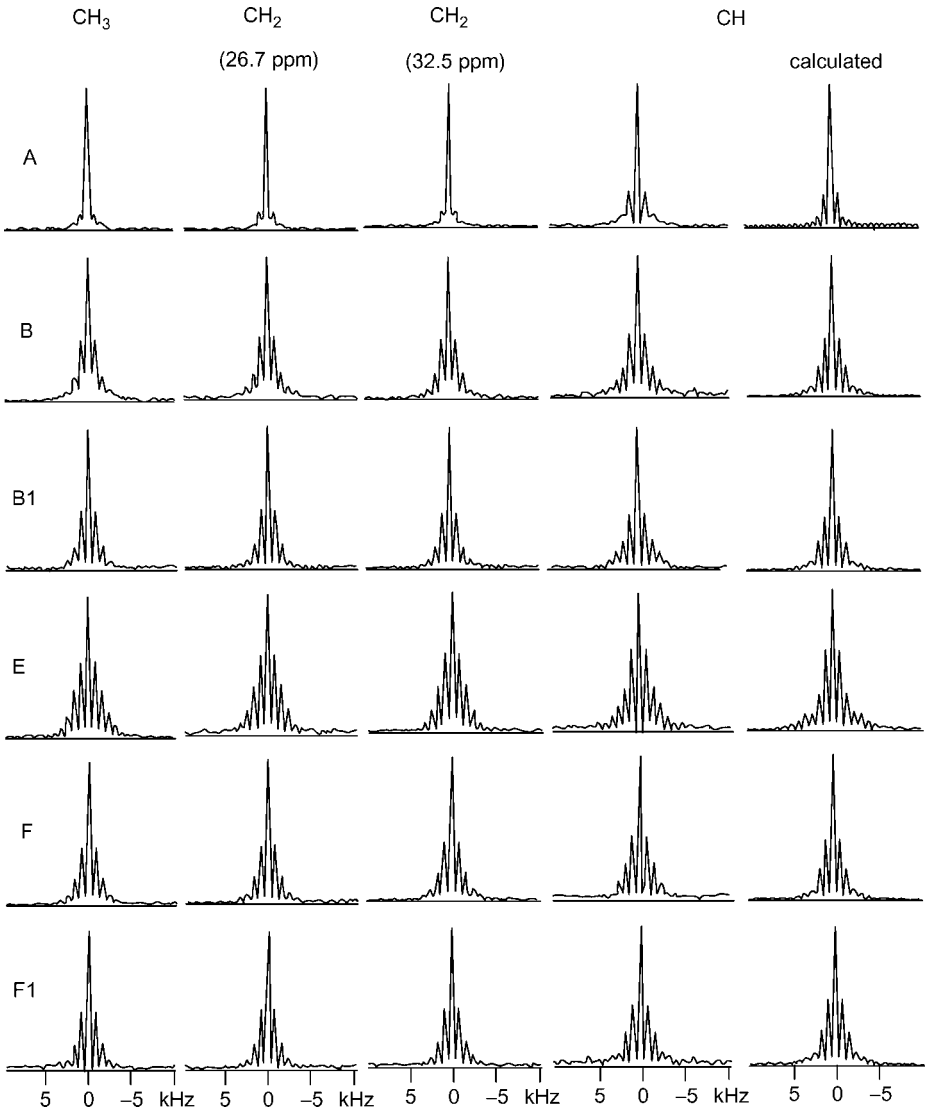

Fig. 22. Slices from a 2D experiment corresponding to $^{13}C—^{1}H$ WISE experiment performed on a series of cross-linked natural rubber samples A—F1 under magic-angle spinning. The slices reflecting proton sideband pattern for the different functional groups that are encoded by the ^{1}H residual dipolar couplings. The distinct features of dipolar slices prove that the different functional groups may be considered as relatively isolated groups of spins on the time scale of the evolution and cross-polarization. Reproduced from Ref. 125, with permission from Rapra Technology.

characteristic ridges in the form of ellipses that can be analyzed with respect to motions (for details about the analysis we refer to literature (2)).

Local Motions and Segmental Orientation in Supramolecular Hydrogen Bond Assemblies. In the field of viscoelastic materials, the technique has been mainly applied to thermoplastic elastomers. One interesting elastomer belonging

to this class consists of polybutadiene chains functionalised by 4-(3,5-dioxo-1,2,4-triazolidin-4-yl) benzoic acid (U4A) units which act as effective junctions zones. The molecular dynamics of the phenyl rings of the U4A units has been probed by 1D and 2D ^{2}H-NMR (see Reference 133, and references therein). In this system, there are three spatially separated environments that are reflected in the mobility of the polar units. Phenyl rings which are incorporated in the structure are either rigid or undergo 180° phenyl flips. The small fraction of free functional groups move isotropically and their mobility is coupled to the dynamics of the polymer matrix. The 1D ^{2}H-NMR spectra can be described quantitatively assuming a distribution of correlation times over 2–3 decades and the geometry of the motional processes is defined by the environment in the clusters up to the order–disorder transition temperature. 2D spectra of the model compounds show an elliptical exchange patterns, indicating well-defined slow 180° phenyl flips on a time scale of 100 ms up to 3 s.

Principles of NMR Imaging Methods

In polymers, the spatial distribution of the nuclei and the spin interactions as well as motions can be probed by NMR at different length scales using different strategies. The NMR techniques suitable for investigation of spatial structures are identified in Figure 23 together with the appropriate spatial resolution scale. In the nanoscale range, spectroscopic methods based on manipulation of spin interactions can measure internuclear distances and bond angles ((27), and references therein).

The field gradients are used for selection of the coherence pathways and encoding of molecular diffusion but many methods perform without the demand for field gradients. In the mesoscopic range, spin diffusion ((2), and references therein) can be used for measuring domain sizes and morphology. The domain of NMR imaging of polymers (134–138), which uses space encoding by field gradients can probe today only the macroscopically distributed heterogeneities, ie, in the order of 10–100 μm.

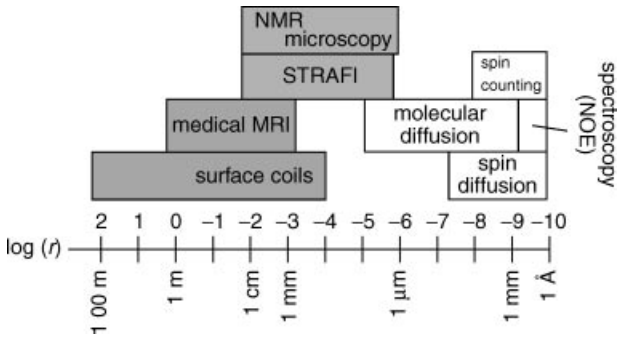

Fig. 23. Range of spatial resolution available from different NMR experiments that covers over teen orders of magnitude. The methods using direct space encoding by gradient are shaded, but all other spatial information can be included for creation of image contrast. Reproduced from Ref. 136, with permission from Wiley.

In recent years, the field of spatially resolved magnetic resonance which includes imaging, microscopy, and volume localized spectroscopy of materials (5,18) has been advanced by the introduction of several new techniques and improvement of the existing ones designed to overcome, mainly, the dipolar interactions of abundant proton spins in rigid polymers that contribute to broadening of the NMR resonance lines. The well-known condition $\Delta x = 2\pi\,\Delta\nu_{1/2}/(\gamma G_x)$ (see for instance, Reference 47) for the spatial resolution Δx^{-1} by frequency encoding, where γ is the magnetogiric ratio, $\Delta\nu_{1/2}$ is the full width at half height of NMR spectrum and G_x is the field gradient strength in the x-direction, can define the strategies for improving the quality of NMR images. There are, in principle, two possibilities: either the gradient strength can be increased or the line width be reduced (47,139–141). This can be achieved by manipulation of the spin or the space part of the interaction Hamiltonian or both, or by dilution manipulations (4). Increasing the gradient, strength might seem the simpler approach. However, the difficulty of using a large gradient is that the receiver bandwidth must be increased to accommodate the spread in resonance frequencies and therefore more noise is introduced into the resultant image. The noise content is proportional to the square root of the receiver bandwidth, and hence the time to acquire a given quality image, in both resolution and sensitivity, depends on the line width.

Many solid-state imaging techniques use spin coherences refocused by *echoes* for different purposes: (*1*) To record very short free induction decays present, in general, for solids and/or in the presence of strong field gradients. (*2*) For space encoding during the echo time. (*3*) For line narrowing by homonuclear or heteronuclear dipolar decoupling. (*4*) Reconversion of multiple-quantum (MQ) coherences into detectable single-quantum coherences. The properties of the spin echoes that refocus inhomogeneous and homogeneopus spin interactions have been discussed in the previous section. Also mixed echoes can be produced which eliminate all internal and external spin interactions. In the maximum of a mixed echo, each individual spin is fully isolated in the rotating reference frame in the absence of relaxation processes; a "time-suspension" process is taking place.

Methods of liquid-state imaging which can be applied, for instance, for analysis of elastomers or polymer swelling have been reviewed on several occasions (see for instance, References 19,47,135, and 139–141). Many of the methods used to record NMR images of solids can be combined with spectroscopic information. This unique feature and the richness in parameter contrast compensate for the relatively modest spatial resolution in many applications. If the spatial information is phase encoded, ie, indirectly detected, then the spectroscopic dimension is scanned directly, in many cases, by means of spin-echoes and in the absence of gradients. This approach is referred to as spectral frequency encoding. On the other hand, the spectroscopic information can be phase encoded or detected indirectly in the same way as in conventional two-dimensional spectroscopy. This approach is referred to as spectral phase encoding.

Spin System Response for a Heterogeneous Sample. In the following, a heterogeneous sample having magnetically equivalent nuclei with magnetogiric ratio γ and the local spin density $\rho(\vec{r})$ is considered. The space localized thermodynamic equilibrium magnetization corresponding to a voxel with coordinates (x, y, z) of the position vector $\vec{r}$ is given by $m_0\,(x, y, z) = C\rho(x, y, z)$, where C is the Curie constant. In the rotating reference frame at the resonance frequency,

the single-pulse NMR spin system response $s(\vec{r},t)$ can be expressed by the local free induction decay (FID) $f(\vec{r}, t)$,

$$s(\vec{r},t) = C\rho(\vec{r})f(\vec{r},t) \tag{35}$$

Spatially resolved NMR is concerned with unraveling the spatial distribution of $\rho(x, y, z)$ and measuring associated NMR parameters at individual "volume cells", or voxels at space point specified by the vector $\vec{r}$. If many contiguous voxels are investigated on a plane, or if a projection is investigated, one refers to NMR *imaging*, if individual voxels are investigated one refers to volume-selective NMR.

The spin density distribution can be resolved by different techniques. The standard approach exploits the possibility of introducing space dependence to the resonance frequency ω in each voxel by superposing a magnetic field gradient to a homogeneous magnetic field $\vec{B}_0(0,0,B_0)$ by the use of additional coils. In general, the field gradient is a Cartesian tensor with nine components related by the Maxwell equations. In the limit of large static magnetic field and small gradient, the gradient tensor can be reduced to a gradient vector $\vec{G}$ for an approximate description of the imaging experiments with good accuracy. Then the resonance frequency becomes dependent on the space vector $\vec{r}$, ie, $\omega(\vec{r}) = \gamma(B_0 + \vec{G}\cdot\vec{r}) = \omega_0 + \gamma\vec{G}\cdot\vec{r}$, where the field gradient vector collects the derivatives of the magnetic field in the z-direction with respect to the space coordinates defined by the component of the field gradient: $\vec{G}(\partial B_0/\partial x, \partial B_0/\partial y, \partial B_0/\partial z)$.

The total time-dependent signal of an inhomogeneous object of volume V measured in a magnetic field gradient and in rotating frame at the angular frequency ω_0 is given by

$$S(t) \propto C\iiint_V \rho(x,y,z)f(x,y,z,t)\exp\{\mathrm{i}\gamma\vec{G}\cdot\vec{r}t\}\,\mathrm{d}x\,\mathrm{d}y\,\mathrm{d}z \tag{36}$$

In high magnetic field the spatial dependence of the Curie constant can be neglected in a good approximation.

In order to illustrate the basic concepts of space encoding time-dependent gradients $\vec{G}(t)$ shall be admitted. The wave vector $\vec{k}$ can be introduced which is the Fourier conjugate to the space variable $\vec{r}$,

$$\vec{k}(t) = \gamma\int_0^t \vec{G}(t')\,\mathrm{d}t'. \tag{37}$$

In this notation, the single-pulse response signal in time-dependent main field gradients becomes

$$S(t) \propto C\iiint_V \rho(x,y,z)f(x,y,z,t)\exp\{\mathrm{i}\vec{k}(t)\cdot\vec{r}\}\,\mathrm{d}x\,\mathrm{d}y\,\mathrm{d}z. \tag{38}$$

This equation is the starting point for the discussion of spatial resolved NMR basic procedures.

Spatial Resolution by Frequency Encoding. The principle of the spatial resolution of NMR imaging by frequency encoding is discussed in the following in the presence of a pulsed uniform gradient, say $G_x = \partial B_0/\partial x$. After the radio-frequency excitation pulse the quantity $k_x(t)$ grows linearly with time according to equation 37, ie, $k_x(t) = \gamma G_x t$. Thus, $\vec{k}$ space is sampled in the direction of k_x, and time t and k_x are equivalent variables. If t is replaced by $k_x/(\gamma G_x)$ the spin system response given by equation 38 becomes

$$S(k_x/(\gamma G_x)) \propto C \iiint_V \rho(x, y, z) f(x, y, z, k_x/(\gamma G_x)) \exp\{i\gamma k_x \cdot x\} \, dx \, dy \, dz \tag{39}$$

The complex FID signal acquired in this way is composed of contributions evolving according to the local offset resonance frequency $\gamma G_x x$ labeling the nuclei responsible for this local transverse magnetization, hence, the term frequency encoding. Note that this is the conventional way of encoding in the Fourier transform spectroscopy. However, in context with NMR imaging, signals are processed in terms of the wave numbers k_x rather than of offset frequencies. The Fourier transform over k_x produces the convolution of the Fourier transform of the functions $\rho(x, y, z)$ and $f(x, y, z, k_x/(\gamma G_x))$. If $f(x, y, z, k_x/(\gamma G_x)) \approx f(k_x/(\gamma G_x))$, the Fourier transform of the FID is the space-dependent spectral response $F(x)$ and the Fourier transform of the triple integral is a projection $P(x) = \int\int \rho(x, y, z) \, dy \, dz$ of the spin density on the x-axis. Then, the Fourier transform of equation 39, can be written as

$$S(x) \propto C \int_{x_{\text{sample}}} F(x - x') P(x') \, dx' \tag{40}$$

where x_{sample} represents the sample size in the x-direction. A faithful representation of the spin-density projection $P(x)$ would be obtained by this method of frequency encoding only if the spectrum $F(x - x')$ is a Dirac function $\delta(x - x')$, or a narrow NMR absorption line like for liquid samples.

The above discussion is illustrated in Figure 24. If the samples are liquid, a narrow NMR absorption line is observed for both samples in a homogeneous magnetic field and a projection of the object along the x-axis is measured in the presence of the field gradient G_x. The signal amplitude at each resonance frequency or space coordinate is determined by the number of spins that experience the same magnetic field strength. If the spectrum in a homogeneous field is broad like in the solid samples (bottom traces) then the convolution (cf eq. 40) of the projection of the spin density by the line shape becomes noticeable, and the spatial features are smeared out. Thus, the minimum distance Δx which can be resolved is defined by the ratio of the full width at half spectral intensity $\Delta\omega_{1/2}$ of spectral features to the spread of the resonances introduced by the field gradient, ie,

$$\Delta x = \frac{\Delta\omega_{1/2}}{\gamma G_x} \tag{41}$$

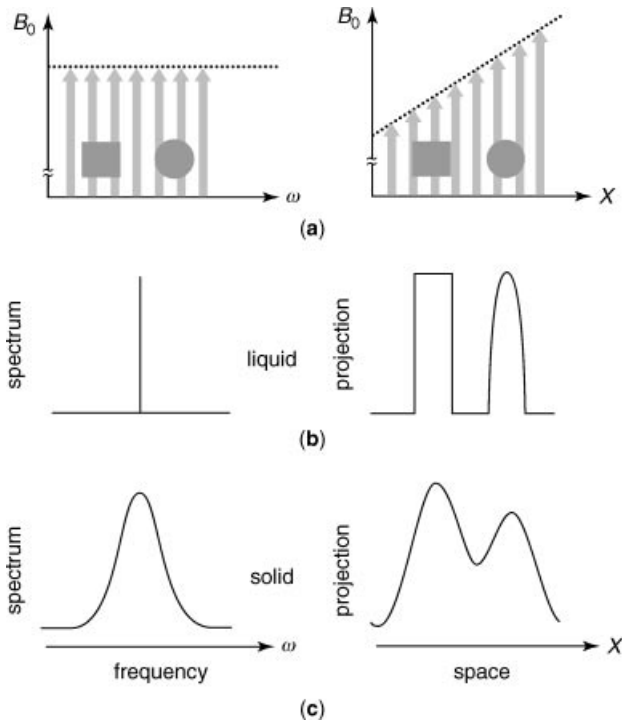

Fig. 24. Effect of field gradient on the NMR signal. The samples consists of a rectangular and a circular object. (**a**) Homogeneous magnetic field (left) and magnetic field with a linear space dependence (right). (**b**) Spectroscopic response for a liquid sample with a single, narrow line in the NMR spectrum. (**c**) Spectroscopic response for a solid sample with a single, broad line in the NMR spectrum. Reproduced from Ref. 136, with permission from Wiley.

Clearly, equation 41 indicates that when the line width increases, the gradient strength G_x also has to be increased, at least when the resolution Δx is to be kept constant.

Spatial Resolution by Phase Encoding. Broadening of the projection by the NMR spectrum (cf eq. 40 can be avoided if the spatial information is detected indirectly in the fashion of the multidimensional Fourier NMR spectroscopy (1). For instance, a magnetic-field gradient G_y is switched on for an evolution time t_1 following a radio-frequency excitation pulse, and the signal is acquired in a detection time t_2 after the gradient has been switched off. For this 2D scheme, the NMR signal can be written as

$$S(t_1, t_2) \propto Cf(t_1) f(t_2) \int_{y_{\text{sample}}} P(y) \exp\{i\gamma k_y y\} \, dy \tag{42}$$

where k_y- $\gamma G_y t_1$ and $P(y) = \int\int \rho(x, y, z) \, dx \, dz$. It becomes clear that there are two ways to perform the experiment: either t_1 is varied in the custom of 2D NMR spectroscopy, or t_1 is kept constant and G_y is stepped in increments ΔG_y. The first

case bears no advantage compared to direct frequency encoding discussed above. As time t_1 proceeds, not only does k_y increase, but also the free induction decay $f(t_1)$ evolve and deteriorate the signal intensity and finally the spatial resolution. But, if t_1 is kept constant $f(t_1)$ has a fixed value, and the phase change of the signal in the evolution period depends only on the wave vector k_y. Thus, the spatial resolution achievable for phase encoding depends on the maximum gradient strength available and on the signal-to-noise ratio, because the signal strength decreases with increasing $\vec{k}$.

The digital resolution or the pixel resolution of an NMR image can be much higher than the actual space resolution. The digital resolution $1/\Delta y$ of the NMR imaging in y-direction is determined by the maximum value of k_y or equivalently by the number n_y of complex signal values and the $\vec{k}$ space sampling intervals Δk_y, ie, $1/\Delta y = n_y\ \Delta k_y/(2\pi)$. To avoid signal aliasing, k_y has to be stepped in small enough intervals so that the signal-phase increment $y_{\max}\ \Delta k_y$ for the maximum object coordinate $y_{\max}$ never exceeds 2π.

Sampling $\vec{k}$ Space. Different imaging schemes are often discriminated against the way $\vec{k}$ space is sampled (for more details see Reference 19).

Two elementary 2D NMR imaging methods are illustrated in Figure 25: 2D Fourier imaging (2DFI, Fig. 25**a**) and back-projection imaging (BPI, Fig. 25**b**). Orthogonal gradients are switched subsequently in 2DFI and simultaneously in BPI. As a consequence, $\vec{k}$ space is sampled in orthogonal coordinates for 2DFI.

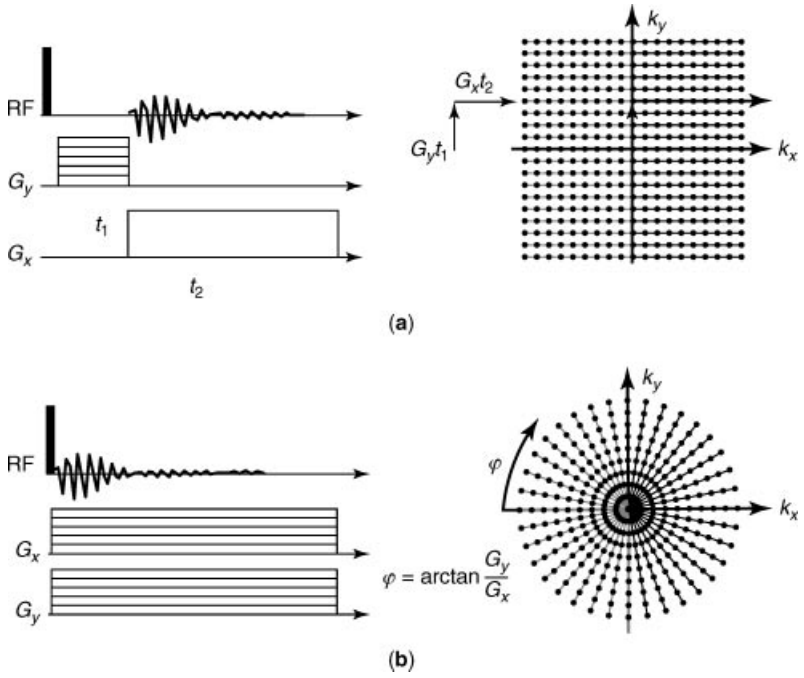

Fig. 25. Schemes for acquisition of 2D NMR images. Excitation and detection schemes (left) and maps in $\vec{k}$ space, where NMR signals is acquired (right). Reproduced from Ref. 136, with permission from Wiley.

When applied simultaneously, the direction of the resulting gradient changes depending on the relative strengths of G_x and G_y gradients. In this way, $\vec{k}$ space can be sampled in cylindrical coordinates in BPI. In either case, the image is obtained by the Fourier transformation of the $\vec{k}$-space data.

Often phase and frequency encoding are combined for acquisition of two-dimensional (2D) images (cf Fig. 25**a**, left). Then the gradient G_y is called the phase encoding gradient, and G_x is the frequency encoding gradient. This is one of the most used methods for recording images in elastomers materials that are soft solids with NMR line widths $\Delta\nu_{1/2} \approx 100$ Hz/1 kHz.

Contrast in NMR Imaging. Compared with other image-forming methods, the NMR imaging is characterized by the abundance of parameters that can be exploited for producing contrast (142,143). Many features invisible to other image-forming techniques can thus be visualized with NMR. To exploit the diversity of contrast features, it is useful to optimize the imaging experiment for generation of maximum contrast. The local contrast C is defined as the relative difference in image intensities M of neighboring structures i and j (17)

$$C = \frac{|M(\vec{r}_i) - M(\vec{r}_j)|}{|M_{\max}|} \tag{43}$$

where $|M_{\max}|$ is the absolute maximum of $M(\vec{r}_i)$ and $M(\vec{r}_j)$, where $\vec{r}_i$ and $\vec{r}_j$ are the space coordinates of voxels i and j under consideration.

Contrast Parameters and Material Properties. The contrast parameters relevant for polymer characterization by NMR imaging are directly related to the spin density, static and fluctuating nuclear spin interactions, and to the mass transport parameters. Even if the above quantities can change on molecular or mesoscopic scale only the variation of them on the space domains larger than the resolution of image can be detected in NMR imaging. The residual dipolar and quadrupolar interactions are related to the NMR parameters like van Vleck moments (4) and relaxation times (144). The fluctuating part of spin interactions leads to a variety of contrast parameters of magnetization relaxation type like spin-lattice relaxation in the laboratory reference frame (T_1), rotating frame (T_{1r}), transverse relaxation (T_2), solid echo or coherent averaging pulse sequences decay time (T_{2e}) (4), and dipolar correlation decays (5). The relaxation NMR parameters are also related to the manipulation of sample by contrast agents like paramagnetic relaxation agents, ferromagnetic particles (17), and hyperpolarized xenon (145,146).

The chemical shielding interaction leads to chemical contrast parameters related to the chemical composition as well as molecular orientation. Differences in magnetic susceptibility and the distribution of magnetic fields produced by electrical currents can be also detected via chemical shift (19).

The NMR quantities defining the contrast of NMR images depend on various macroscopic and microscopic physical and chemical parameters of the investigated samples that affect the nuclear spin interactions or molecular transport parameters. They can be classified as internal and external. Moreover, they can be state parameters that are stationary quantities like stress, strain, moduli of shear and compression, cross-link density, distribution and agglomeration of filler particles, molecular orientation, fibril orientation and domain size distribution,

distribution of voids, and the temperature distribution. Transition parameters or kinetic parameters characterize the time evolution of the polymer system. They are determined in *in situ* NMR experiments or in stop-and-go experiments. Examples are characteristic times of chemical and physical aging (147,148) of vulcanization (149) and curing (150) processes of heat dissipation and fluid permeation (151,152).

Transition parameters can be determined directly from the analysis of the time evolution of changes in NMR images, but state parameters must be related to NMR parameters either by theory or calibration. Theories have been published that relate the cross-link density of unfilled and filled elastomers to the parameters of transverse relaxation parameters (153) and others relating dynamic storage modulus of polymers to the cross-polarization rate (154).

A simpler approach is based on empirical correlations between NMR parameters and sample properties, which often can be established by calibration of an NMR parameter against a material parameter (155,156). An example of stress–strain calibration is given in Figure 26 by calibration of T_2 of filled poly(dimethyl siloxane) rubber against strain (153), (cf Fig. 26**a**). By use of the stress–strain curve (Fig. 26**b**) from mechanical measurements, T_2 can be calibrated against stress (see Fig. 26**c**).

The procedure can be used to translate the spatially resolved NMR parameters T_2 into values related to the strength of local stress.

Another possibility is given by the observation of the quadrupole splitting in deuteron NMR (155,157). For small strain, the splitting Δ_Q is linearly proportional to $\Lambda^2 - \Lambda^{-1}$ where $\Lambda = \frac{L}{L_0}$ is the elongation ratio, L and L_0 are the length of polymer band after stretching and in the relaxed state, respectively (see Fig. 27).

The rubber samples are prepared by swelling in a solution of deuterated spy molecules, these molecules follow the polymer network alignment under strain and the residual quadrupolar coupling that results from their anisotropic motion is observed either by spectroscopic imaging or by double-quantum imaging (158,159). The above deuteration procedure leads to the modification of the network and to potential modulation of the NMR signal encoding by the self-diffusion of the incorporated oligomers.

The above adverse effects can be avoided if ^{1}H residual dipolar couplings of elastomer chains (68) were used to generate contrast in NMR imaging of stretched samples. Dipolar contrast filters can be implemented based on dipolar encoded longitudinal magnetization as well as double- and triple-quantum coherences (160,161). The associated contrast filter parameters were investigated by measurements of the line width in ^{1}H multiple-quantum filtered spectra, the dipolar encoded longitudinal magnetization decay curves, and the double- and triple-quantum buildup curves as a function of the extension ratio for a natural rubber band. Together with stress–strain measurements, these results allow for correlation of ^{1}H residual dipolar couplings with stress values in stretched natural rubber.

Magnetization Filters. The contrast generation in NMR imaging is directly related to the concept of magnetization or coherences filters. Various molecular (internal) or external parameter weights are introduced by the use of magnetization or coherences filters (Fig. 28), which block part of the incoming signal originating from the thermodynamic equilibrium magnetization.

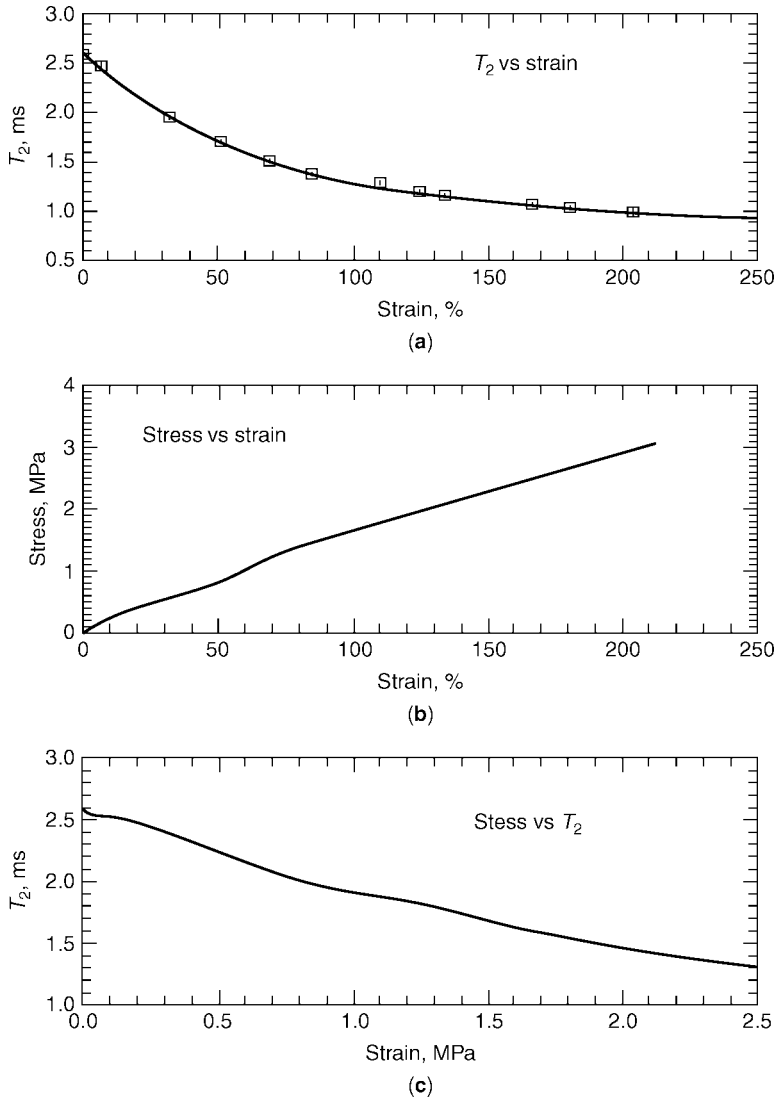

Fig. 26. Calibration of T_2 values measured for different strain (**a**) of filled poly(dimethyl siloxane) against stress (**c**) by use of the mechanical stress–strain curve (**b**). Reproduced from Ref. 142, with permission from Wiley.

As a result, there is a gain in selectivity of the output signal at the expense of a deterioration of signal-to-noise ratio.

A generic scheme for contrast optimisation in the Fourier NMR imaging is illustrated in Figure 28**b**, (142). In general, three periods are distinguished: a filter period, a space-encoding period, and a spectroscopy period. For image contrast other than the often-uninformative spin density, the space-encoding period must be combined either with a magnetization filter or with spectroscopic data acquisition or both. The signal detected after the action of the general pulse sequence

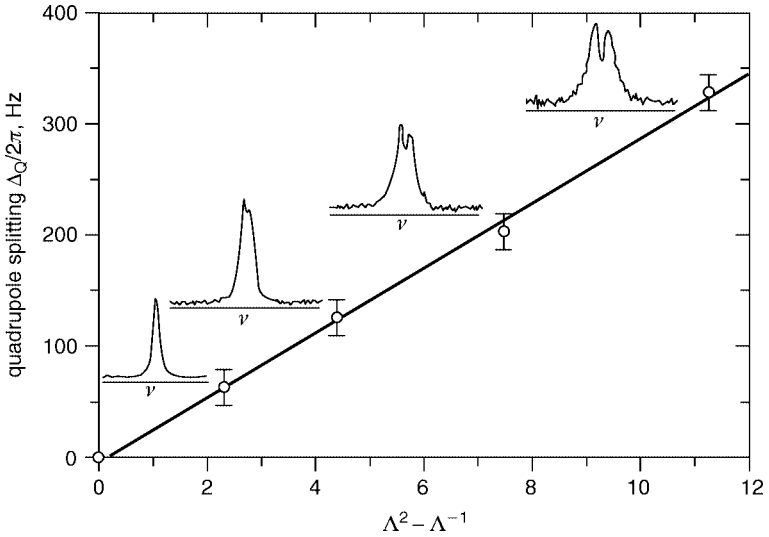

Fig. 27. Deuteron quadrupolar splitting of 1,4-tetra-deuterated butadiene oligomers from natural rubber bands for different strains. Reproduced from Ref. 142, with permission from Wiley.

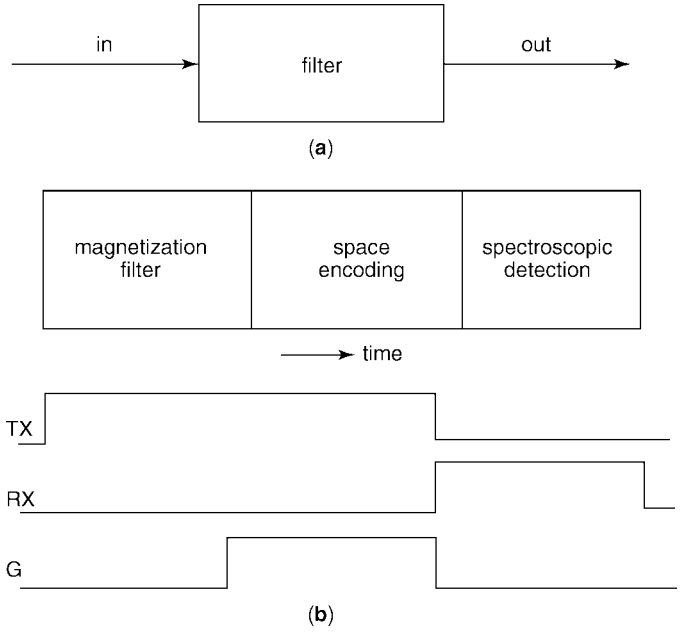

Fig. 28. (**a**) A magnetization filter blocks part of the incoming magnetization or spin coherences. (**b**) General scheme for generation of NMR image contrast. Initial nuclear magnetization is filtered by the radio-frequency irradiation of resonant nuclei (TX) before or also during space encoding period by magnetic-field gradients ($\vec{G}$). In the absence of gradients, the NMR signal is detected (RX) for the extraction of spectroscopic information. Reproduced from Ref. 143, with permission from Wiley.

designed to introduce image contrast can be written as (162)

$$S(\vec{k}) = \int \rho(\vec{r}) F_c(\{p\}, \vec{r}) \exp[-i\,2\pi \vec{k} \cdot \vec{r}]\, d\vec{r} \tag{44}$$

where the contrast parameter manifold is denoted by $\{p\}$ and $F_c(\{p\}, \vec{r})$ is the combined local contrast function. This function could be a product of several parameter contrast functions, such as

$$F_c(\{p\}, \vec{r}) \equiv F_c(T_1, \vec{r}) F_c(T_{1\rho}, \vec{r}) F_c(T_2, \vec{r}) F_c(\delta_i, \vec{r}) F_c(\vec{q}, \vec{r}) \cdots \tag{45}$$

where for instance, the contrast factors in the right-hand side of equation 45 representing the effects of longitudinal (T_1 and $T_{1\rho}$) and transverse (T_2) relaxation times, chemical shift (δ), and the effect of coherent and incoherent molecular translation motions described in the $\vec{q}$ space (18).

There are two basic approaches by which the image contrast can be studied. The first makes the pulse sequence sensitive to a particular contrast parameter p so that the image intensity bears or is weighted by the influence of that contrast. This approach offers the advantage of time efficiency but is only qualitative. The quantitative information can be obtained by the second approach that include inter alia two-image scheme (162). This method requires two imaging experiments under two contrast conditions. The final parameter map is computed from the two images, voxel by voxel, by means of some mathematical calculation, such as division.

The first approach is illustrated in Figure 29 for the simple case of spin-lock-filtered projections of a composite piece of rubber cut from the tread of a car tire. Such a filter imposes a $T_{1\rho}$ weight on the spin density (cf Fig. 29**a**). From the space distributed magnetization decays, the parameter map of $T_{1\rho}$ can be obtained (cf Fig. 29**b**) independent of spin densities.

An important class of magnetization filters are mobility filters which select magnetization based on the time scale of segmental motions ((19), and references therein). The parameters for discrimination are the amplitude and characteristic frequency or the correlation time τ_c of molecular motions. The effect a filter exerts on a NMR signal can be represented by the filter transfer function. Examples are given in Figure 30 (163,164) with transfer function for filters, which select magnetization based on the time scale of molecular motion.

Depending on the time scale, different pulse sequences can be used. In the fast motion regime, T_1 filters are applicable. Both saturation recovery and the stimulated echo can be used for this, but the transfer function of both filters is complementary. The spin-echo or Hahn echo filter has a transfer function similar to that of the saturation recovery filter, but because T_2 processes are efficient at slower molecular motions, the filter cut off is shifted to longer correlation times. The dipolar filter exploits the strength of the dipolar couplings averaged by the molecular motions. The residual dipolar filters can use ^{1}H double- and triple-quantum coherences (160,161) as well as ^{1}H–^{1}H magnetization exchange (165). Dipolar correlation effect detected via stimulated echo can be used for a mixed residual dipolar coupling/slow motion filter (166). Resolved splitting of the residual quadrupolar coupling of ^{2}H of spy molecules has been used as quadrupolar

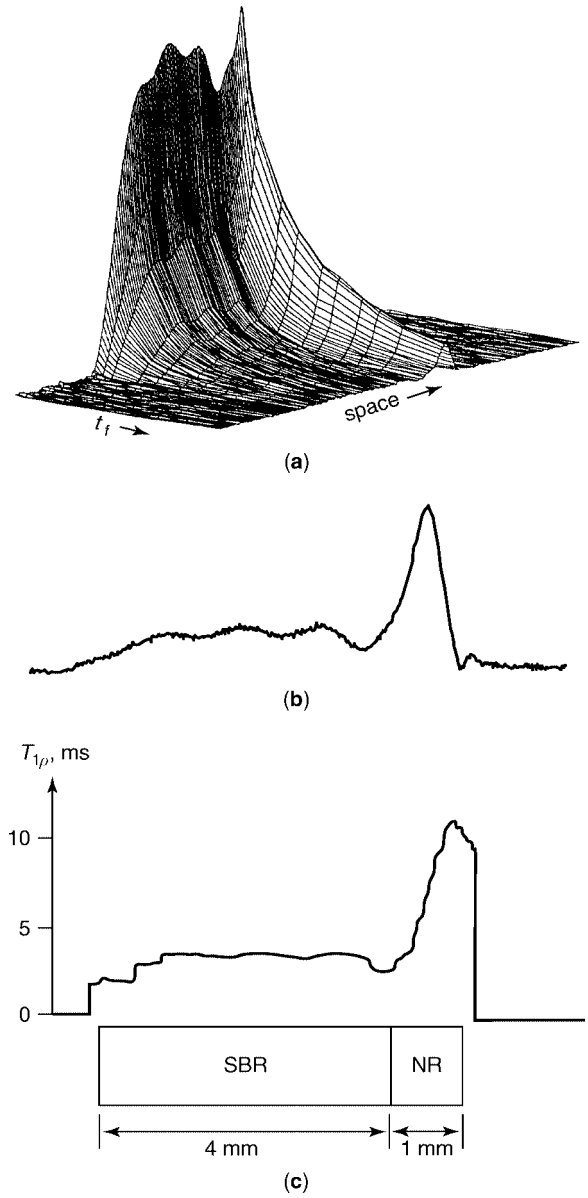

Fig. 29. Filter-weighted and spin-lattice relaxation in the rotating frame $T_{1\rho}$ of an elastomer composite of SBR and natural rubber cut from the tread of a car tire. (**a**) A stack of one-dimensional ^{1}H images with variable duration t_f of the spin-lock radio-frequency magnetic field. (**b**) A $T_{1\rho}$ parameter map obtained from the decay shown in (**a**). Reproduced from Ref. 143, with permission from Wiley.

coupling filter (158,159). The spin-lattice relaxation in the rotating frame or $T_{1\rho}$ filter is efficient at slow motions with correlation times of the order of the inverse of the angular frequency of the spin-look radio-frequency pulse. The transverse magnetization decay for a train of solid echoes or magic echoes is characterized

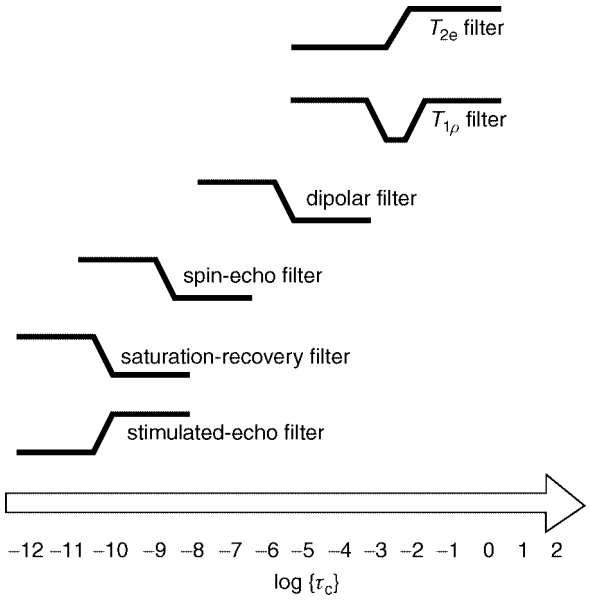

Fig. 30. Time scale of molecular motion and filter transfer functions of pulse sequences, which can be used for selecting magnetization according to the time scale of the molecular motion. Reproduced from Ref. 143, with permission from Wiley.

by the effective transverse relaxation time T_{2e} (68) a parameter sensitive to the slow segmental motion like $T_{1\rho}$.

The identification of material heterogeneities based on differences in molecular motion is an important feature of NMR imaging. The importance of slow molecular motion for image contrast is demonstrated in Figure 31 with relaxation time parameter images through a partially aged sheet of carbon-black-filled styrene-*co*-butadiene rubber (SBR) (147).

The one-dimensional space scale starts at the unaged center of the rubber sheet at $\Delta r = 0$ and ends at the aged surface at $\Delta r = 700$ μm. Two curves are shown for each relaxation parameters as a function of space. The top curve is for unaged material and it varies little with space. The bottom curve is for the aged material. Both curves overlap in the center of the sheet and split toward the surface. The splitting is a direct measure of image contrast. The contrast is largest for those relaxation times that are sensitive to slow molecular motions. the contrast is largest for T_{2e} and $T_{1\rho}$ images and almost zero for T_1.

NMR Imaging of Elastomers

Potentially rather useful applications of NMR imaging are in elastomer industry. This section features some selected examples that illustrate the type of information obtained by imaging of elastomers. Such applications to elastomers concern distribution in temperature stress, cross-link density, modulus, and the dynamics of fluid absorption and swelling.

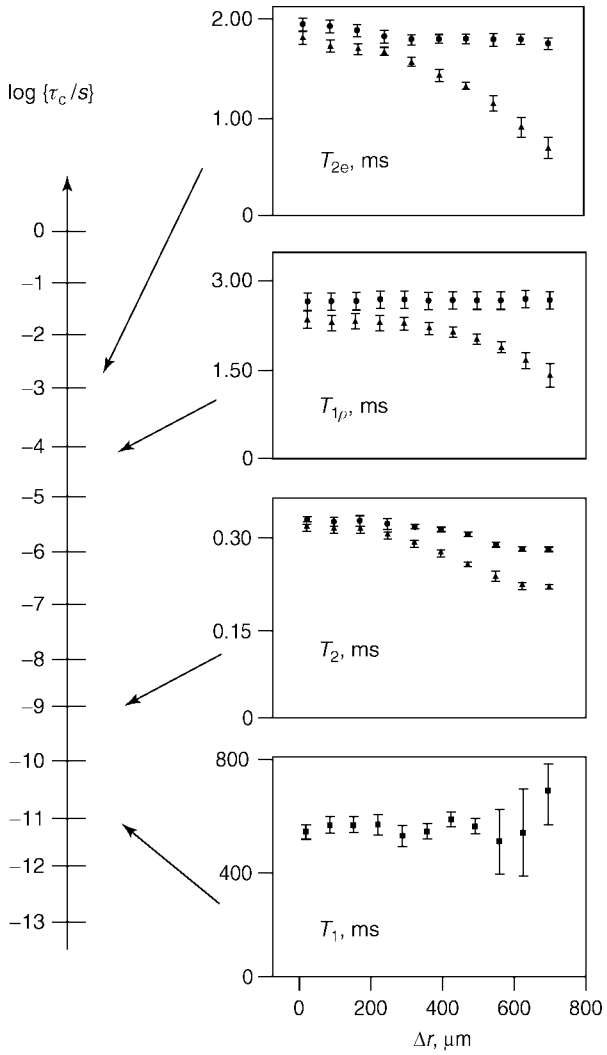

Fig. 31. Relaxation parameters T_1, T_2, $T_{1\rho}$, and T_{2e} for contrast in thermal oxidative aging of SBR. The insets depict the space distribution of relaxation times for a partially aged (lower curve) and an unaged (upper curve) rubber sheet. Reproduced from Ref. 147, with permission from Wiley.

Heterogeneities in Elastomers. Heterogeneities in elastomers materials are related to the defects induced in the process of preparation. The processes that lead to the defects are as follows.

Mixing Processes. Technical elastomers are blends of up to about 30 different compounds like natural rubber, styrene–butadiene rubber, silicate and carbon-black fillers, and mobile components like oils and waxes. Improper mixing leads to inhomogeneities with corresponding variation in mechanical and thermal properties. An important source of heterogeneities of this type is represented by filler

clusters. Even the variance of the distribution statistics of active filler may lead to heterogeneities detected as an average over a volume cell or voxel with the spatial resolution of NMR imaging.

Vulcanization. Heterogeneous structures arise from effects of thermal conductivity, which lead to space-dependent temperature profile during the vulcanization process depending on the position of the heat source and on heat dissipation. As a result, inhomogeneous cross-link densities may be established (167). If the process of cross-linking is incomplete the defects represents by the free chains are also presents. The changes in segmental mobility from progress of the vulcanization reaction and from the associated sample temperature distribution can be monitored directly by the NMR imaging *in situ* (149). In the covulcanization of blends and sheets from different formulations, inhomogeneities in cross-link density max arise from differences in solubility and diffusion of curatives (168).

Aging. Aging processes are often induced by ultraviolet (UV) irradiation or other ionization radiations (169), exposure to heat and oxygen, and by biological mechanisms. Depending on the load applied, different aging processes are observed (170). The action of electromagnetic radiation with high energy of the associated photons as well as nuclear irradiation will produce chain scission with decrease in the cross-link density and associated increase in chain mobility. Thermal oxidative aging usually leads to the formation of hardened surface layers in natural rubber (NR) as well as synthetic rubber (styrene-*co*-butadiene rubber (SBR) (147,148,171–174). Typically, these layers approach a thickness of 200–300 μm and inhibit progress of the aging process further into the bulk of thin sample. The material hardening is explained by an increase in cross-link density. In the absence of oxygen, chain scission may dominate at elevated temperatures with an associated increase in the segmental mobility. Other types of aging involve aggressive fluids and gases. In this context, a sample of degraded rubber hose gas been investigated (175), but also the degradation of polyethylene pipes and the enzymatic degradation of biologically synthesized polymers (176) have been studied through NMR imaging. Related investigations have been carried out on asphalts (177). Aging associated with swelling of the rubber particles has been observed in crumb-rubber modified asphalts (178).

Mechanical Load. Static mechanical load by strain leads to stretching of random-coil polymer chains in the direction of sample elongation and chain compression in the orthogonal directions. The value of the residual dipolar and quadrupolar couplings is increased by the mechanical load, and moreover, the distribution of the correlation times is also modified. Therefore, many NMR parameters sensitive to the residual dipolar couplings and slow motions can be used for characterization of the local strain–stress effects in heterogeneous elastomers (158,160,161,179). Dynamics mechanical load leads to sample heating where the temperature distribution in dynamic equilibrium is determined by the temperature-dependent loss-modulus and the thermal conductivity of the sample. Because transverse relaxation rate (approximated by the T_2 relaxation) scales with the temperature for carbon filled SBR, a T_2 map provides a temperature map of the sample. Such temperature maps have been measured for carbon-black filled SBR cylinders for different filler contents and mechanical load (180).

NMR Images and Parameter Maps in Elastomers. NMR of elastomers including NMR imaging appears to address one of the industrially most relevant applications of NMR. Applications of the one- (1D) and two-dimensional (2D) NMR images and parameter maps for characterization of elastomer materials with heterogeneous mesoscopic and macroscopic structure will be reviewed in the following.

Vulcanization and Covulcanization. The main effect taking place during the vulcanization process is the space distribution in the cross-link density. One source of this variation is the spatial distribution of the rubber formulation, although short-scale variations are often smoothed by component diffusion during the vulcanization process. Differences on the millimeter scale can lead to interfacial structures.

Another source of variations in cross-link density on the millimeter scale is the curing process in combination with the sample geometry. Heat is supplied to the sample for a certain time and after vulcanization is removed from the sample in certain time. Near the heat source the cross-linking process induced by vulcanization is set in first and near the heat sink is sets in last. Depending on the time dependence of the heat from the source and sink, surface and the thermal properties of the sample, complicated time-dependent temperature profiles are established in the sample.

The vulcanization process has been followed across a thick disk from unfilled SBR by NMR imaging of the effective transverse signal decay (149). The measurements were carried out in a magnetic field slightly inhomogeneous from the construction of a special vulcanization probe and the effective transverse relaxation time T_2^* was measured (see Fig 32). Despite accelerated signal decay from the field inhomogeneities, T_2^* still turned out to be sensitive to chain mobility because of a sufficiently strong contribution from T_2.

A nonlinear relationship between the effective transverse relaxation rate $1/T_2^*$ and the reduced shear modulus was found. Nevertheless, the relationship that low modulus corresponds to high T_2^* and high modulus to low T_2^* can be used to interpret the imaging data across the SBR sheet measured during the vulcanization process (see Fig. 32). Immediately after sample heating, chain mobility is high and so is T_2^*. With the formation of the cross-links chain mobility decreases and so does T_2^*. The vulcanization front is defined by the center of change in T_2^*. It can be seen to migrate through the thin sample on a time scale of about half an hour with the temperature in the range between 140 and 170°C across the sample. With increasing time the slope of the T_2^* curve flattens indicating a broadening of the reactive vulcanization zone.

Another example of spatial determination of the local cross-link density in inhomogeneous vulcanized elastomers by means of the spatially dependent T_2^* decay times was discussed on poly(isobutylene-*p*-methylstyrene-*p*-bromon-ethylstryrene) (PIB-PMS/BrPMS) (181). It was shown that by swelling the elastomers in the aprotic solvent CCl_4, the proton signal in the magnetic resonance images originates almost exclusively from the rubber methyl protons (182). This makes it possible to acquire selective images of the rubbery phase, which were demonstrated to be superior toward the visualization of the network homogeneity. Moreover, swelling of these elastomers in an appropriate solvent enhances the molecular chain mobility and reduces the

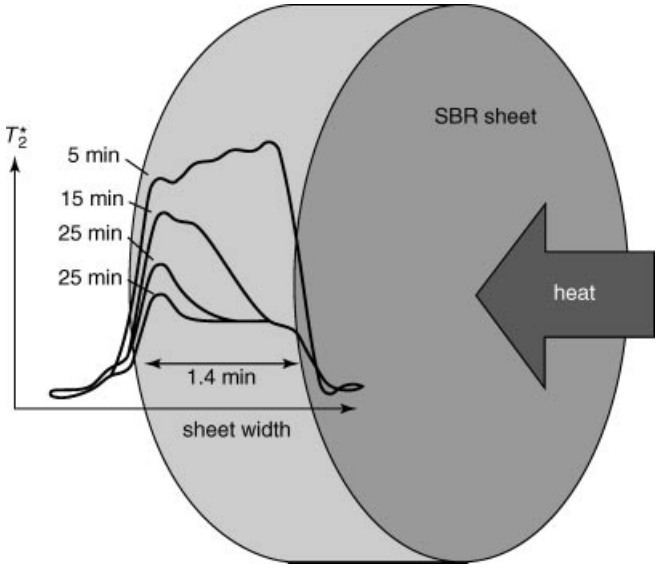

Fig. 32. Time-resolved T_2^* parameter one-dimensional images across a 1.4 mm thick sheet of SBR following the vulcanisation process. Reproduced from Ref. 149, with permission from Rapra Technology.

proton line width to an extent acceptable for recording magnetic resonance images.

The gravimetric Flory–Rehner (183) experiments are combined with NMR imaging to study spatially dependent degree of cross-linking, in unfilled, 1,6-hexamethylenediamine-cured PIB-PMS/BrPMS therpolymers (181). Localized relaxometry reveals two proton T_2^* relaxation decay times in CCl_4 swollen specimens: a fast decaying component reflecting the constrained chain segments near the cross-links and topological constraints (T_{2s}^*) and a slow decaying component originating from less constrained, remote chains (T_{2l}^*). On the basis of a linear relation between the bulk number-average molecular weight between effective cross-link ($M_{n,\mathrm{eff}}^{\mathrm{bulk}}$) and the volume average T_2^*, magnetic resonance images allow the determination of the local cross-link density in inhomogeneous cross-link PIB terpolymer samples by means of the spatially-dependent effective transverse relaxation. The measurements of the localized T_{2s}^*, and T_{2l}^* allow to deduce the localized molecular weight between the effective cross-links $M_{n,\mathrm{eff}}(\vec{r})$ for each region of interest labeled 1–10 in Fig. 33. This method reveals that the sample 1 exposes a very heterogeneous network structure as is illustrated by a large variation in the localized $M_{n,\mathrm{eff}}(\vec{r})$. This indicates an unfavourable mixing. This in strong contrast to specimen 2, having a rather homogeneous network structure as is demonstrated by the small variation in $M_{\mathrm{n,eff}}(\vec{r})$ as a result of a uniform curing. The homogeneity of mixing and curing of the specimens 3 and 4 (cf Fig. 33) is somewhere in between. These results clearly demonstrate that NMR image is a useful technique to investigate the homogeneity of mixing and curing of elastomers.

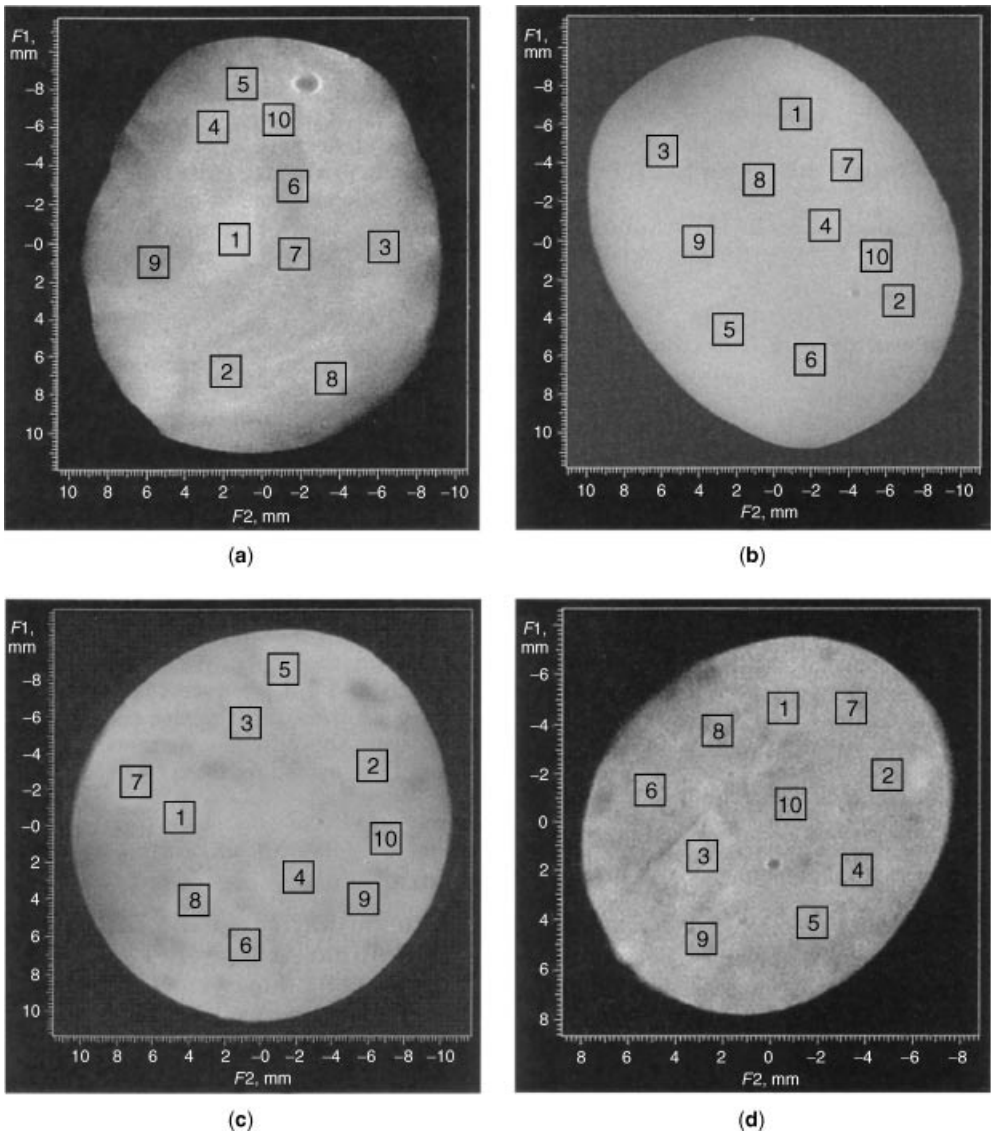

Fig. 33. Proton NMR images of unfilled polyisobutilene-based elastomers, cured with 1,6-hexamethylenediamine, after equilibrium swelling in CCl_4. The degree of cross-linking increases from samples 1 to 4. The regions of interest indicate the locations used to determine the local relaxation decay times. Reproduced from Ref. 181, with permission from American Chemical Society.

During fabrication of elastomer products like car tires different elastomer formulations often need to be covulcanizes. At the interface between an SBR and an NR layer, an interfacial layer with a modulus higher than either SBR and NR had been detected (145,171). In images detected using Hahn-echo method

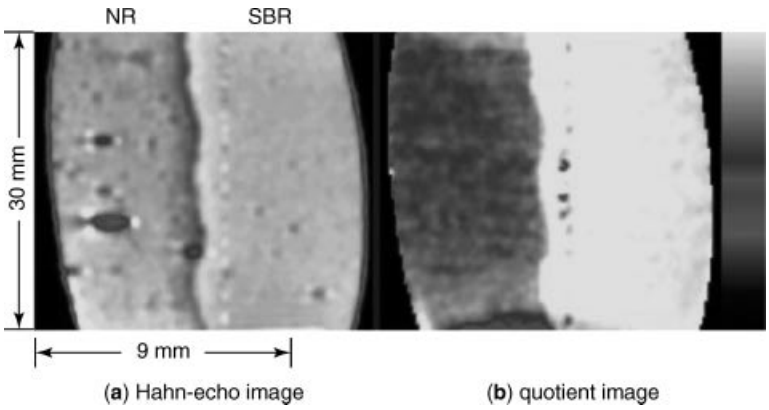

Fig. 34. Proton T_2^*-weighted Hahn-echo image (**a**) of an unfilled SBR/NR covulcanisate with dimensions 9 mm × 30 mm. The image has been acquired with an echo time of $t_E = 3.3$ ms. A quotient image (**b**) computed as the quotient of two Hahn-echo images acquired with different echo times of 4.2 and 3.4 ms. Reproduced from Ref. 145, with permission from Rapra Technology.

the interface is identified by a dark line paralleled to a slightly brighter line (see Fig. 34).

A mixture of spin density and relaxation forms contrast in the Hahn-echo image. Contrast in the quotient image is determined only by transverse relaxation. In this image, the interface appears abrupt and well defined. The image of the interface shows a transition from the hard SBR component to the soft NR component with a width of the order of 0–5 mm (184,185). This is the space scale on which the modulus changes. The shape and dimension of the interface are defined by the concentration differences in the vulcanizing agents, which diffuse at elevated temperatures across the interface until their diffusion is hampered by their role in the vulcanization reaction. Thus, the interface arises from a delicate balance between diffusion, reaction, heat supply, and removal.

Blending. Interfaces similar to those encountered during covulcanization may arise in blends with incomplete mixing. In unvulcanized samples, heterogeneities from blending can be deduced by gradient echo imaging, where the contrast is enhanced by differences in magnetic susceptibility of the components (186). However, fine structures are usually homogenized during the vulcanization process. Larger structures survive, in particular, when one component had already been vulcanized.

An example of such a case is illustrated in Figure 35 by two orthogonal slices through a block of a vulcanised blend from a soft (bright) and a previously vulcanised hard (dark) component (141). In slice (a), the structures invoked by mixing of components appear course but random, but slice (b) reveals stream lines of material flow in the rolling mill.

The presence of carbon-black filler usually does not affect the NMR data in contrast to functionalized silicate filler. This is attributed to rapid transverse relaxation of network chain segments near carbon-black filler particles caused by paramagnetic centers in the filler. Thus, for the technologically important

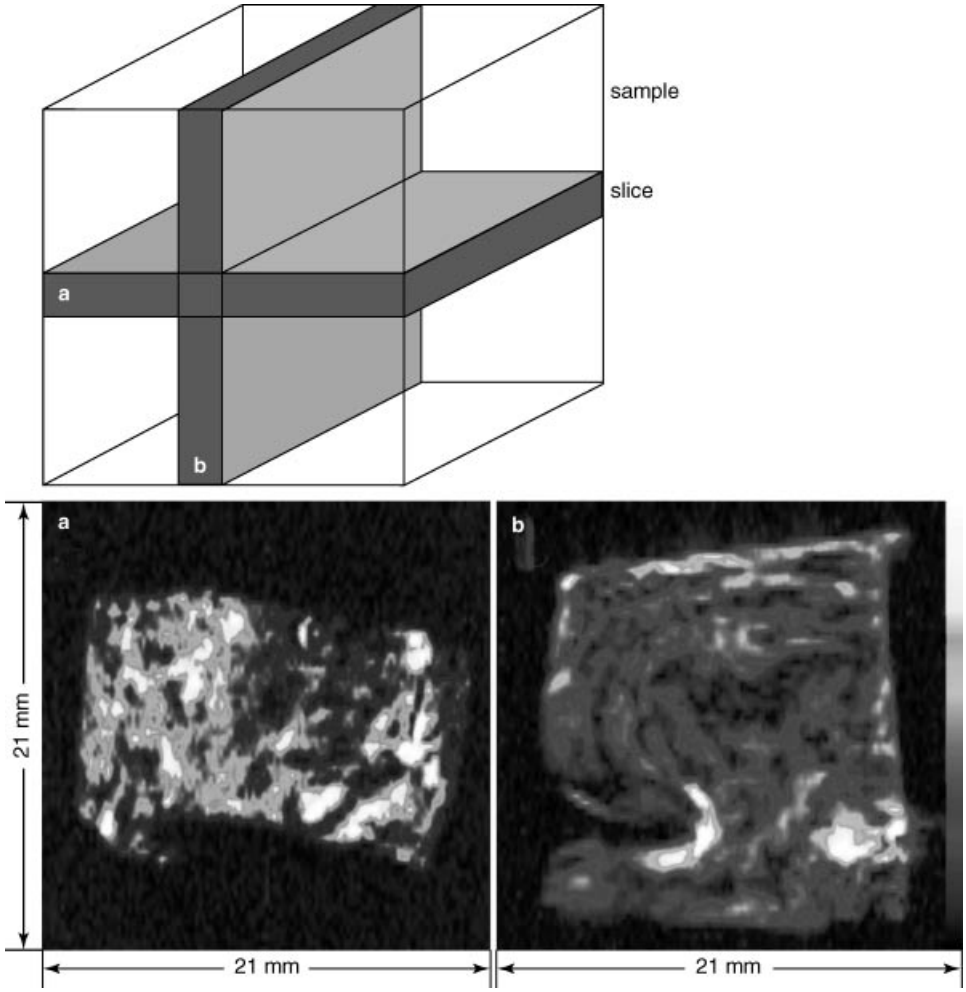

Fig. 35. (**a**) Proton T_2^*-weighted orthogonal slices of a carbon-black filled blend with a soft (bright) and a hard (dark) component. Insufficient blending in a rolling mill is visualized by the stream lines in slice (**b**). Reproduced from Ref. 145, with permission from Rapra Technology.

class of carbon-filled elastomers, NMR can provide the chemical cross-link density.

Aging. Aging of elastomers is a process that affects the mobility of intercross-link chains by packing, chain scission, and formation of new cross-links. Thermooxidative aging of many elastomers including SBR and NR leads to the formation of a brittle surface layer with reduced mobility that appears dark in ^{1}H Hahn-echo images. Often this region is followed by a zone of brighter image intensity, which can be attributed to chain scission or the accumulation of low molecular-weight additives (148).

The time evolution of the thermooxidative aging in SBR has been studied by NMR imaging (see Ref. 145). In order to detect the aged surface layer with reduced

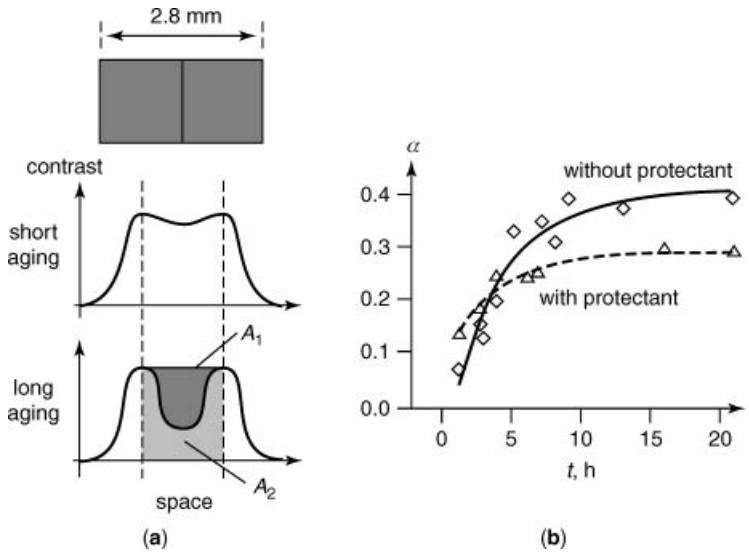

Fig. 36. Analysis of thermal oxidative aging by T_2^*-weighted Hahn-echo imaging. (**a**) Two SBR layers stacked after aging. The aged layer suffers a signal loss marked by the area A_1. The relative signal decrease defines the aging parameter α. (**b**) The progress in aging can be followed by evaluating the aging parameter α as a function of aging time t. Reproduced from Ref. 145, with permission from Rapra Technology.

signal intensity in Hahn-echo images, two aged sheets were stacked and the stack was imaged along its axis. In this way, the signal from the soft core delineated the hardened surface layers (cf Fig. 36).

Sample Deformation. Sample deformations modify the number of accessible conformations of intercross-link chains, so that they can be detected by analysis of relaxation and residual dipolar and quadrupolar couplings. For instance, dynamic mechanical load on elastomers is often exerted at small deformations and low deformation rates but over extended time periods. Then part of the mechanical energy is dissipated into heat depending on the value of the loss modulus. As a consequence, a temperature profile is established within the sample. Then the modulus varies across the sample depending on the temperature profile and properties determined for thick samples under dynamic load are average quantities.

The temperature profile associated with sample heating during weak dynamic shear deformation of carbon-black filled SBR cylinders of 10 mm diameter and 10 mm in height has been imaged by NMR by use of a specially designed probe (180).

The transverse relaxation time strongly depends on temperature (cf Fig. 37**a**), so that the temperature can be mapped by parameter imaging of T_2. Axial parameter projections have been acquired in dynamic equilibrium at a shear rate of 10 Hz and for carbon-black contents ranging from 10 to 70 phr. One-dimensional cross sections through those projections are depicted in Figure 37**b**. An increase of the temperature in the center of the sample is observed with increasing carbon-black contents which scales with the increasing loss modulus of

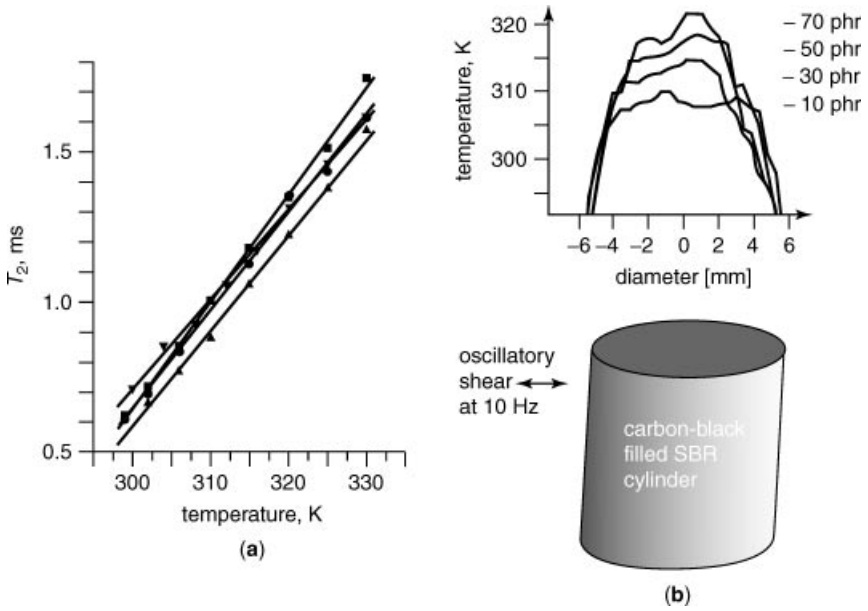

Fig. 37. Temperature profiles from T_2 parameter images of SBR cylinders with different carbon-black filler contents undergoing oscillatory shear deformations. (**a**) Temperature calibration curves and (**b**) temperature profiles across the cylinders. (■) 10 phr (●) 30 phr, (▲) 50 phr, and (▼) 70 phr. The pixel resolution was 0.4 × 0.4 mm^2. Reproduced from Ref. 180, with permission from Rapra Technology.

the sample. The 70 phr sample is warmer by over 10°C in the center of the sample than the 10 phr sample.

NMR Mobile Sensor for Quality Control of Elastomers. Over the last few years, a mobile NMR surface scanner called NMR-MOUSE has been developed for the nondestructive investigation of arbitrarily large objects (187,188). The NMR-MOUSE is a palm-size NMR device which is built up from two permanent magnets. The magnets are mounted on an iron yoke with antiparallel polarization to form the classical horseshoe geometry. The main direction of the polarization magnetic field $\boldsymbol{B}_0$ is across the gap and the field strength decreases rapidly with increasing distance from the surface. The radio-frequency (rf) field $\boldsymbol{B}_1$ is generated by a surface coil which is mounted in the gap. The NMR-MOUSE is characterized by strong inhomogeneities in the static and radio-frequency magnetic fields. Due to these fields inhomogeneities, NMR spectroscopy of the chemical shift is not possible, but magnetization relaxation times and parameters of translational motion can be measured by echo techniques (189–192). Moreover, the orientation dependence of NMR parameters can be easily investigated with the mobile NMR sensor for large samples on stretching devices (191).

Some selected applications of the NMR-MOUSE to elastomers are summarized in Figure 38 (193). In Figure 38**a**, transverse relaxation times have been measured for a series of carbon-filled NR samples with different curing times. Normalized values measured at high and homogeneous magnetic field (7 T, DMX 300) are compared to those measured with the NMR-MOUSE (0.5 T). Although

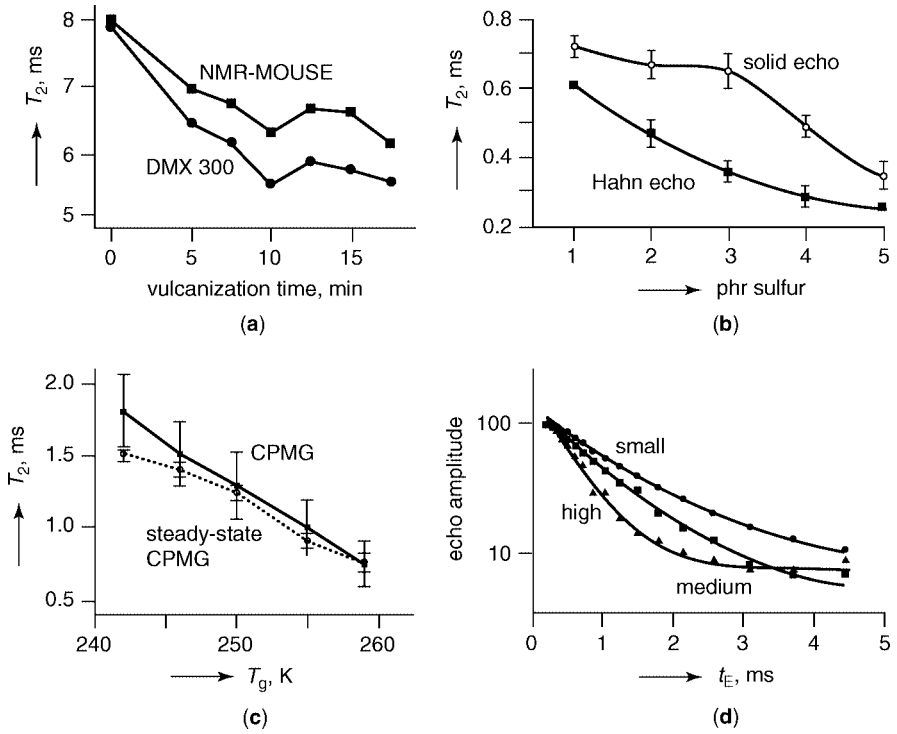

Fig. 38. Applications of the NMR-MOUSE to elastomer materials. (**a**) Values of ^{1}H T_2 for a curing series of carbon-black filled NR. The measurements made with NMR-MOUSE are compared with the values obtained at 300 MHz in high homogeneous field. (**b**) T_2 of a cross-link series of unfilled SBR with different sulfur contents. (**c**) T_2 versus glass-transition temperature T_g of unfilled SBR by the CPMG and steady-state CPMG methods. (**d**) Normalized Hahn-echo decays for polybutadiene latex samples for small, medium, and large cross-link densities. Reproduced from Refs. 189 and 190, with permission from Rapra Technology.

the values differ because of different $\boldsymbol{B}_0$ field strengths, they closely follow the same trend. This confirms that relaxation measurements by the NMR-MOUSE are a valid alternative to relaxation measurements at homogeneous magnetic fields.

In Figure 38**b**, relaxation times are shown for a series unfilled SBR samples with variations in sulfur content. With increasing sulfur content the chemical cross-link density increases. Relaxation times are given for measurements with Hahn echoes and with solid echoes. The change in relaxation times and thus the sensitivity of the method is larger for the Hahn-echo measurements at small cross-link density and for the solid echo measurements at high cross-link density. Solid echoes reduce the signal attenuation from the dipole–dipole interaction between two spins in addition to producing a Hahn echo. At high cross-link density multi-center dipolar couplings become effective and the solid echo becomes less effective in reducing signal attenuation from dipolar interactions. The Hahn echo does not

affect the dipole–dipole interaction at all. This explains the difference in contrast obtained with both methods.

A reduction in measurement time is gained when the measurements are performed in dynamic equilibrium between radio-frequency excitation and longitudinal relaxation (1). NMR methods which operate in this regime are referred to as steady-state methods. They deliver equivalent information compared to methods which demand complete relaxation to thermodynamic equilibrium between scans. T_2 measurements performed with the CPMG and the steady-state CPMG method are depicted in Figure 38**c** and correlated with the glass-transition temperature T_g of unfilled SBR laboratory samples of different cross-link densities. The NMR measurements were done at room temperature, whereas T_g had been determined by temperature-dependent measurements of the dynamic-mechanical loss modulus (189,190). The correlation between both measurements is not surprizing, because both probe the network dynamics. These data demonstrate that in certain cases T_g can be determined locally and nondestructively on large samples at room temperature by the NMR-MOUSE.

The large magnetic-field gradients give rise to rapid signal loss from molecules with translational motion, so that signal from low molecular-weight fluids is suppressed at echo times t_E of the order of 1 ms and more. The signal detected at larger echo times is from larger molecules or particles. This effect of solvent suppression is exploited in the characterization of cross-link density in polybutadiene latex samples (see Fig. 38**d**). The signal decay for weak cross-link density is slow compared to that for large cross-link density. In summary, Figure 38 demonstrates that the NMR-MOUSE is a suitable device for determination of relative cross-link density in a number of different soft materials.

The possibility to excite and detect proton NMR double-quantum coherences in inhomogeneous static and radio-frequency magnetic fields was also investigated (194,195). For this purpose, specialized pulse sequences which partially refocus the strongly inhomogeneous evolution of the spin system and generate double-quantum buildup and decay curves were implemented on the NMR-MOUSE. It was shown that DQ decay curves have a better signal-to-noise ratio in the initial time regime compared to DQ buildup curves. The double-quantum buildup and decay curves were recorded for a series of cross-linked natural rubber samples. These curves give access to quantitative values of the ratio of proton total residual dipolar couplings that are in good agreement with those measured in homogeneous fields. A linear dependence of these ratios on the sulfur-accelerator content was reported.

The self-diffusion coefficient (D) of swollen liquids in elastomers can be measured using NMR-MOUSE with a bar magnet (192). The method was shown to be particularly useful for measuring D of small penetrant molecules in elastomers without the need for measurements of the transverse relaxation rates. The self-diffusion coefficient of toluene in a series of cross-linked natural rubber samples was measured and correlated with the cross-link density.

The NMR-MOUSE is simple mobile NMR sensor suitable for operation in an industrial environment. Its use for quality control is demonstrated in Figure 39 by the T_2 statistics measured at both sides of a conveyor belt with steel cords (193). The magnetic field $\boldsymbol{B}_0$ distortions from the steel cords were minimized by suitable orientation of the NMR-MOUSE with respect to the direction of the cords.

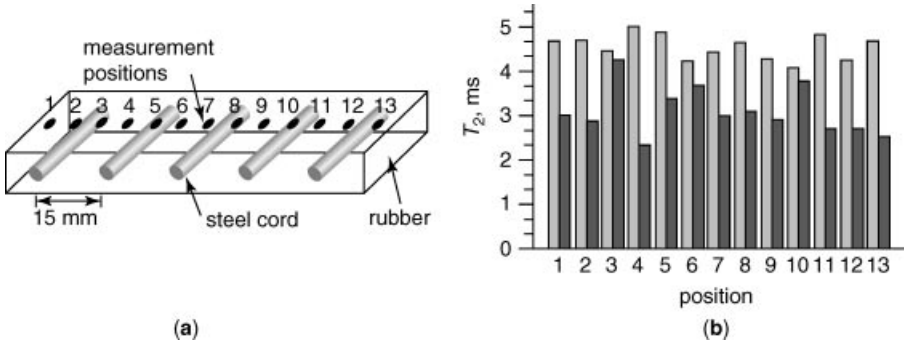

Fig. 39. Quality control of a conveyor-belt section with steel cords. (**a**) Position of measurement points. (**b**) T_2 values for upper and lower sides determined with the CPMG pulse sequence (▒) upper side and (■) lower side. Reproduced from Ref. 193, with permission from Rapra Technology.

The upper side of the belt exhibits a higher average T_2 value than the lower side, which indicates lower cross-link density. In addition to that the variance of the measured values is larger for the lower side indicating a better quality material on the upper side.

Images can be obtained with the NMR-MOUSE by measuring voxels individually by lateral displacement of the device or a change of excitation frequency to shift the sensitive volume in depth (193). On the other hand, also pulsed magnetic field gradients can be employed for phase encoding of the space information. Frequency encoding is hampered by the nonlinear magnetic field profile together with the inaccessibility of the FID.

In direction parallel to the magnetic gap, the magnetic field gradient is weakest, and a sensitive volume of a centimeter and more in width can be excited by a short rf pulse. Solenoidal gradient coils can readily be incorporated into the gap and pulsed to produce antiparallel magnetic fields (196,197). Then a gradient field is established along the gap and spatial resolution can be introduced into the measurement by phase-encoding techniques similar to single-point imaging. The effects of the background field inhomogeneity $B_z - B_0$ and of chemical shift on the magnetization phase are balanced in the peak of the Hahn echo and the only phase evolution from the pulsed field gradient remains. By applying gradient pulses with different amplitudes, $\boldsymbol{k}$ space can be scanned in the direction along the gap, so that the Fourier transformation of the acquired signal produces a one-dimensional image (196). This measurement protocol has been applied in a study of a rubber sheet with parallel textile fibers. The fibers do not contribute to the detected signal, so that their positions can be located by the dips in the 1D profile.

Clearly, the basic imaging scheme can be extended to include relaxation-time contrast for discrimination of variations in cross-link density and strain, and the 1D MRI-MOUSE (magnetic resonance imaging MOUSE) can be extended with further gradient coils to permit imaging in three dimensions. Recently, a two-dimensional imaging with a single-sided NMR probe was reported (197). Numerous applications of the MRI-MOUSE can be envisioned in soft-matter analysis, in

particular in those areas, where imaging with conventional equipment has proven to be successful and where smaller, less expensive, and mobile devices are in need.

BIBLIOGRAPHY

"Nuclear Magnetic Resonance" in *EPST* 1st ed., Vol. 9, pp. 356–396, by F. A. Bovey, Bell Telephone Laboratories; in *EPSE* 2nd ed., Vol. 104, pp. 254–327, by F. A. Bovey and L. W. Jelinski, AT&T Bell Laboratories.

1. R. R. Ernst, G. Bodenhausen, and A. Wokaun, *Principles of Nuclear Magnetic Resonance in One and Two Dimensions*, Clarendon Press, Oxford, 1987.
2. K. Schmidt-Rohr and H. W. Spiess, *Multidimensional Solid State NMR and Polymers*, Academic Press, New York, 1994.
3. V. J. McBrierty and K. J. Parker, *Nuclear Magnetic Resonance in Solid Polymers*, Cambridge University Press, Cambridge, 1993.
4. M. Mehring, *Principles of High Resolution NMR Spectroscopy in Solids*, 2nd ed., Springer, Berlin, 1983.
5. R. Kimmich, *NMR: Tomography, Diffusiometry, Relaxometry*, Springer, Berlin, 1997.
6. F. A. Bovey and P. A. Mireau, *NMR of Polymers*, Academic Press, San Diego, 1996.
7. F. Horii, in I. Ando and T. Asakura, eds., *Solid State NMR in Polymers*, Elsevier, Amsterdam, 1998.
8. H. W. Beckham and H. W. Spiess, *NMR Basic Princ. Prog.* **32**, 163 (1994).
9. H. W. Spiess, *Annu. Rep. NMR Spectrosc.* **34**, 1 (1997).
10. P. A. Mirau, S. A. Heffner, G. Koegler, and F. Bovey, *Polym. Int.* **26**, 29 (1991).
11. B. F. Chmelka, K. Schmidt-Rohr, and H. W. Spiess, in R. Tycko, ed., *Nuclear Magnetic Resonance Probes of Molecular Dynamics*, Kluwer Academic Publishes, the Netherlands, 1994, p. 113.
12. J.-P. Cohen Addad, *Prog. NMR Spectros.* **25**, 1 (1994).
13. V. D. Fedotov and H. Schneider, Structure and dynamics of bulk polymers by NMR method, *NMR, Basic Principles and Progress* Vol. 21, Springer, Berlin, 1989.
14. F. A. Bovey, *High Resolution NMR of Macromolecules*, Academic Press, New York, 1972.
15. J. N. S. Evans, *Biomolecular NMR Spectroscopy*, Oxford University Press, New York, 1995.
16. D. E. Demco, S. Hafner, and H. W. Spiess, Multidimensional NMR techniques for characterization of viscoelastic materials, in V. M. Litvinov and P. P. De, eds., *Handbook of Spectroscopy of Rubbery Materials*, Rapra Technology Ltd., Shawbury, 2002.
17. P. Mansfield and P. G. Morris, NMR imaging in biomedicine, *Advanced Magnetic Resonance*, Suppl. 2, Academic Press, New York, 1982.
18. P. T. Callaghan, *Principles of Nuclear Magnetic Resonance Microscopy*, Clarendon Press, Oxford, 1991.
19. B. Blümich, *NMR Imaging of Materials*, Clarendon Press, Oxford, 2000.
20. E. M. Haacke, R. W. Brown, M. R. Thompson, and R. Venkatesan, *Magnetic Resonance Imaging, Physical Principles and Sequence Design*, Wiley-Liss, New York, 1999.
21. M. T. Vlaardingerbroek and J. A. den Boer, *Magnetic Resonance Imaging*, 2nd ed., Springer, Berlin, 1999.
22. B. Blümich and D. E. Demco, NMR Imaging of Elastomers, in V. M. Litvinov, and P. P. De, eds., *Handbook of Spectroscopy of Rubbery Materials*, Rapra Technology Ltd., Shawbury, 2002.

23. J.-J. Delpuech, ed., *Dynamics of Solutions and Fluid Mixtures by NMR*, John Wiley & Sons, Ltd., Chichester, 1995.
24. R. Tycko, ed., *Nuclear Magnetic Resonance of Molecular Dynamics*, Kluwer Academic Publishers, Dordrecht, 1994.
25. D. Canet, *Nuclear Magnetic Resonance. Concepts and Methods*, John Wiley & Sons, Ltd., Chichester, 1996.
26. M. Munowitz and A. Pines, *Adv. Chem. Phys.* **66**, 1 (1987).
27. M. H. Levitt, *Spin Dynamics*, John Wiley & Sons, Ltd., Chichester, 2001, and references therein.
28. I. Schnell and H. W. Spiess, *J. Magn. Reson. Adv. Magn. Reson.* **151**, 153 (2001).
29. S. B. Brown and H. W. Spiess, *Chem. Rev.* **101**, 4125 (2001).
30. E. Hahn, *Phys. Rev.* **80**, 580 (1950).
31. J. G. Powles and P. Mansfield, *Phys. Lett.* **2**, 58 (1962).
32. H. Schneider and H. Schmiedel, *Phys. Lett.* **30A**, 298 (1969).
33. W.-K. Rhim, A. Pines, and J. S. Waugh, *Phys. Rev. B* **3**, 684 (1971).
34. D. E. Demco, *Phys. Lett.* **45A**, 113 (1973).
35. J. Jeener, Ampere International Summer School, Basko Polje, Yugoslavia, 1971
36. R. R. Ernst, *Chemia* **29**, 179 (1975).
37. L. Müller, A. Kumar, and R. R. Ernst, *J. Chem. Phys.* **63**, 5490 (1975).
38. W. P. Aue, E. Bertholdi, and R. R. Ernst, *J. Chem. Phys.* **64**, 2229 (1976).
39. S. R. Hartmann and E. L. Hahn, *Phys. Rev.* **128**, 2042 (1962).
40. A. Pines, M. G. Gibby, and J. S. Waugh, *J. Chem. Phys.* **59**, 569 (1973).
41. M. Munowitz and A. Pines, *Adv. Chem. Phys.* **66**, 1 (1987).
42. R. Freeman, *Spin Choreography. Basic Steps in High Resolution NMR*, Spektrum, Oxford, 1997, and references therein.
43. E. R. Andrew, A. Bradbury, and R. G. Eades, *Nature* **182**, 1659 (1958).
44. I. J. Lowe, *Phys. Rev. Lett.* **2**, 285 (1959).
45. J. S. Waugh, L. M. Huber, and U. Haeberlen, *Phys. Rev. Lett.* **20**, 180 (1968).
46. P. Mansfield, M. J. Orchard, D. C. Stalker, and K. H. B. Richards, *Phys. Rev. B* **7**, 90 (1973).
47. P. Mansfield and P. G. Morris, NMR imaging in biomedicine, *Advanced Magnetic Resonance*, Suppl. 2, Academic Press, New York, 1982.
48. A. K. Whittaker, *Annu. Rep. NMR Spectrosc* **34**, 106 (1997).
49. A. Schmidt, W. S. Veeman, V. M. Litvinov, and W. Gabrielse, *Macromolecules* **31**, 1652 (1998).
50. B. Deloche and P. Sotta, in V. M. Litvinov and P. P. De, eds., *Handbook of Spectroscopy of Rubbery Materials*, Rapra Technology Ltd., Shawbury, 2002.
51. P. G. Klein and M. E. Ries, *Prog. NMR Spectrosc.* **42**, 31 (2003).
52. P. T. Callaghan and E. T. Samulski, *Macromolecules* **30**, 113 (1997).
53. R. Ball, P. T. Callaghan, and E. T. Samulski, *J. Chem. Phys.* **106**, 7352 (1997).
54. B. Deloch, A. Dubault, and D. Durand, *J. Polym. Sci., Part B: Polym. Phys.* **30**, 1419 (1992).
55. V. M. Litvinov and H. W. Spiess, *Makromol. Chem.* **193**, 1181 (1992).
56. P. Sotta and B. Deloch, *J. Chem. Phys.* **100**, 4591 (1994).
57. P. Sotta, *Macromolecules* **31**, 3872 (1998).
58. M. G. Brereton and E. R. Ries, *Macromolecules* **29**, 2644 (1996).
59. M. G. Brereton, *Macromolecules* **24**, 6160 (1991).
60. M. E. Ries, M. G. Brereton, P. K. Klein, I. M. Ward, P. Ekanayake, H. Menge, and H. Schneider, *Macromolecules* **32**, 4961 (1999).
61. A. Dardin, R. R. Stadler, C. Boeffel, and H. W. Spiess, *Makromol. Chem.* **194**, 3467 (1993).

62. A. Dardin, H. W. Spiess, R. R. Stadler, and E. T. Samulski, *Polym. Gel Networks* **5**, 37 (1997).
63. J. Collignon, H. Sillescu, and H. W. Spiess, *Colloid Polym. Sci.* **259**, 220 (1981).
64. R. Fechete, D. E. Demco, and B. Blümich, *J. Chem. Phys.* **118**, 2411 (2003).
65. D. E. Demco, S. Hafner, C. Fülber, R. Graf, and H. W. Spiess, *J. Chem. Phys.* **105**, 11285 (1996).
66. C. Fülber, D. E. Demco, O. Weintraub, and B. Blümich, *Macromol. Chem. Phys.* **197**, 581 (1996).
67. P. Sotta, C. Fülber, D. E. Demco, B. Blümich, and H. W. Spiess, *Macromolecules* **29**, 6222 (1996).
68. M. Schneider, L. Gasper, D. E. Demco, and B. Blümich, *J. Chem. Phys.* **111**, 402 (1999).
69. A. Wiesmath, C. Filip, D. E. Demco, and B. Blümich, *J. Magn. Reson.* **149**, 258 (2001).
70. D. E. Demco, R. Fechete, and B. Blümich, *Chem. Phys. Lett.* **375**, 406 (2003).
71. A. Pines, W.-K. Rhim, and J. S. Waugh, *J. Magn. Reson.* **6**, 457 (1972).
72. S. Matsui, *Chem. Phys. Lett.* **179**, 187 (1991).
73. R. Graf, D. E. Demco, S. Hafner, and H. W. Spiess, *Solid State Nucl. Magn. Reson.* **12**, 139 (1998).
74. R. Graf, D. E. Demco, S. Hafner, and H. W. Spiess, *J. Chem. Phys.* **106**, 885 (1997).
75. J. Gottwald, D. E. Demco, R. Graf, and H. W. Spiess, *Chem. Phys. Lett.* **243**, 314 (1995).
76. M. Wang, M. Bertmer, D. E. Demco, B. Blümich, V. M. Litvinov, and H. Barthel, *Macromolecules* **36**, 4411 (2003).
77. V. M. Litvinov, H. Barthel, and J. Weis, *Macromolecules* **35**, 4356 (2002).
78. L. R. G. Treloar, *The Physics of Rubber Elasticity*, Clarendon Press, Oxford, 1975.
79. B. Erman and J. Mark, *Structures and Properties of Rubberlike Networks*, Oxford University Press, Oxford, 1997.
80. R. Fechete, D. E. Demco, and B. Blümich, *Macromolecules* **35**, 6083 (2003).
81. J.-P. Cohen Addad, in V. M. Litvinov and P. P. De, eds., *Handbook of Spectroscopy of Rubbery Materials*, Rapra Technology Ltd., Shawbury, 2002, p. 291.
82. J.-P. Cohen Addad, B. Phan Thanh, and H. Montes, *Macromolecules* **30**, 4374 (1997).
83. V. M. Litvinov, in V. M. Litvinov and P. P. De, eds., *Handbook of Spectroscopy of Rubbery Materials*, Rapra Technology Ltd., Shawbury, 2002, p. 353.
84. V. M. Litvinov and A. A. Dias, *Macromolecules* **34**, 4051 (2001).
85. V. M. Litvinov and P. A. M. Steeman, *Macromolecules* **32**, 8476 (1999).
86. V. M. Litvinov, *Int. Polym. Sci. Technol.* **15**, T/28 (1988).
87. M. G. Brereton, *Macromolecules* **23**, 1119 (1990).
88. M. G. Brereton, *Macromolecules* **24**, 2068 (1991).
89. J. P. Cohen-Addad and O. Girard, *Macromolecules* **25**, 593 (1992).
90. T. P. Kulagina, V. M. Litvinov, and K. T. Summanen, *J. Polym. Sci., Part B: Polym. Phys.* **31**, 241 (1993).
91. H. W. Weber and R. Kimmich, *Macromolecules* **26**, 2597 (1993).
92. R. Kimmich, M. Köpf, and P. T. Callaghan, *J. Polym. Sci., Part B: Polym. Phys.* **29**, 1025 (1991).
93. G. I. Sandakov, V. P. Tarasov, N. N. Volkova, Y. A. Ol'khov, L. P. Smirnov, L. N. Erofeev, and A. K. Khitrin, *Vysokomol. Soedin., Ser. B* **31**, 821 (1989).
94. N. N. Volkova, G. I. Sandakov, A. I. Sosikov, Y. A. Ol'khov, L. P. Smirnov, and K. T. Summanen, *Polym. Sci. U.S.S.R.* **34**, 127 (1992).
95. R. Kimmich, E. Fischer, P. Callaghan, and N. Fatkullin, *J. Magn. Reson. A* **117**, 53 (1995).
96. E. Fischer, F. Grinberg, R. Kimmich, and S. Hafner, *J. Chem. Phys.* **109**, 846 (1998).
97. F. Grinberg, M. Garbarczyk, and W. Kuhn, *J. Chem. Phys.* **111**, 11222 (1999).

98. D. E. Demco, S. Hafner, and R. Kimmich, *J. Magn. Reson.* **96**, 307 (1992).
99. A. Y. Grosberg and A. R. Khokhov, *Statistical Physics of Macromolecules*, American Institute of Physics, Woodbury, NY, 1994.
100. L. Gasper, D. E. Demco, and B. Blümich, *Solid State Nucl. Magn. Reson.* **14**, 105 (1999).
101. A. P. M. Kentgens, W. S. Veeman, and J. van Bree, *Macromolecules* **20**, 1234 (1987).
102. A. S. Kulik, D. Radloff, and H. W. Spiess, *Macromolecules* **27**, 433 (1994).
103. A. W. Overhauser, *Phys. Rev.* **92**, 411 (1953).
104. J. Denault and J. Prud'homme, *Macromolecules* **22**, 1307 (1989).
105. J. L. White and P. Mirau, *Macromolecules* **26**, 3049 (1993).
106. J. L. White, *Solid State NMR* **10**, 79 (1997).
107. P. Mirau, P. H. Tanaka, and F. Bovey, *Macromolecules* **21**, 2929 (1988).
108. S. A. Heffner and P. Mirau, *Macromolecules* **27**, 7283 (1994).
109. T. Fritzhanns, S. Hafner, D. E. Demco, H. W. Spiess, and F. H. Laukien, *J. Magn. Reson.* **134**, 355 (1998).
110. T. Fritzhanns, D. E. Demco, S. Hafner, and H. W. Spiess, *Mol. Phys.* **97**, 931 (1999).
111. E. Fischer, R. Kimmich, U. Beginn, M. Möller, and N. Fatkulin, *Phys. Rev. E* **59**, 4079 (1999).
112. G. Lipardi and A. Szabo, *J. Am. Chem. Soc.* **104**, 4546 (1982).
113. G. Lipardi and A. Szabo, *J. Am. Chem. Soc.* **104**, 4559 (1982).
114. G. Simon, K. Baumann, and W. Gronski, *Macromolecules* **25**, 3624 (1992).
115. H. Geen, J. J. Titman, J. Gottwald, and H. W. Spiess, *Chem. Phys. Lett.* **227**, 79 (1994).
116. M. Feike, D. E. Demco, R. Graf, J. Gottwald, S. Hafner, and H. W. Spiess, *J. Magn. Reson.* **122**, 241 (1996).
117. C. Filip, X. Filip, M. Bertmer, D. E. Demco, and B. Blümich, *J. Magn. Reson.* **150**, 184 (2001).
118. X. Feng, P. J. E. Verdegem, Y. K. Lee, D. Sandström, M. Edén, P. Bovee-Geurts, W. J. de Grip, J. Lugtenburg, H. J. M. de Grott, and M. H. Levitt, *J. Am. Chem. Soc.* **119**, 6853 (1997).
119. R. Graf, A. Heuer, and H. W. Spiess, *Phys. Rev. Lett.* **80**, 5738 (1998).
120. W. Sommer, J. Gottwald, D. E. Demco, and H. W. Spiess, *J. Magn. Reson. A* **112**, 131 (1995).
121. M. Hong, J. D. Gross, and R. G. Griffin, *J. Phys. Chem. B* **101**, 5869 (1997).
122. K. Saalwächter, R. Graf, D. E. Demco, and H. W. Spiess, *J. Magn. Reson.* **139**, 287 (1999).
123. V. M. Litvinov, M. Bertmer, L. Gasper, D. E. Demco, and B. Blümich, *Macromolecules* **36**, 7598 (2003).
124. W. Gabrielse, M. Suliman, and K. Dijkstra, *Macromolecules* **34**, 1685 (2001).
125. C. Malveau, P. Tekely, and D. Canet, *Solid State NMR* **7**, 271 (1997).
126. P. Tekely, D. Nicole, J. Brondeau, and J. J. Delpuech, *J. Phys. Chem.* **90**, 5608 (1986).
127. N. Zumbulyadis, *Phys. Rev. B* **33**, 6495 (1986).
128. K. Schmidt-Rohr, J. Clauss, and H. W. Spiess, *Macromolecules* **25**, 3273 (1992).
129. P. Sotta, C. Fülber, D. E. Demco, B. Blümich, and H. W. Spiess, *Macromolecules* **29**, 6222 (1996).
130. C. Fülber, D. E. Demco, O. Weintraub, and B. Blümich, *Macromol. Chem. Phys.* **197**, 581 (1996).
131. A. D. Meltzer, H. W. Spiess, C. D. Eisenbach, and H. Hayen, *Makromol. Chem. Rapid Commun.* **12**, 261 (1991).
132. J. A. Kornfield, H. W. Spiess, H. Nefzger, H. Hayen, and C. D. Eisenbach, *Macromolecules* **24**, 4787 (1991).

133. A. Dardin, C. Boeffel, H. W. Spiess, R. Stadler, and E. T. Samulski, *Acta Polym.* **46**, 291 (1995).
134. P. Blümler and B. Blümich, *Rubber Chem. Technol.* **70**, 469 (1997).
135. B. Blümich and D. E. Demco, in V. M. Litvinov and P. P. De, eds., *Spectroscopy of Rubbery Materials*, Rapra Technology Ltd., Shrewsbury, 2001.
136. D. E. Demco and B. Blümich, *Conc. Magn. Reson.* **10**, 19 (1997).
137. D. E. Demco and B. Blümich, *Conc. Magn. Reson.* **10**, 269 (1997).
138. D. G. Cory, *Annu. Rep. NMR Spectrosc.* **24**, 88 (1992).
139. P. Blümler and B. Blümich, *NMR Basic Princ. Prog.* **30**, 211 (1994).
140. J. H. Strange, *Phil. Trans. Soc. Lond. A* **333**, 427 (1990).
141. P. J. McDonald, *Prog. NMR Spectrosc.* **30**, 69 (1997).
142. B. Blümich, *Conc. Magn. Reson.* **10**, 19 (1998).
143. B. Blümich, *Conc. Magn. Reson.* **11**, 71 (1998).
144. A. Abragam, *Principles of Nuclear Magnetism*, Oxford Academic Press, London, 1961.
145. D. Raftery and B. F. Chmelka, *NMR Basis Princ. Prog.* **30**, 111 (1994).
146. D. E. Demco and B. Blümich, *Curr. Opp. Solid State Mater. Sci.* **5**, 195 (2001), and references therein.
147. C. Fülber, B. Blümich, K. Unseld, and V. Herrmann, *Kautsch. Gummi Kunstst.* **48**, 254 (1995).
148. P. Blümler and B. Blümich, *Macromolecules* **24**, 2183 (1991).
149. C. Fülber, K. Unseld, V. Herrmann, K. H. Jakob, and B. Blümich, *Colloid Polym. Sci.* **274**, 191 (1996).
150. R. L. Armstrong, A. Tzalmona, M. Menzinger, A. Cross, and C. Lemaire, in B. Blümich and W. Kuhn, eds., *Magnetic Resonance Microscopy*, VCH, Weinheim, 1992, p. 309.
151. P. Mansfield, R. Bowtell, and S. Blackband, *J. Magn. Reson.* **99**, 507 (1992).
152. M. A. Rana and J. L. Koenig, *Macromolecules* **27**, 3727 (1994).
153. G. Simon and H. Schneider, *Macromol. Chem. Macromol. Symp.* **52**, 233 (1991).
154. A. A. Parker, J. J. Marcinko, P. Rinaldi, D. P. Hendrick, and W. Ritchey, *J. Appl. Polym.* **48**, 667 (1993).
155. P. Blümler and B. Blümich, *Acta Polym.* **24**, 2183 (1991).
156. C. Schwarzbauer, J. Zange, H. Adolf, R. Deichnmann, U. Nöth, and A. Haase, *J. Magn. Reson. B* **100**, 178 (1995).
157. P. Sotta, B. Deloche, J. Herz, A. Lapp, D. Durand, and J.-C. Rabadeux, *Macromolecules* **20**, 2769 (1987).
158. M. Klinkenberg, P. Blümler, and B. Blümich, *Macromolecules* **30**, 1038 (1997).
159. M. Klinkenberg, P. Blümler, and B. Blümich, *J. Magn. Reson. A* **119**, 197 (1996).
160. M. Schneider, D. E. Demco, and B. Blümich, *Macromolecules* **34**, 4019 (2001).
161. M. Schneider, D. E. Demco, and B. Blümich, *J. Magn. Reson.* **140**, 432 (1999).
162. Y. Xia, *Conc. Magn. Reson.* **8**, 205 (1996).
163. P. Blümler and B. Blümich, *Magn. Reson. Imag.* **10**, 779 (1992).
164. B. Blümich and P. Blümler, *Makroml. Chem.* **194**, 2133 (1993).
165. L. Gasper, D. E. Demco, and B. Blümich, *Solid State Nucl. Magn. Reson.* **14**, 105 (1999).
166. F. Grindberg, M. Heidenreich, and W. Kuhn, *J. Magn. Reson.* **159**, 87 (2002).
167. S. R. Smith and J. L. Koening, *Macromolecules* **24**, 3498 (1991).
168. B. Klei and J. L. Koenig, *Acta Polym.* **48**, 199 (1997).
169. P. Palmas, R. Colsenet, L. Lemaire, and M. Sebbare, *Polymer* **44**, 4889 (2003).
170. P. Denner, B. Walker, and T. Willing, *Macromol. Symp.* **119**, 339 (1997).
171. P. Blümler, B. Blümich, and H. Dumler, *Kautsch. Gummi. Kunstst.* **45**, 699 (1992).
172. M. Knörgen, U. Heuert, H. Schneider, P. Barth, and W. Kuhn, *Polym. Bull.* **38**, 101 (1997).

173. M. Knörgen, U. Heuert, H. Menge, and H. Schneider, *Angew. Makromol. Chem.* **261/262**, 123 (1998).
174. J. A. Chudek and G. Hunter, *J. Mater. Sci. Lett.* **11**, 222 (1992).
175. M. Sardashti, B. A. Baldwin, and D. J. O'Donnell, *J. Polym. Sci., B: Polym. Phys.* **33**, 571 (1995).
176. A. Spyros, R. Kimmich, B. H. Briese, and D. Jenddrossek, *Macromolecules* **30**, 8218 (1997).
177. F. P. Miknis, A. T. Pauli, L. C. Michon, and D. A. Netzel, *Fuel* **77**, 399 (1998).
178. F. P. Miknis and L. C. Michon, *Fuel* **77**, 393 (1998).
179. P. Blümler and B. Blümich, *Acta Polym.* **44**, 125 (1993).
180. D. Hauck, P. Blümlr, and B. Blümich, *Macromol. Chem. Phys.* **198**, 2729 (1997).
181. P. Adriaensens, A. Pollaris, M. Kelchtermans, and J. Gelan, *Macromolecules* **36**, 706 (2003).
182. P. Adriaensens, A. Pollaris, D. Vanderzande, J. Gelan, J. L. White, A. J. Dias, and M. Kelchtermans, *Macromolecules* **32**, 4692 (1999).
183. P. J. Flory, *J. Chem. Phys.* **18**, 108 (1950).
184. P. Prado, L. Gasper, G. Fink, B. Blümich, V. Herrmann, K. Unseld, H-B. Fuchs, H. Möhler, and M. Rühl, *Macromol. Mater. Eng.* **274**, 13 (2000).
185. P. Prado, L. Gasper, G. Fink, and B. Blümich, *Appl. Magn. Reson.* **18**, 1 (2000).
186. P. Blümler, V. Litvinov, H. G. Dikland, and M. van Duin, *Kautsch. Gummi. Kundstst.* **51**, 865 (1998).
187. G. Eidmann, R. Salvesberg, P. Blümler, and B. Blümich, *J. Magn. Reson. A* **122**, 104 (1992).
188. F. Balibanu, K. Hailu, R. Eymael, D. E. Demco, and B. Blümich, *J. Magn. Reson.* **145**, 246 (2000).
189. G Zimmer, A. Guthausen, and B. Blümich, *Solid State Nucl. Magn. Reson.* **12**, 183 (1998).
190. A. Guthausen, G. Zimmer, P. Blümler, and B. Blümich, *J. Magn. Reson.* **130**, 1 (1998).
191. K. Hailu, R. Fechete, D. E. Demco, and B. Blümich, *Solid State Nucl. Magn. Reson.* **22**, 327 (2002).
192. M. Klein, R. Fechete, D. E. Demco, and B. Blümich, *J. Magn. Reson.* **164**, 310 (2003).
193. B. Blümich and D. E. Demco, in V. M. Litvinov and P. P. De, eds., *Spectroscopy of Rubbery Materials*, Rapra Technology Ltd., Shrewsbury, 2001.
194. A. Wiesmath, C. Filip, D. E. Demco, and B. Blümich, *J. Magn. Reson.* **149**, 258 (2001).
195. A. Wiesmath, C. Filip, D. E. Demco, and B. Blümich, *J. Magn. Reson.* **154**, 60 (2002).
196. I. P. Prado and B. Blümich, *J. Magn. Reson.* **144**, 200 (2000).
197. F. Casanova and B. Blümich, *J. Magn. Reson.* **163**, 38 (2003).

D. E. DEMCO
B. BLÜMICH
Institut für Technische Chemie und Makromolekulare Chemie,
Rheinisch-Westfälische Technische Hochschule

NUCLEIC ACIDS. See POLYNUCLEOTIDES.

NYLON. See POLYAMIDES.